



**THREE-DIMENSIONAL ANALYSIS OF A COMPOSITE REPAIR
AND THE EFFECT OF OVERPLY SHAPE VARIATION
ON STRUCTURAL EFFICIENCY**

THESIS

David A. Sutter, Captain, USAF

AFIT/GAE/ENY/07-M22

**DEPARTMENT OF THE AIR FORCE
AIR UNIVERSITY**

AIR FORCE INSTITUTE OF TECHNOLOGY

APPROVED FOR PUBLIC RELEASE; DISTRIBUTION UNLIMITED

The views expressed in this thesis are those of the author and do not reflect the official policy or position of the United States Air Force, Department of Defense, or the United States Government.

AFIT/GAE/ENY/07-M22

THREE-DIMENSIONAL ANALYSIS OF A COMPOSITE REPAIR AND THE
EFFECT OF OVERPLY SHAPE VARIATION ON STRUCTURAL EFFICIENCY

THESIS

Presented to the Faculty

Department of Aeronautics and Astronautics

Graduate School of Engineering and Management

Air Force Institute of Technology

Air University

Air Education and Training Command

In Partial Fulfillment of the Requirements for the
Degree of Master of Science in Aeronautical Engineering

David A. Sutter, BS
Captain, USAF

March 2007

APPROVED FOR PUBLIC RELEASE; DISTRIBUTION UNLIMITED.

AFIT/GAE/ENY/07-M22

THREE-DIMENSIONAL ANALYSIS OF A COMPOSITE REPAIR AND THE
EFFECT OF OVERPLY SHAPE VARIATION ON STRUCTURAL EFFICIENCY

David A. Sutter, BS
Captain, USAF

Approved:

Anthony Palazotto (Chairman)

date

Marina Ruggles-Wrenn (Member)

date

Greg Schoeppner (Member)

date

Abstract

This research characterizes, in the elastic range, a scarf joint with overply using digital image correlation photogrammetry and finite element modeling. Additionally, the effect of varying the overply's geometric profile is examined. Specimens are constructed from AS4/3501-6 prepreg with a $[0/\pm 45/90]_{2s}$ layup. A fixture is used to achieve a consistent scarfed hole in each panel. The patch and adhesive (FM 300) are co-cured to the panels using positive pressure, which minimizes repair porosity. Three variations in the overply geometry are used: circular, rooftop-end, and tooth-end.

The full strain field in each uni-axially loaded specimen is captured using digital image correlation photogrammetry (ARAMIS). These results validate an ABAQUS 3-D finite element model of a scarf patch with circular overply. Good correlation is evident in the longitudinal strain; strain sensitivity limits correlation in the transverse and shear directions.

The finite element model is used to identify peak out-of-plane stresses in the repair joint. Significant normal stresses occur at edge of the overply and at the inner scarf diameter.

Finally, the experimentally-measured strains of the 3 overply variations are examined. Variation in strain magnitude is insignificant; the strain gradient at the overply edge, however, is significantly lower on the profile with the tooth-edge.

AFIT/GAE/ENY/07-M22

To My Wife and Two Daughters

Acknowledgements

I am grateful for the guidance of my advisor, Dr. Anthony Palazotto. His solid mechanics expertise and his insight on the thesis process were invaluable. Additionally, I'd like to thank the sponsor of this research, Dr. Greg Schoeppner of AFRL/ML, for his extra effort and coordination in setting up this research project. Also, his perspective and assistance throughout the process were critical. Finally, I'd like to thank those who helped me turn the plan into reality. Ron Trejo showed me the how to build the perfect panel. Paul Childers and the folks at MLSA walked me through the repair process. I am indebted for their time spent teaching me the ropes and their significant effort to ensure the quality of my final product. Jack Coate taught me the ARAMIS system and guided me through every step of the testing process.

David A. Sutter

Table of Contents

	Page
Abstract.....	iv
Acknowledgements.....	vi
List of Figures	x
List of Tables	xiii
I. Introduction	1-1
1.1. Motivation.....	1-1
1.2. Research Focus	1-2
1.3. Background.....	1-2
1.3.1. Repair State of the Art.	1-3
1.3.2. Experimental Background.	1-6
1.3.3. Finite Element Modeling.	1-7
1.3.4. Full-Field Strain Measurement.	1-9
1.3.5. Strain Gauges.....	1-10
1.3.6. Moiré Interferometry.	1-11
1.3.7. Electronic Speckle Interferometry (ESPI).	1-13
1.3.8. Advanced 3-D Digital Image Correlation Photogrammetry.....	1-14
1.4. Thesis Overview	1-15
II. Specimen Fabrication.....	2-1
2.1. Panel Manufacture	2-1
2.1.1. Panel Layup.	2-1
2.1.2. Panel Cure.....	2-3
2.1.3. Non-Destructive Inspection	2-6
2.2. Panel Preparation for Test Fixture.....	2-7
2.2.1. Initial Sizing.....	2-7
2.2.2. Tab Manufacture and Adhesion.....	2-8
2.2.3. Finial Sizing.....	2-11
2.2.4. Tab Holes	2-12
2.3. Panel Scarfing and Repair.....	2-14
2.3.1. Panel Scarf Procedure.....	2-14
2.3.2. Patch Fabrication and Panel Repair.....	2-20
III. Experimental Technique	3-1

	Page
3.1. Digital Image Correlation Photogrammetry (ARAMIS®)	3-1
3.1.1. System Configuration.	3-1
3.1.2. Theory.	3-3
3.1.3. Strain Measurement.	3-13
3.2. Test Procedure	3-15
3.2.1. Panel Preparation.	3-15
3.2.2. Camera Setup.	3-16
3.2.3. Camera Calibration.	3-17
3.2.4. Physical Test Setup.	3-17
3.2.5. Noise Floor Measurement.	3-18
3.2.6. Testing and Data Acquisition.	3-18
3.2.7. Data Analysis.	3-19
3.3. Influence of ARAMIS System Parameters on Strain Measurement.	3-21
3.3.1. General Displacement and Strain Sensitivity.	3-21
3.3.2. Parameter Tradeoff Study.	3-22
IV. Finite Element Analysis.	4-1
4.1. Geometry and Material of the Finite Element Model.	4-1
4.1.1. Global Dimensions.	4-1
4.1.2. Material Properties.	4-3
4.2. Model Definition in ABAQUS	4-5
4.3. Boundary and Loading Conditions	4-6
4.4. Finite Element Model Definition	4-7
4.4.1. Model Meshing.	4-7
4.5. Reducing the Model Size	4-11
4.6. Model Convergence	4-13
4.6.1. Convergence Model Geometry.	4-13
4.6.2. Analytical Solution.	4-14
4.6.3. FEM Solution and Convergence Values	4-15
V. Results and Analysis	5-1
5.1. Comparison of Experimental Data to Finite Element Data	5-1
5.1.1. Top Panel Surface.	5-2
5.1.2. Bottom Panel Surface.	5-11
5.2. Finite Element Model Stress Analysis	5-18
5.2.1. Stresses Through the Repair Joint Thickness	5-19
5.2.2. In-Plane Scarf Joint Adhesive Stresses	5-26
5.3. Comparison of Overply Geometries	5-29
VI. Conclusions and Recommendations	6-1
6.1. Repair Fabrication	6-1
6.2. Experimental Validation of a Finite Element Model	6-2

	Page
6.3. Digital Image Correlation Photogrammetry for Strain Measurement	6-2
6.4. Finite Element Model	6-3
6.5. Overply Geometry Variation	6-4
6.6. Recommendations.....	6-5
Bibliography	BIB-1

List of Figures

	Page
Figure 1.1. Common Composite Repair Joints (Gunnion, 2006)	1-4
Figure 1.2. Plate Cross Section: Steps for Scarf Joint Repair: (a) damaged plate, (b) damage removed, (c) tapered edges of damage cutout, (d) tapered repair with adhesive and overply.	1-5
Figure 1.3. Moiré Pattern Produced by Two Sets of Lines with a 5° Relative Orientation (http://en.wikipedia.org/wiki/Moire)	1-12
Figure 1.4. Microscopic photograph of a diffraction grating provided by David Mollenhauer, AFRL	1-13
Figure 2.1. Composite Layup Table. Layup Lines Used to for Fiber Orientation.....	2-2
Figure 2.2. Use of Steel Rulers to Aid in Fiber Orientation.	2-3
Figure 2.3. Vacuum Bag Setup for Autoclave Cure	2-4
Figure 2.4. Panel Autoclave Cure Cycle (AS4/3501-6)	2-5
Figure 2.5. C-Scan Full Immersion Ultrasonic Inspection Equipment.....	2-6
Figure 2.6. C-Scan Setup. Transducer and Panel Submerged in Water	2-7
Figure 2.7. C-Scan of Panel #691	2-8
Figure 2.8. Attachment of Fiberglass Tabs to Panel Ends.....	2-9
Figure 2.9. Tensile Cut Machine used for Trimming Panel to Final Width	2-11
Figure 2.10. Vacuum Bag Setup for Tab Cure	2-11
Figure 2.11. Hole Spacing for Test Fixture Grips	2-12
Figure 2.12. Steel Pins Used to Prevent Shifting of the Panel During Re-Positioning	2-13
Figure 2.13. “Scarf-O-Matic” Used to Produce Scarfed Holes	2-14
Figure 2.14. Scarf-O-Matic Slider Assembly	2-16
Figure 2.15. Typical Panel Scarf	2-20
Figure 2.16. Layup Rosette with Patch Assembly	2-21
Figure 2.17. Overply Geometry, Configuration #1	2-22
Figure 2.18. Overply Geometry, Configuration #2	2-23
Figure 2.19. Autoclave for Curing Patch. (Vacuum bag assembly in foreground)	2-25
Figure 2.20. Patch Co-Cure Autoclave Cycle.....	2-25
Figure 3.1. Typical ARAMIS System (Trilion).....	3-2
Figure 3.2. Basic Photographic Components. (Luhmann, 2006).....	3-4
Figure 3.3. Image Parameters (<i>a.k.a. Image Orientation</i>)	3-6
Figure 3.4. Photogrammetry: Orthogonal Case	3-9
Figure 3.5. Sample Calibration Plate Images Taken During Camera Calibration.....	3-12
Figure 3.6. Intensity Field of Digitized Speckle Image w/ Elevate Portion Showing Pixels Used in Correlation. (PETERS et al., 1982)	3-13
Figure 3.7. Post-Test Ultrasonic Inspection (C-Scan) of Repaired Panel	3-19
Figure 3.8. Step Length Variation Effects.....	3-24
Figure 3.9. Facet Size Variation Effects.....	3-24
Figure 3.10. Strain Length Variation Effects	3-25
Figure 3.11. Un-filtered ϵ_{xx}	3-26
Figure 3.12. Variation Effects of Filter Runs and Size.....	3-27

	Page
Figure 4.1. Scarf Joint Cross Section.....	4-5
Figure 4.2. Basic Element Shapes Used	4-8
Figure 4.3. Model of Undamaged Panel: (a) ϵ_{11} ; (b) ϵ_{22}	4-12
Figure 4.4. Quarter Plate Geometry: (a) Mesh Seed $10t_l$; (b) Mesh Seed $20t_l$	4-14
Figure 5.1. FEM vs. Experimental: Z Displacement (mm)	5-3
Figure 5.2. ϵ_{xx} : Center Section View, Y=4.....	5-3
Figure 5.3. ϵ_{xx} : View A (Figure 5.2), Center Section View, XZ Plane, Y=4	5-4
Figure 5.4. ϵ_{xx} : Panel #696 Experimental	5-6
Figure 5.5. ϵ_{xx} : Finite Element Model	5-6
Figure 5.6. ϵ_{xx} : Data Plot, y=4, Experimental vs. Finite Element Model	5-7
Figure 5.7. ϵ_{yy} : Panel #696 Experimental.....	5-8
Figure 5.8. ϵ_{yy} : Finite Element Model.....	5-9
Figure 5.9. ϵ_{yy} : Data Plot, y=4, Experimental vs. Finite Element Model	5-9
Figure 5.10. ϵ_{xy} : Panel #696 Experimental.....	5-10
Figure 5.11. ϵ_{xy} : Finite Element Model.....	5-10
Figure 5.12. ϵ_{xy} : Data Plot, y=4, Experimental vs. Finite Element Model	5-11
Figure 5.13. ϵ_{xx} Close-Up: Lower Surface FEM Surface at Hole Boundary.....	5-12
Figure 5.14. ϵ_{xx} : Panel #696 Experimental	5-13
Figure 5.15. ϵ_{xx} : Finite Element.....	5-13
Figure 5.16. ϵ_{xx} : Data Plot, y=4, Experimental vs. Finite Element Model	5-14
Figure 5.17. ϵ_{yy} : Panel #696 Experimental.....	5-15
Figure 5.18. ϵ_{yy} : Finite Element	5-15
Figure 5.19. ϵ_{yy} : Data Plot, y=4, Experimental vs. Finite Element Model	5-16
Figure 5.20 ϵ_{xy} : Panel #696 Experimental.....	5-17
Figure 5.21. ϵ_{xy} : Panel #696 Experimental.....	5-17
Figure 5.22 ϵ_{xy} : Data Plot, y=4, Experimental vs. Finite Element Model	5-18
Figure 5.23. Stresses Through the Panel Thickness: Data Path Locations.....	5-19
Figure 5.24. σ_{xx} : Repair Cross-Section, y=4.....	5-19
Figure 5.25. σ_{xx} : Overply and Scarf Edge (Figure 5.24)	5-20
Figure 5.26. σ_{xx} : Scarf Tip (Figure 5.24).....	5-20
Figure 5.27 σ_{zz} : Repair Cross-Section, y=4.....	5-21
Figure 5.28 σ_{zz} : Overply and Scarf Edge (Figure 5.27).....	5-22
Figure 5.29. σ_{zz} : Scarf Tip (Figure 5.27)	5-22
Figure 5.30 σ_{xz} : Repair Cross-Section, y=4.....	5-23
Figure 5.31 σ_{xz} : Overply and Scarf Edge (Figure 5.30).....	5-24
Figure 5.32. σ_{xz} : Scarf Tip (Figure 5.30)	5-24
Figure 5.33 σ_{yz} Repair Cross-Section, y=4	5-25
Figure 5.34 σ_{yz} Overply and Scarf Edge (Figure 5.33).....	5-25
Figure 5.35. σ_{yz} Scarf Tip (Figure 5.33)	5-26
Figure 5.36. σ_{yy} : Stresses Transformed in-Plane with Scarf Edge	5-27
Figure 5.37. σ_{yy} : Line Plot, Stresses Transformed in-Plane with Scarf Edge.....	5-27
Figure 5.38. σ_{xy} : Stresses Transformed in-Plane with Scarf Edge	5-28
Figure 5.39. σ_{xy} : Line Plot, Stresses Transformed in-Plane with Scarf Edge.....	5-28
Figure 5.40. ϵ_{xx} : Rooftop (#690).....	5-30
Figure 5.41. ϵ_{xx} : Tooth (#688)	5-30

Figure 5.42. ε_{xx} : Round (#692)	5-30
Figure 5.43. ε_{xx} : Geometry Comparison (y=4)	5-31
Figure 5.44. ε_{yy} : Overply Geometry Comparison (y=4)	5-31
Figure 5.45. ε_{yy} : Round (#692)	5-32
Figure 5.46. ε_{yy} : Tiger (#688)	5-32
Figure 5.47. ε_{yy} : Rooftop (#690)	5-32

List of Tables

	Page
Table 2.1. Maximum Variation in Outside Scarf Diameter. Comparison of Smallest and Largest Dimensions (Percentage given compared to max diameter)	2-19
Table 2.2. Final Scarf Diameters: Inner and Outer	2-19
Table 3.1. ARAMIS Camera Options (GOM).....	3-2
Table 3.2. ARAMIS Displacement & Strain Sensitivity/Accuracy.....	3-22
Table 4.1. FE Model: Panel Dimensions	4-2
Table 4.2. FE Model: Patch Layer Dimensions.....	4-2
Table 4.3 FE Model: Material Properties	4-3
Table 4.4. Mesh Characteristics Using Swept, Advancing Front Meshing.....	4-10
Table 4.5. Ratio of FEM Predicted Laminate Stress to Theoretical Anisotropic Plate Prediction	4-16

THREE-DIMENSIONAL ANALYSIS OF A COMPOSITE REPAIR AND THE EFFECT OF OVERPLY SHAPE VARIATION ON STRUCTURAL EFFICIENCY

I. Introduction

1.1. Motivation

In both civilian and military application, the aircraft industry continues to push the envelope of performance and efficiency as an increasing percentage of aircraft structural components are manufactured from composite materials. These cutting-edge structures can be fabricated faster and are lighter, stronger, and in some cases, are more damage tolerant than their aluminum counterparts. But while the science of composite design and manufacturing has fully matured, the repair of these structures is still in its relative infancy. Much of the research on joining composite materials has focused on aspects related to initial design. In recent years, we have witnessed a new challenge arise: the struggle with aging aircraft issues in the aluminum structures built in past decades. A similar challenge in the maintenance of composite structures will quickly arise as the time in service of today's aircraft increases. The need, therefore, becomes more pressing to fully understand the mechanics of the repair joint and its ability to return full structural integrity to the damaged structure. With this knowledge, engineers and maintenance professionals will have the ability to design and apply the most efficient repair for a given application.

1.2. Research Focus

This study looks at a 3-D scarf joint with overply in a 16-ply quasi-isotropic carbon-epoxy panel loaded in tension. This repair is typical of repairs performed in the field, on both the commercial and military sides. The extent to which the combined scarf joint and overply (lap joint) have been researched is considerably less than that of the individual joints.

First, the joint will be experimentally characterized in the materials' elastic range through the use of an emerging full-field strain analysis technique that employs digital image correlation photogrammetry (ARAMIS[®]). Separately, the joint will be analyzed using a three-dimensional finite element model created using ABAQUS[®]. Comparison of the experimental and numerical results will provide insight into the ability of the ARAMIS results to validate a finite element model. A validated finite element model will provide insight into the joint's loading characteristics below the surface. Finally, the effect of modifying the geometric profile of the patch, or more specifically, of the patch overply, will be examined. The overarching goal of this research is to produce information that may be used to validate or improve existing composite repair techniques on similar thin-plate structure.

1.3. Background

If the goal of this study is to produce data that may be used to improve maintenance of composite structures, it is first useful to understand the current repair technology state of the art. Certainly others have examined the scarf repair previously using experimental, analytical, and numerical methods. We will look briefly at some of the work done in these areas to improve our understanding of the problem. Finally, since

full field strain measurement plays a pivotal role in the evaluation of the repair joints, a few of the most prominent methods currently in use will be examined.

1.3.1. Repair State of the Art.

Stated simply, the purpose of a repair is to restore sufficient strength to the damaged area for continued safe operation. Of interest here is structural damage that permeates through the entire thickness; i.e. zero load carrying capability in the damaged area. Since the inception of composite aircraft structure in the 1950s, several basic repair geometries have emerged as methods of repair, including the lap joint, the stepped-lap joint, and the scarf joint. These geometries are illustrated in Figure 1.1 in both single- and double-sided configurations. The procedures used to install these repairs are still predominantly manual; minimal progress has been made its automation.

The repair joint being examined in this study has characteristics of both a classical scarf joint and a single lap joint. The primary load path in the joint is through the scarf repair region. A significant level of the load, however, is transferred through the overply, which overlaps both the patch and the panel. Its behavior can be modeled as single lap joint.

The asymmetry of the single-sided repair with respect the plane of the applied load creates a bending moment in the repair. As loading increases, the joint bends until the moment created by the offset in the joint is counteracted by the moment required to bend the members in the joint (Pipes & Adkins, 1982). This bending, most pronounced under uni-axial tensile loading, is an important consideration. It induces a tensile stress, also known as peel stress, in the adhesive layer. Adhesive material, be it paste or film adhesive, is generally designed to carry shear load; it is significantly weaker under tensile loads. For example, FM-300M (0.05 psf), a film adhesive manufactured by Cytec Engineered Materials Inc. and commonly used in aircraft repair, has a tensile shear

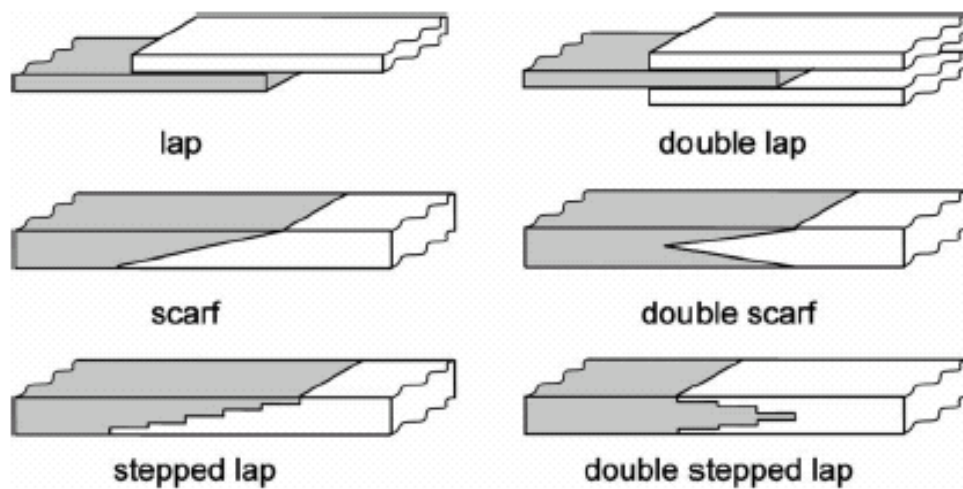


Figure 1.1. Common Composite Repair Joints (Gunnion, 2006)

strength of 4325 MPa at 24 °C; its flatwise tensile strength, however, is only 435 MPa (Cytec Engineered Materials Inc., 2005). While bending is more pronounced in the single lap joint, single scarf joints aren't immune from such bending.

The lap joint excels because of its ease of fabrication and because it avoids additional removal of structurally sound material. Various areas of the aircraft, though, are aerodynamically sensitive to changes in the outer mold line (OML). Some of the areas most sensitive include the engine nacelle; pylon; forward areas of the fuselage; and leading edges of the wing, horizontal, and vertical stabilizers. For example, the allowable mismatch on control surfaces is less than 1 mm (Mallick, 1997). Here, “mismatch” is defined as an abrupt interruption in the surface. Radar requirements of radomes or of stealth aircraft may also necessitate a similarly smooth surface. Finally, mechanical clearance may be a concern on moveable surfaces such as flaps, ailerons, etc. These aerodynamic, radar, and physical considerations significantly limit the viable repair configurations, leaving only the step-lap or the scarf joint. Both options involve removing structurally sound material from the parent structure. The stepped lap is

typically used on boron/epoxy laminates, some aramid (Kevlar) composites, and in areas where electromagnetic properties of the structure are a concern (radomes, etc.). The scarf repair, however, is three to four times faster to perform, given the same initial damage size.

The basic steps to creating a scarf joint are illustrated in Figure 1.2. After the extent of the damage is determined using non-destructive inspection (NDI) techniques,

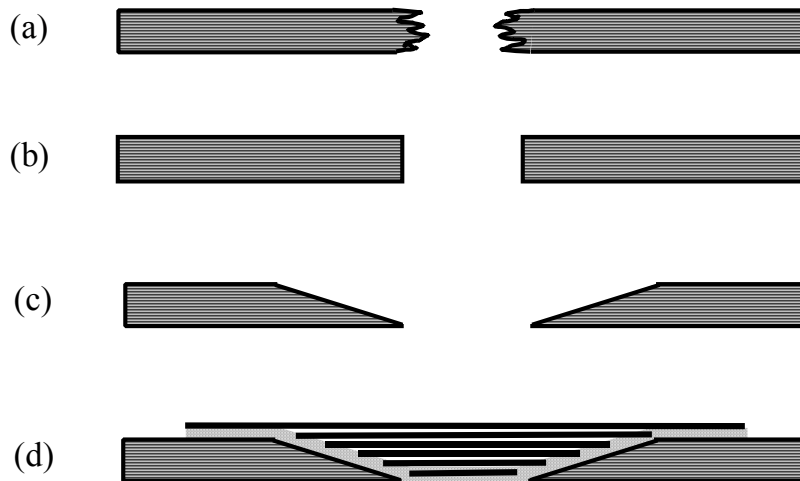


Figure 1.2. Plate Cross Section: Steps for Scarf Joint Repair: (a) damaged plate, (b) damage removed, (c) tapered edges of damage cutout, (d) tapered repair with adhesive and overply.

the damage is removed, typically using a 60-180 grit diamond router bit. Using a 90-degree router and an 80 grit abrasive disk, the hole's edges are then tapered to a shallow angle, usually less than 5° . This taper is called the scarf. The scarf is finished using 150 to 180 grit silicon carbide abrasive paper. The shallow angle increases the adhesive surface area between the patch and the parent material. Perhaps more importantly, it increases the proportion of the load transferred into the patched region as shear stress.

Next, the fiber direction and the profile of the hole for each ply layer are traced onto a stable film such as Mylar. If not previously known, fiber orientation must be determined visually using a magnifying glass. The profiles are used as the templates for cutting the individual layers for the tapered patch. Next, the patch is assembled (stacked) on a clean surface, usually a non-porous film. Lines drawn on the film are used to ensure proper orientation of the plies. Finally, the repair patch is positioned over the scarfed area in the damaged panel. As shown in Figure 1.2, if the repair is manufactured using pre-impregnated carbon-epoxy sheets (prepreg), a layer of paste or film adhesive is added to ensure adhesion of the patch to the scarf surface. After assembly, the repair is cured under vacuum pressure with heat supplied by a heat blanket and controller.

Although the method described for patch fabrication and assembly is the most common, others exist, such as an inverted scarf. This technique, commonly used by the Navy and in many marine applications, assembles the patch for a wet lay-up in reverse order. This results in the largest diameter patch going into the scarfed hole first. Its edges overlap the entire scarfed areas. Successively smaller patches are assembled on top. This technique uses the same number of repair plies as the standard method previously described. Tests by Heslehurst, Dorworth, and Hoke have indicated that while the maximum strength achieved using this method is comparable to the standard method, the standard method shows better consistency. (Heslehurst, Dorworth, & Hoke, 2000)

The repair process will be described in further detail in Chapter II during the discussion of specimen fabrication.

1.3.2. Experimental Background.

The experimental study of scarf joints in composite adherends has focused primarily on characterizing the joint in an effort to accurately predict joint failure. Most

of the studies have used approximations to model the joint, using for example machine scarfed edges on both the panel and the patch, or discrete steps similar to a step-lap joint (Ahn & Springer, 1998). An assumption is made here, in application to repair methods, that the uniform or stepped taper is an adequate approximation of the combined uniform/discrete taper actually used for repair (Mallick, 1997).

In 1998, Chalambrides et al. examined fatigue and static performance of 2° scarf joints in a quasi-isotropic panel. These results were later tied into a finite element model to help determine a method to predict static strength of the joint. During testing, they observed several failure modes, including tensile failure through the scarf joint – clearly no delamination in the overply area. The static strength of the repairs, they found, was roughly 84% of a “undamaged” specimen.

It is important to recognize the role loading direction plays in the performance of the scarf patch with a single overply. In 1995, Found and Friend looked at buckling in panels repaired using a scarf joint. They found that the scarf repair restored only 24% of the load when compared to the failure load of a “damaged” panel. The study noted that excessive buckling of the panel led to disbond of the scarf patch.

1.3.3. Finite Element Modeling.

The finite element method (FEM) has been a key method of exploring the stress and strain characteristics of the composite bonded joint. The use of such numerical methods has enabled researchers to overcome obstacles such as a non-idealized joint and non-linear adhesive behavior, which limited traditional the traditional closed form analysis approach (continuum mechanics) (Odi & Friend, 2004). Much of the early work done employed two-dimensional finite element models.

In 1978, Adkins & Pipes performed a parametric study of one-sided scarf joints loaded in tension using a linear elastic 2-D finite element model. Parameters examined in

this study included the scarf angle, the damage length, and the overlap of the doubler. The study determined that in a scarf joint with no doubler, the maximum stresses occurred at the ends of the adhesive, attributable to a shear-lag effect also observed in also seen in lap joints. For the same repair angle, however, they found that a doubler increased the stress at the bottom of the adhesive layer. This was most likely due to the added eccentricity of the doubler, they concluded. High stresses were also observed at the end of the doubler; attributed to the mismatch in stiffness between the plate and the doubler. Finally, maximum tensile stresses in the scarf joint with doubler were observed in both tapered edges of the patch and the parent material, and in the doubler immediately above the tip of the patch.

In 2004, Odi and Friend made a departure from modeling the scarf joint using effective laminate properties, as had been common to that point. Their approach, still within a 2-D plane stress framework, models each ply in the joint individually. The focus of this study was the strength prediction of composite scarf joints, using both adhesive and composite failure criteria.

Behavior of the adhesive in the joints has been a major focus of scarf joint studies. Most scarf joints are designed so as to ensure that joint failure doesn't occur in the adhesive. Odi and Friend, 2002, observed that, while modeling the adhesive using equivalent peel and shear springs may be an effective technique for joint design, it isn't practical for designing bonded repairs for composites. Later, using a 3-D finite element analysis, Gunnion and Herszberg (2006) examined how joint parameters affected adhesive normal and shear stress distribution along the bond line of the scarf joint, assuming linear adhesive behavior. 3-D elements were used to allow material orientations other than 0° and 90°. Boundary conditions on one end of the specimen were fixed in all rotation and translation directions. On the other end, only the translation in the direction of the applied load was left free. The load was applied to the joint using a

pressure load. They found that the number of peaks in peel and shear stress correspond to location of 0° plies in the laminate. Variation in the thickness of the adhesive in the bondline indicated that stresses in the bond line are very sensitive to variations in thickness. Peak stresses, both peel and shear, increase with increasing adhesive thickness. Finally, investigation of the scarf angle was revealed that the level of the peak adhesive shear decreased with scarf angle; however, the peak location as a function of the normalized bond length appears to remain constant.

Soutis and Hu point out that a 2-D analysis assumes all of the load in a panel is transferred through the repair joint (Soutis & Hu, 1998). Since the damaged panel is still able to carry some load, the strength of a repaired panel is significantly underestimated; a full 3-D analysis is required. Gunnion and Herszberg (2006) examined a 3D circular patch using the finite element method. To minimize the size of the model, $\pm 45^\circ$ plies were excluded from the lay-up, enabling modeling of the patch using a quarter-plate model with symmetry boundary conditions about the x and y axis. They found that as the angle in the patch with respect to the load increases both the peak and average adhesive peel and sheer stresses decrease. It is notable, however, their finding that the shape of the peak and peel adhesive stress distributions in the 3D model are identical to those in the 2D model. Furthermore, comparing the 2D and 3D models, it is apparent that the average stresses are reduced by 25% due to load bypass.

1.3.4. Full-Field Strain Measurement.

The three-dimensional nature of the strain field in the scarf-repaired panels necessitates an experimental method that provides full-field strain measurement with sufficient sensitivity. These methods offer several advantages over traditional measurement methods. Whereas strain gauge measurements capture strain at only a single location, full-field strain measurement techniques capture strain measurements

over the entire surface of interest; the number of strain data points collected can number in the tens of thousands or more. This comprehensive coverage enables complete characterization of regions with high strain gradients. This is especially helpful in situations where these gradients occur in unexpected regions. Strain gauges measure strain at only a single location, making this kind of characterization difficult. Finally, full-field strain measurement enables meaningful comparison of experimental and finite element results.

Three commonly used methods are moiré interferometry, electronic speckle pattern interferometry (ESPI), and advanced digital image correlation photogrammetry (ARAMIS[®], etc.). Although the scientific basis for each of these technologies is well-established, recent advances in computer processor speeds and high resolution digital imaging have taken these methods to the forefront in experimental strain measurement. However, like any experimental method, their unique strengths and weaknesses dictate their suitability for a given application.

1.3.5. Strain Gauges.

Elementary strain measurement terminology and techniques is discussed here to provide a basis upon which to evaluate the merits of these techniques. First, all of the measurement techniques mentioned capture surface strains only. They are expressed here in linear form as $e_x = \frac{\partial u}{\partial x}$, $e_y = \frac{\partial v}{\partial y}$, $e_x = \frac{1}{2} \left(\frac{\partial v}{\partial x} + \frac{\partial u}{\partial y} \right)$, where u and v represent displacement of a point on the surface. In theory, measurement and differentiation of these point displacements will yield the exact strain; however, this typically isn't feasible. Instead, an average strain is determined by measuring the post-load change in distance between two points, then dividing it by the pre-load distance between those two points, gauge length l_0 . If this value is taken to represent strain at the midpoint of the line segment, then the error between the exact strain and the measured strain is dependant upon the

gauge length and the strain gradient in that region. When the strain is assumed to be quadratic, the error between the average strain and the point strain is $\frac{k \cdot l_0^2}{12}$. For a high gradient, corresponding to a large value of k , the gauge length must be minimized to minimize the error. Gauge lengths as low as 0.2mm are commercially available today. (Dally & Riley, 1991)

Suitability criteria used for traditional strain gauge systems can be used to help evaluate the full-field techniques. Perhaps the most important criteria in evaluating suitability of a strain measurement are the gauge length, sensitivity, accuracy, and range. As discussed earlier, as the gauge length decreases, the measured strain approaches that of a point strain. This is especially important when measuring non-linear strain. The next two are often confused. Sensitivity is the smallest strain that can be accurately determined. High sensitivity, however, doesn't necessarily imply accuracy. Accuracy refers to the ability to produce and record error-free strain measurements. Finally, range is the largest strain that can be measured by the gauge. Often, a wide range is sacrificed for higher sensitivity, and vice versa. (Dally & Riley, 1991)

1.3.6. Moiré Interferometry.

Moiré interferometry is the first of the full-field strain measurement techniques to be discussed. Only the in-plane displacements are measured using this technique (a result of the optical science used). The basis of this technique is the generation and analysis of fringes in a moiré pattern. Figure 1.3 shows an example of a simple moiré pattern created by rotating a set of equally spaced lines by 5°, then superimposing these lines on the original pattern. The alternating dark and light bands are called fringes.

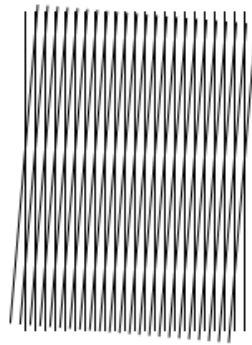


Figure 1.3. Moiré Pattern Produced by Two Sets of Lines with a 5° Relative Orientation (<http://en.wikipedia.org/wiki/Moire>)

This moiré interferometry method creates a similar moiré pattern using interference of two coherent light beams reflected off a thin diffraction grating (Figure 1.4) which has been applied to the measurement surface. Each fringe in the moiré pattern created as a result of the specimen deformation represents a finite displacement value. Post reports displacement sensitivities on the order of $0.417\text{ }\mu\text{m}$ per fringe contour are possible (Post et al, 1994). The displacement gradients in the measured direction (x or y) can be determined manually using the grating frequency and the fringe gradient. To capture strain in the orthogonal direction, a separate set of beams must be used, or the plane of the beams must be rotated. Using the two orientations, as described, displacement gradients along both axis may be determine, permitting full characterization of the strain field. (Post et al., 1994)

The moiré interferometry method excels in its high displacement sensitivity and accuracy. The use of phase shifting techniques enables automation of strain computation and increases sensitivity 10-100 times (Cloud, 1995). Several factors, however, limit the suitability of this method. First, preparation and test set-up are time intensive and best suited to a laboratory environment. The measurement surface must be perfectly flat

before application of the diffraction grating. Next, due to the requirement for a diffraction grating and a coherent light source, measurement of large areas isn't practical. Finally, displacement measurements aren't possible in the presence large vibrations, in-plane specimen rotations or rigid body displacements.

1.3.7. Electronic Speckle Interferometry (ESPI).

Electronic speckle pattern interferometry is a procedure that, like moiré interferometry, uses fringe patterns to determine displacements and strain. The method by which the moiré fringe patterns is produced, however, is entirely different. Digital superposition of a reference image (the unloaded specimen) with an image of the loaded specimen creates the fringe pattern of displacements (Cloud, 1995). Measurement sensitivity of 0.27-0.35 $\mu\text{m}/\text{fringe}$ has been reported (T. Schmidt, Tyson, & Galanulis, 2003). A strength of this method is that no manipulation of the surface is required, since it relies on the inherent texture of the measured surface. Additionally, using diverging beams, measurement of larger surfaces is possible, as compared to moiré interferometry (Vautrin, Lee, Molimard, & Surrel, 2002). The downside of this technique is that the surface must be extremely stable; approximately 1/30 second is required to capture the

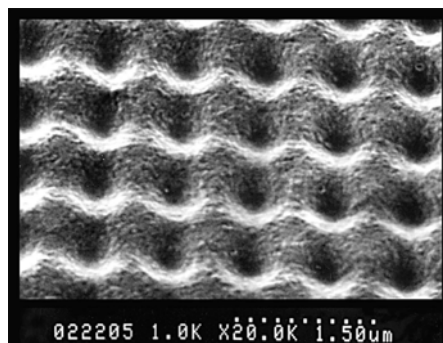


Figure 1.4. Microscopic photograph of a diffraction grating provided by David Mollenhauer, AFRL

speckle pattern. Thus, the technique in its standard form isn't suited for dynamic measurements. (Cloud, 1995). Additionally, significant noise levels in the data require substantial digital filtering. This reduces spatial resolution from one pixel to between 30 and 60 pixels. (Vautrin et al., 2002) Finally, if the speckle shifts more than its diameter, the images decorrelate, preventing further measurement. Thus, the dynamic range of the system is limited. (T. Schmidt et al., 2003)

1.3.8. Advanced 3-D Digital Image Correlation Photogrammetry.

This technique, unlike the previous two, doesn't require illumination of the surface using a coherent light source, nor does it require the use of fringe patterns to determine displacements of the surface. Instead, it uses a high-contrast, stochastic pattern of dots applied to the surface. The pattern can be easily created using a can of white and of black spray paint. Additionally, the science behind the measurements makes it ideally suited to measure out-of-plane displacements. Both before the deformation and at regular intervals during the deformation, digital photographs of the object are taken by two separate cameras. The computer then takes over and processes the images. Each image is broken up into digital subsets, called facets. A process known as image correlation identifies the individual facets in the image taken by one camera, notes its location in the image, and finds the corresponding facet in the image taken by the other camera. Using photogrammetric techniques, a three-dimensional coordinate is then assigned to each facet. Comparing the coordinates of a facet measured at different points in time, the displacement value of a facet during the deformation is determined. Finally, using this information, a displacement gradient is determined for the facet and its neighboring facets. These displacement gradients may be then used to evaluate the strain values in a given direction.

Image correlation photogrammetry, in some situations, offers unique advantages compared to the two previously discussed methods. First, the ease of surface preparation permits large or irregular surfaces to be measured. Measurement is possible of surfaces which fit into a volume up to 2m x 2m x 2m. Second, the system excels in cases where large rigid body movements are expected both in-plane and out-of-plane. As long as the object remains within the camera's field of view, measurements can be taken. Third, dynamic motion and vibration isn't a problem as long as the shutter speed of the camera is fast enough to "stop" the motion and produce a clear, un-blurred image. Shutter speeds as high as .010 micro-seconds are currently available. Finally, surface illumination, using any light source, is only required to the extent needed for a properly "exposed" digital image. Although it lacks the ultra-high measuring sensitivity of the moiré technique, the operational speed and simplicity of the system permits measurements to be easily made in a non-laboratory environment.

1.4. Thesis Overview

Chapter two discusses the manufacture of the test specimens. Using AS4/3501-6 carbon epoxy prepreg, 12 each 304.8 x 584.2 mm panels are manufactured. Each panel has sixteen plies oriented at $[0/\pm 45/90]_{2S}$ degrees with respect to the longitudinal direction. After manufacture and non-destructive inspection of each panel, the panels are prepared for testing by adding the tabs and drilling the holes for attachment to the test cell. Using these holes, the specimen is attached to a fixture to create a centered and repeatable hole with the edges scarfed at a 20:1 ratio. Finally, the patch, created using the same prepreg used to manufacture the panels, is co-cured to the panel using FM-300M (.05psf) film adhesive. A single layer, called the overply, is included in each of

the repairs. The overply overlaps both the patch and the panel. Three different overply geometries, one standard and two non-standard, are used in the repairs.

The experimental technique is the focus of chapter three. The advanced image correlation photogrammetry is discussed in greater depth, including specific characteristics of the system used (ARAMIS). Included here will be a discussion of the data extraction technique used. Then, the procedure used for physical testing of the specimens will be outlined.

Since the experimental data characterizes only the behavior at the surface of the specimens, a finite element model must be employed to gain insight into stress behavior below the surface. Chapter four discusses creation of a 3-D finite element model with a scarf-repaired hole and a single circular overply. Dimensions of the model replicate those of the test panels.

Chapter five is devoted to discussion of the experimental and of the finite element model results. First, experimental results of those panels repaired using the standard overply geometry are used to validate the finite element model. With the finite element model validated, the through-the-thickness strain behavior of the patch is explored. Finally, a comparison of the elastic behavior of the three overply configurations is examined, using experimental results.

A conclusion will be presented in chapter 6. Additionally, lessons learned and possible areas for further investigation will be discussed.

II. Specimen Fabrication

The manufacture and repair techniques of the carbon-reinforced epoxy test specimens is discussed here. This discussion will be sub-divided into three areas. First, the manufacture of the panel will be described. Next, the steps taken to prepare for the test fixture are outlined. Finally, a detailed description of the processes used to cut and repair the scarfs in the panels is provided.

2.1. Panel Manufacture

Twelve panels are constructed using AS4 carbon sheets pre-impregnated (prepreg) with 3501-6 polymer resin, manufactured by Hercules, Inc. Selection of the material is based purely on availability. This same material will later be used to fabricate the repair patches and overplies. Each panel is constructed using 16 layers of prepreg, oriented at $[0/\pm 45/90]_{2S}$ degrees. This layup gives the panel quasi-isotropic properties, and is typical of a skin panel used in aircraft construction.

2.1.1. Panel Layup.

Each of the panels was laid up manually. This prepreg comes from the factory as roll of continuous 304.8 mm material. To prevent degradation due to moisture absorption, etc. of the epoxy, the material must be sealed in an airtight plastic bag and stored in the freezer. Typically, time out of the freezer is limited before the material must be re-certified. When the prepreg is removed from the freezer, it must be allowed to warm to room temperature before removing it from the plastic bag. This prevents

moisture condensation on the prepreg, which degrades the performance of the epoxy. Every effort was made to pre-cut material sufficient for lay-up of several panels at a time, thus minimizing the time the bulk material spent outside the freezer. Three sizes were needed: 308.4 x 308.4 mm sheets for the 90° plies, 308.4 x 609.6 mm sheets for the 0° plies, and 308.4 x 584.2 mm sheets for the $\pm 45^\circ$ plies. A large industrial-style paper cutter was used to cut the material. The pre-cut material was then bagged in quantities sufficient for two panels.

The panels are laid up using the bench in Figure 2.1. Guidelines drawn on the bench aid correct fiber direction orientation. The sheets are laid out such that the factory edge of the sheet lines up with the guidelines drawn. Due to inadequacies of the cutting method, slight variations in the size of the 0° and 90° plies did exist. Although this won't be a significant problem, an effort was made to isolate any variations to the top and right edges; the bottom and left edges were kept relatively uniform. When the $\pm 45^\circ$ plies obscure the middle of some of the reference lines, steel rulers are used to provide the reference (Figure 2.2). Although not a precise process, it is estimated that this method of manual layup enables accurate material orientations to within $\pm 1^\circ$ - 2° . This is well within limits defined by standard practices.



Figure 2.1. Composite Layup Table. Layup Lines Used to for Fiber Orientation

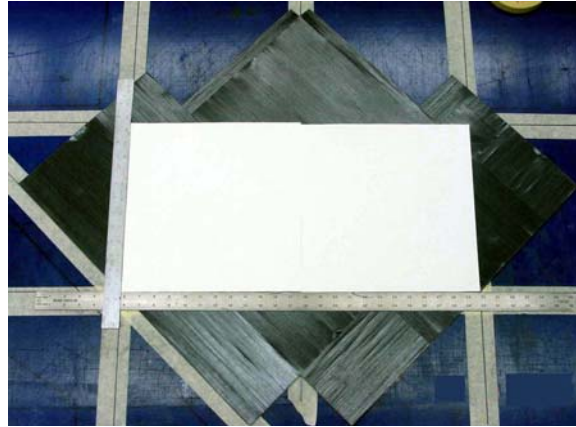


Figure 2.2. Use of Steel Rulers to Aid in Fiber Orientation.
(White surface is the prepreg backing paper)

2.1.2. Panel Cure.

Following layup, the panels are prepped for curing using the vacuum bag setup depicted in Figure 2.3. The autoclave is large enough to permit simultaneous curing of two panels. First, each uncured panel is sandwiched between two sheets of fine, Teflon coated glass sheets. These act as release plies and prevent the epoxy from adhering to anything after curing, while their porosity permits excess epoxy to flow away from the panel. Together with an aluminum caul plate, this ensemble is “gift wrapped” with a sheet of non-porous Teflon sheet. The non-porous Teflon sheet is usually a sheet of Teflon, perforated with micro-sized holes to allow gases to escape and contain the epoxy. The 3.175 mm caul plate ensures that the surfaces of the panels are smooth and flat. At the same time, air is still permitted to escape. Next, a perimeter of yellow tacky tape is placed around the two packages on the autoclave table. Tacky tape is a rubber-based adhesive taped that’s uniformly sticky. This yellow tape provides an additional barrier to contain any excess epoxy that flows out past the non-porous Teflon. At this point, two thermocouples are taped down adjacent to the panels to monitor local temperature while

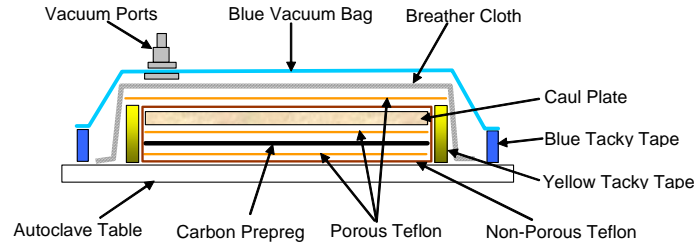


Figure 2.3. Vacuum Bag Setup for Autoclave Cure

curing. These are nothing more than two dissimilar metals that generate an electric current when heated. The current is converted to temperature by either a standalone a thermocouple monitor or by a monitor within the autoclave. Another layer of porous Teflon is placed over the perimeter established by the tacky tape, followed by a sheet of non-woven polyester breather material. The breather cloth ensures airflow when a vacuum is pulled on the bag. Finally, a perimeter of blue tacky tape is then used to attach the nylon vacuum bag over the entire ensemble. Two vacuum ports are attached to the bag at diagonally opposite corners

The cure cycle used, in accordance with manufacturer recommendations, is depicted in Figure 2.4. During the first stage of the cure, a vacuum is pulled to –30 psi. Positive pressure in the autoclave is then increased to 85 psi while the temperature is ramped up at 5° F/minute until 245° F is reached. The temperature and pressure are held at this level for 60 minutes to allow the panel layup to compact and trapped gasses to escape as the epoxy transitions to a liquid state. This process is termed “hot debulking”. At the beginning of the fourth stage, the vacuum is vented to atmospheric pressure while the positive pressure is maintained. At the same time, the temperature is again increased at the same rate until the final cure temperature of 355° F is achieved. At this point, the rate of reaction in the adhesive increases and it begins to harden. After 120 minutes, the

adhesive is fully cured and the temperature is decreased at a rate of 10° F per minute. Finally, when the temperature drops below 140° F, the pressure is turned off.

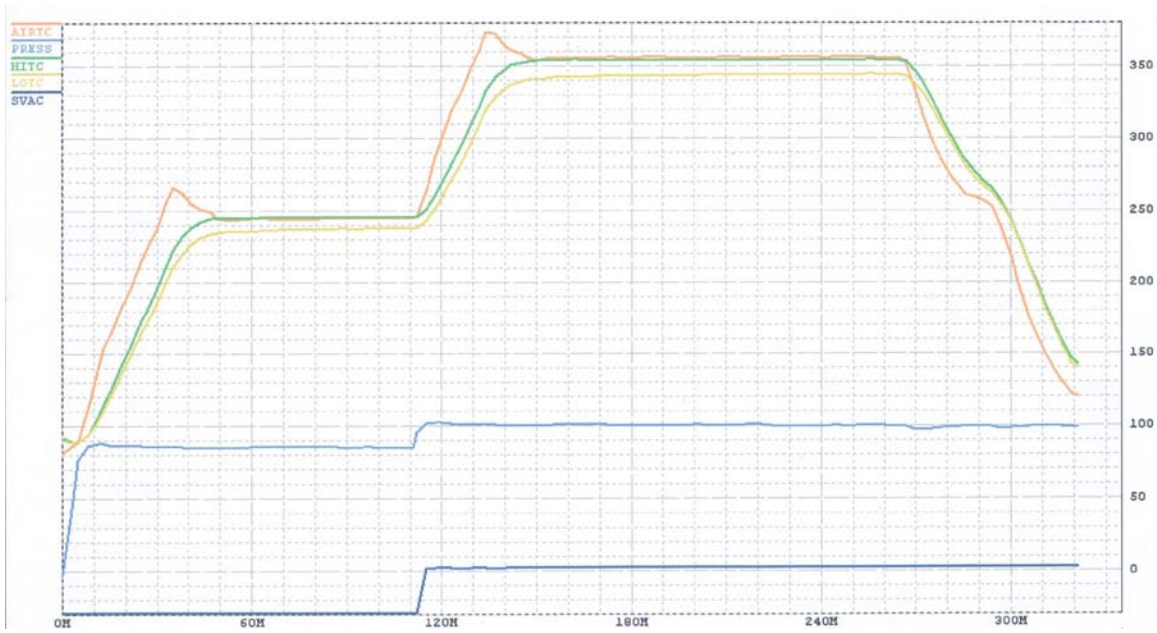


Figure 2.4. Panel Autoclave Cure Cycle (AS4/3501-6)

2.1.3. Non-Destructive Inspection

Following the autoclave cure cycle, each panel is inspected using full immersion C-scan ultrasonic inspection. The equipment is pictured in Figure 2.5. Ultra-high frequency sound waves, around 5 MHz in this application, are transmitted from the



Figure 2.5. C-Scan Full Immersion Ultrasonic Inspection Equipment

transducer to a point on the panel surface (Figure 2.6). The size of defect that can be detected is dictated by the wavelength of the signal transmitted. Typical defects detected include voids, delamination, and porosity. Both the panel and the transducer are submerged in water, which serves as a coupling medium. In air, such a frequency would be attenuated immediately after leaving the transducer. Defects in the panel are detected by measuring the level of attenuation of the signal reflected back to the transducer. In the ideal case, the sound wave travels through the panel, hits the reflective surface below the panel (an aluminum plate), and returns to the transducer without attenuation (100% reflection). When voids or defects in the panel are encountered, some or all of the signal

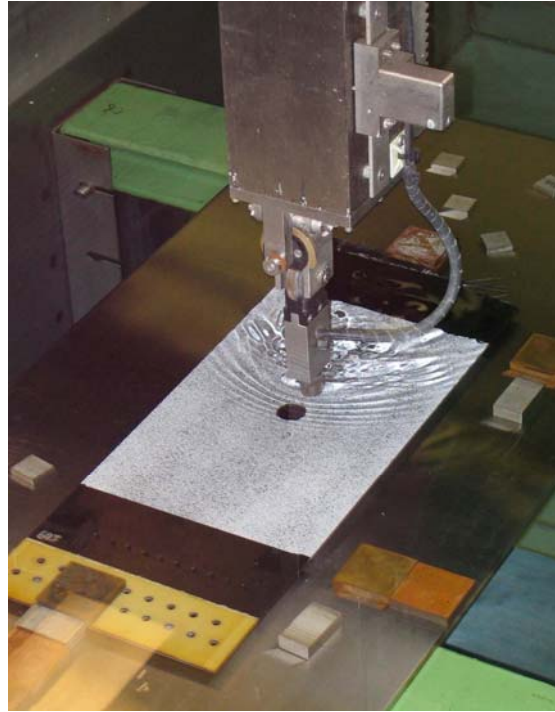


Figure 2.6. C-Scan Setup. Transducer and Panel Submerged in Water (Panel shown is a post-test specimen)

is attenuated. A C-scan of panel #691 is shown in Figure 2.7. No significant defects were identified in any of the twelve panels.

2.2. Panel Preparation for Test Fixture

The panels must be cut to final size and prepared for the testing fixture by adding tabs and drilling holes for the fixture grips.

2.2.1. Initial Sizing.

The 0° fiber direction on each panel is verified by visually identifying individual fibers on the top surface. A reference line is drawn parallel to the fiber. The first step is identifying a reference edge parallel to the fibers. Because of the special attention paid to



Figure 2.7. C-Scan of Panel #691

ensure that two edges were true during layup, each of the 12 panels had a parallel edge. The next step was to trim one of the long edges using a diamond bladed wet saw. A sliding table with guide perpendicular to the blade helps ensure square cuts are made. The panels were too long, however, to use this guide when cutting along the length of the panel. To ensure straight cuts along the length, a clamping straightedge was used. The panels were trimmed slightly wider than the finished width, to permit final trimming after the tabs are applied. Nearly equal amounts of material are cut from each side to remove any irregularities in ply overlap, etc. that may have occurred as a result of the hand-layup. With the long edges trimmed, the guide on the sliding table is reattached to square up the ends. The panels are cut to final length, 23 in.

2.2.2. Tab Manufacture and Adhesion.

Tabs are used to increase the bearing surface for the fasteners used to attach load frame grips. Additionally, it helps prevent damage to the carbon fibers as the panel is compressed between the two grip plates. Forty-eight tabs were manufactured for the

twelve panels using fiberglass-reinforced plastic (FRP). Using ASTM D 3039M as a guide, the tabs were cut to 63.5 x 203.2 mm. Using a small fixture and the tensile cut machine, a 17° bevel was ground along the length of each tab (Figure 2.8). During testing, this helps to reduce the peel stress in the adhesive used to attach the tab to the

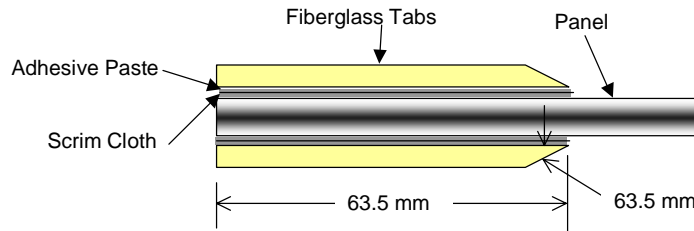


Figure 2.8. Attachment of Fiberglass Tabs to Panel Ends

panel.

The tensile cut machine is essentially a table-mounted router with a straight, small diameter diamond bit. Each pass past the bit grinds away a small amount of material. This machine is ideal for final precision trimming, as will be discussed later.

After the tabs are trimmed and beveled, the bonding surfaces of both the panels and the tabs must be prepared. Each surface is first solvent cleaned using acetone. Care is taken to wipe in only one direction, ending at an edge. This standard practice for surface preparation ensures that contaminants are wiped off the surface, as opposed to just being moved around on the surface. After wiping the entire surface once, the cloth is discarded and a new one soaked with solvent is used. The process is repeated until the cloths appear clean after wiping. This was usually achieved with three to four cloths. After the surface was solvent wiped, care was taken to avoid touching the surface and

introducing new contamination. As a precautionary measure, latex gloves were used when handling the parts.

To promote adhesion, the surface is roughened by grit blasting using 50 micron aluminum-oxide blast media. Special care must be taken to avoid removing too much material. Ideally, the surfaces should be abraded to the point that the top layer of matrix is removed without damaging the first layer of fibers. Following grit blasting, dust is removed from the surface using nitrogen compressed at 80 psi. The nitrogen is dry and non-reacting, which prevents re-contamination of the surface. The tabs must be bonded to the panels the same day the surfaces are cleaned and grit blasted. Otherwise, the surfaces must be re-energized by repeating the abrading process.

The tabs are bonded onto the panels using a high temperature paste adhesive, Hysol EA 9394. This adhesive, manufactured by Loctite Aerospace, has a maximum service temperature of 177° C, and has a high shear strength of 29 MPa at 25° C. Although the temperature during testing will be well below the maximum for this adhesive, the high service temperature ensures the adhesive properties are not degraded when panel undergoes another autoclave cycle to cure the patch. The two-part adhesive is first mixed according to manufacturer's instructions. A thin layer of adhesive is applied to both the panel and the tab. Thin, non-woven scrim cloth, used to maintain a uniform bondline thickness, is cut to the size of the tabs and laid on the tab. Additional adhesive is worked into the cloth. Finally, the tabs are placed into position at the end of each panel (Figure 2.8). To prevent shifting of the tabs during curing, the tabs are taped into place using flashbreaker tape. A vacuum bag is then built according to Figure 2.9. In this case, the larger aluminum caul plate is used as the foundation for the vacuum bag. The fiberglass spacer placed under the panel and between the tabs to prevents the panel from bowing as the vacuum is applied. Initial cure of the adhesive is achieved at room temperature for 24 hours. Full strength cure is achieved in 3-5 days at room temperature.

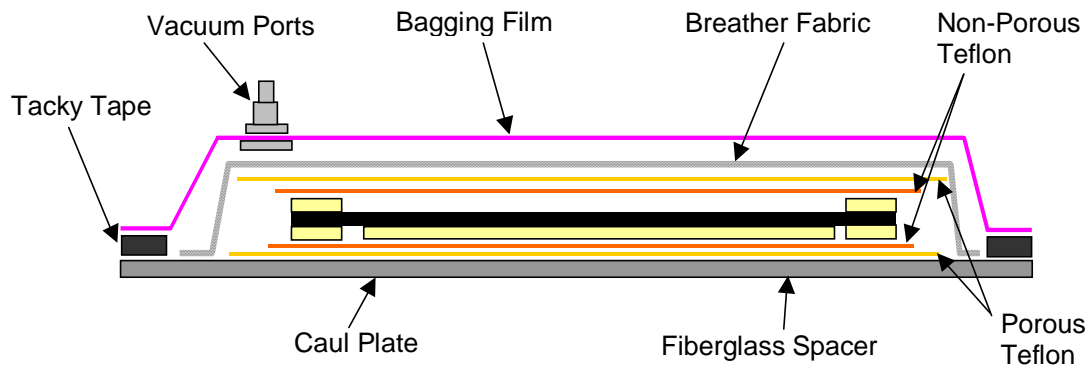


Figure 2.9. Vacuum Bag Setup for Tab Cure

2.2.3. Finial Sizing

Once all the tabs are bonded to the panels and fully cured, the panels must be cut to their final width using the tensile cut machine (Figure 2.10). The guards and the micro-adjustment fence shown are removed for adequate clearance. The clamping

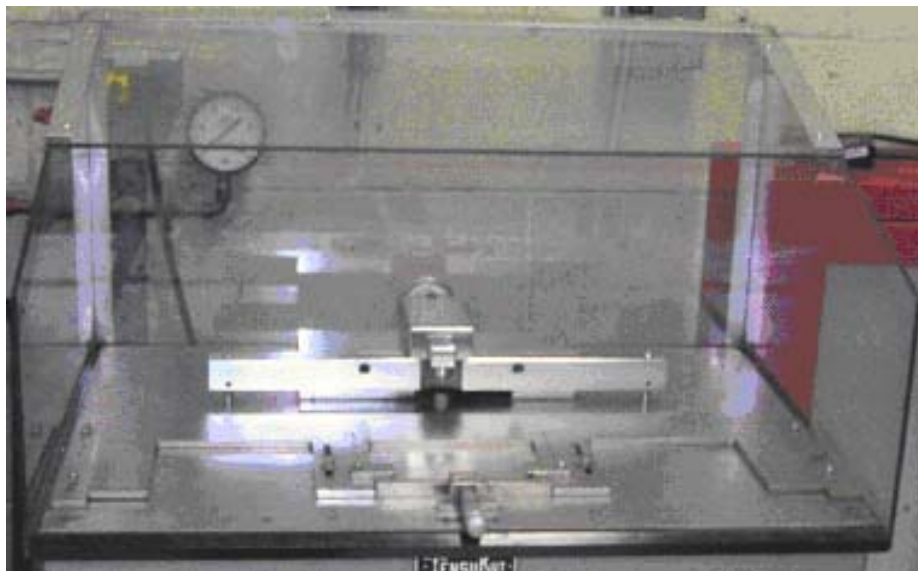


Figure 2.10. Tensile Cut Machine used for Trimming Panel to Final Width

straightedge, used with the wet saw, is again used to guide the panel as it feeds past the diamond bit. Initially, one edge on all twelve panels is fed through, ensuring a smooth, flat edge. The fence is adjusted accordingly to permit varying widths. Care is taken to minimize the amount of material removed from the first edge. Each panel is then measured to determine the minimum width. This will be the target final dimension for each panel. Using the first panel, the limit is approached incrementally, using multiple passes. Once the target dimension is reached, to within .005 in., the fence position is held constant for the remaining 11 panels. The final panel width, measured using a dial micrometer, is $8.000 \pm .005$ in., well within the tolerance recommended by ASTM D 3039M.

2.2.4. Tab Holes

With the tabs attached and the panels cut to their final widths, through holes must be drilled in the tab region to accommodate the test fixture grips. The hole pattern is depicted in Figure 2.11.

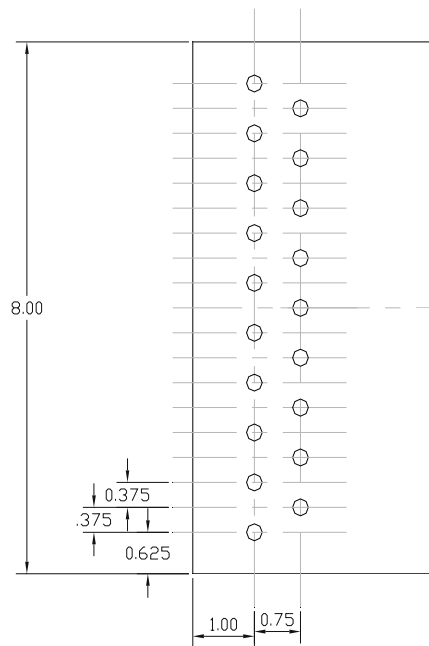


Figure 2.11. Hole Spacing for Test Fixture Grips

. The holes are cut on the drill press using a 6.35 mm straight-flute bit. The straight flutes on the bit prevent fiber tearing and delamination around the hole. To ensure proper alignment of the holes, a steel drill fixture sized to accommodate the panel is used. When one end is completed, steel pins are inserted into the holes to ensure the panel doesn't shift relative to the fixture as they are both re-positioned to drill the other side of the panel (Figure 2.12). These holes will also be used to position the panel in the fixture used to cut the scarfed holes.



Figure 2.12. Steel Pins Used to Prevent Shifting of the Panel During Re-Positioning

2.3. Panel Scarfing and Repair

2.3.1. Panel Scarf Procedure.

Once all the tab holes have been cut, the panels are ready for scarfing. The procedure used to produce the scarf is different than the procedure described in Chapter I. Since these panels are flat (or nearly so), a special grinding fixture called the Scarf-O-Matic (Figure 2.13) is used to ensure consistent, uniform taper ratios and diameters. Instead of starting with an initial “damage diameter”, the Scarf-O-Matic creates the scarf and a hole by starting at the outside diameter and working inward.

To begin the scarf, the holes previously cut in the panel are aligned with steel pins

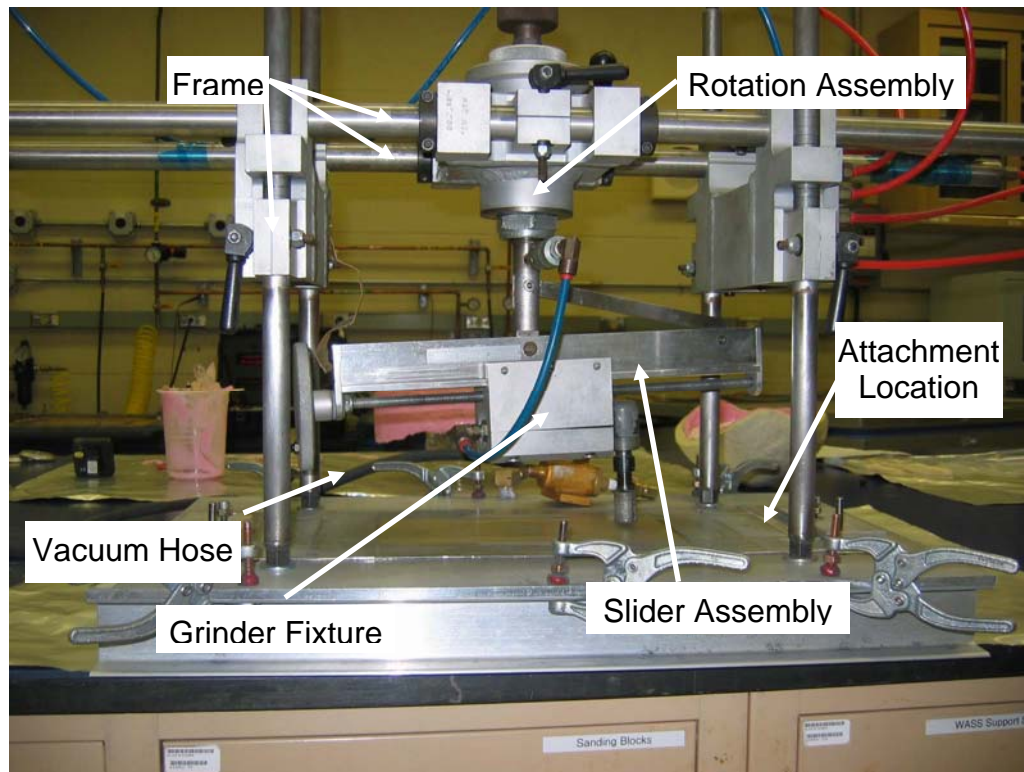


Figure 2.13. “Scarf-O-Matic” Used to Produce Scarfed Holes

in the base of the Scarf-O-Matic. A socket screw and a small aluminum plate provide clamping pressure on the ends to prevent panel movement. In the center, a thin ring of ultrasound coupling gel is applied between the panel and the fixture plate. The gel improves the vacuum pulled through a ring of small holes near the center of the fixture plate. This vacuum counteracts warping of the panel's center, caused by the material removal and resulting asymmetry conditions.

The primary components of the Scarf-O-Matic are the frame, the rotation assembly, the slider assembly, and the grinder fixture. Before any cutting is performed, the fixture must be adjusted so that the rotation axis of the cutter is coincident with the panel's center. Next, the axis must be perfectly perpendicular to the base plate. Any deviation will cause elongation in the holes. The rotation assembly controls rotation of the cutter and the vertical distance separating the panel and the slider assembly. The slider assembly is attached to the rotation shaft at two points. A pin at the bottom of the shaft connects with the center of the slider assembly. A dogleg, shown in Figure 2.14, attaches to the rotation assembly several inches up from the bottom of the rotation assembly and to the end of the slider assembly. This dogleg fixes the relative angle between the slider assembly and the panel surface, and hence the scarf ratio. Attached to the slider assembly is the grinder fixture, which holds an off-the-shelf Dotco pneumatic angle grinder equipped with a 120 grit cylindrical diamond bit. Rotation of the wheel at the end of the slider assembly drives the threaded rod, which translates the grinding fixture along the translation fixture.

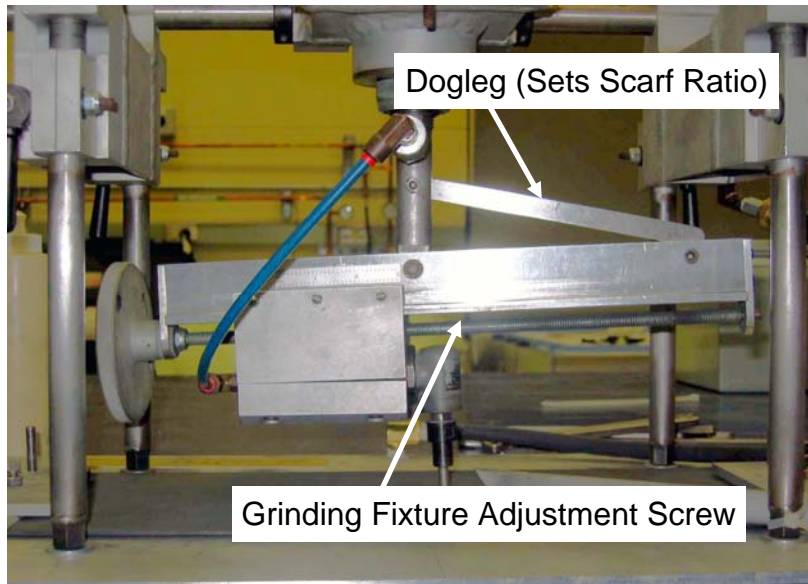


Figure 2.14. Scarf-O-Matic Slider Assembly

The inner diameter of the scarf is dictated by a combination of the outer diameter in the scarf and the thickness of the panel. Using the measured panel thickness and the target inner diameter, the outer diameter required can be calculated using simple trigonometry. The theoretical outer diameter is then set by adjusting the height of the slider assembly and the location of the grinding fixture on the slider assembly so that the diamond bit just contacts the surface of the panel. To cut the scarf, the fixture is rotated and the grinding fixture is translated along the slider beam towards the center of the hole. Typically, one or two complete rotations are required for every incremental translation of the grinding fixture. Careful attention must be paid to the sound of the angle grinder as it grinds away the composite panel. If the motor is bogged down, it means the feed rate is too high. The feed rate is dictated by a combination of the fixture rotation speed and the incremental adjustment of the grinding fixture. Consequences of a high feed rate include a rough surface and an irregular scarf angle. The rotation and translation cycle is continued until the edge of the grinder reaches the bottom surface of the panel and the

inside “plug” is liberated. At this point, nitrogen supplied to the grinder must be stopped immediately to prevent damage to the razor-thin scarf edge.

While the scarf process may seem relatively straightforward, in reality, a considerable amount of trial and error was required before relatively uniform scarfs were achieved. First, the hole diameters achieved didn’t match the diameters anticipated. Several factors contributed to this. The scarf angle is not precisely fixed with the dogleg. Even with the dogleg attached a small degree of motion possible before the threaded pins attaching the dogleg are tightened. This causes a variation in the scarf angle by as much as several degrees. Pushing up on the end of the slider assembly before tightening the pins results in a scarf which comes closest to the desired 20:1 ratio. Play in the rotation shaft also affects the scarf angle. Initially, the holes were cut with pressure applied downward at the forward edge of the slider beam. This caused a non-uniform decrease in the scarf angle. This problem was alleviated by rotating the fixture using the handle located on top of the rotation assembly.

The second significant problem encountered was elongation of the holes. If the surface of the plate is irregular, then as the grinder is rotated, the grinder will take material away from the high spots but may miss the low spots on that pass altogether. In some of the panels, the major and minor diameters of the scarf varied by nearly 6.5 mm. After making measurements using a dial indicator chucked in the angle grinder and by comparing the surface with a straight edge, it was determined that the base of the fixture wasn’t flat, but varied by as much as 0.508 mm. Several steps were taken to correct this problem. First, the sacrificial fiberglass layer that supported the panel was removed and re-attached using film instead of paste adhesive for a more uniform bond line. This didn’t solve the problem, so manual leveling of the surface was attempted using aluminum speed tape picture-framed around the perimeter of the fiberglass panel. Although this improved the situation, the variation still exceeded 0.254 mm, nearly twice

the average ply thickness. Manually straightening the 6.35 mm thick aluminum plate was attempted by clamping a pair of thick aluminum I-beams to the edges of the plate. The final solution, which reduced the surface variation to within a 0.127 mm (about one ply thickness) was achieved using a combination of the I-beams, additional tweaking of the speed tape perimeter, and minimizing use of the coupling gel to only a thin layer and only in the area immediately adjacent to the vacuum holes.

With the elongation problem fixed, there was still the question of what to do with nearly half the panels that had already been scarfed and whose holes were elongated to varying degrees. The feasibility of putting them back into the scarf fixture was doubtful. The concern was that the previously scarfed panels were no longer flat in the scarfed region; putting them back into the fixture to re-scarf the holes might only exacerbate the problem. Despite these misgivings, a trial was performed using the panel with the largest diameter variation. The slider assembly was adjusted down slightly to increase the scarf diameter slightly and ensure a fresh cut. The results were astounding. It appeared that the vacuum on the lower surface was sufficient to pull the surface flat. The panel went from having the worst variation to zero variation, measured down to the nearest .001 in. Based on these results, each panel was put back through the scarf fixture. Table 2.1 shows the variations in the outer diameter after each panel was re-scarfed. The maximum variation was acceptable at just over three percent. The final inside and outside hole diameters are given in Table 2.2. Panel to panel variation of both the inside and outside diameters is due to variation in the average panel thickness.

Table 2.1. Maximum Variation in Outside Scarf Diameter. Comparison of Smallest and Largest Dimensions (Percentage given compared to max diameter)

Panel #	Max Outer Diameter Variation	
	(mm)	
687	1.75	1.3%
688	0.56	0.4%
689	1.32	1.0%
690	0.76	0.6%
691	0.00	0.0%
692	0.94	0.7%
693	4.04	3.1%
694	0.00	0.0%
695	0.00	0.0%
696	0.00	0.0%
6101	3.73	2.8%
6102	2.59	2.0%

Table 2.2. Final Scarf Diameters: Inner and Outer

Panel #	Inner Scarf Diameter (mm)	Outer Scarf Diameter (mm)
687	24.003	129.057
688	18.644	128.549
689	21.082	131.928
690	20.447	128.600
691	18.796	132.842
692	17.501	131.115
693	18.542	129.057
694	20.218	130.073
695	17.120	128.168
696	17.424	128.575
6101	17.983	128.854
6102	18.644	129.337

2.3.2. Patch Fabrication and Panel Repair.

With each panel scarfed, the repairs can be manufactured and applied. A typical scarfed hole is shown in Figure 2.15. Each “band” represents a different ply direction.

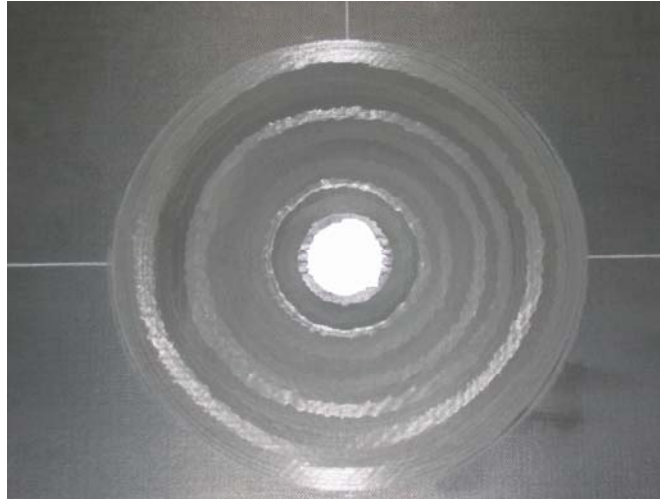


Figure 2.15. Typical Panel Scarf

Beginning with the inside hole, the largest diameter of each “band” is measured using a dial micrometer and recorded, to include the outside diameter. A total of 17 measurements are taken and recorded for each panel. These measurements will be used to size the individual layers in the repair patches. It’s clear from Figure 2.15 that there is some variation in the diameter of each ring measured. This is could be due to the difficulties previously mentioned, or more likely, just variations in the individual ply thicknesses or flatness. Sizing the patch layer to the largest diameter ensures a minimum overlap between the ply layer in the panel and the corresponding patch layer. Conventional repair wisdom says it’s better to have too much overlap (within reason) than too little, which will decrease the strength of the patch.

The same material used to construct the panels is used for the patches. Using the measurements taken, the patches are laid out on the prepreg backing using a compass. A dial micrometer is used to set the required radius on the compass. Within the outline for each of the 17 layers (including the overply), a line is drawn through the center representing the fiber direction, and the orientation of that particular patch ply is annotated (0° , 45° , etc.). Each layer is then cut out using the corner of a razor blade.

The patch is assembled starting with the first layer (inside hole diameter), like an inverted wedding cake. This first layer is essentially a plug – it will carry a negligible amount of load since it has no overlap with any panel plies. The patches are oriented using a rosette drawn on a layout surface, with a line identifying each of the orientations used in the layup (Figure 2.16). To ensure each layer is centered over the previous layer, a scribe is inserted into the small center hole already created by the compass. The tip is then lined up with the hole in the previous patch layer. With the center established, the patch is rotated until the line drawn on the backing, corresponding to the fiber orientation, is aligned with the line on the rosette corresponding to the angle required.

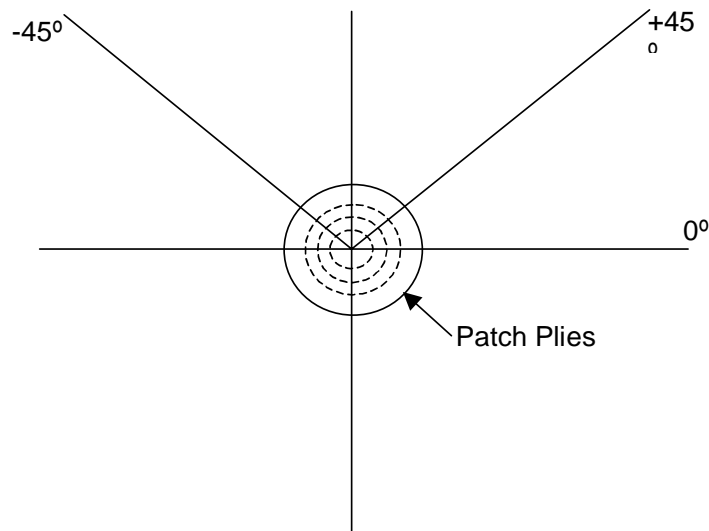


Figure 2.16. Layup Rosette with Patch Assembly

After positioning each layer, the backing paper is removed.

The last layer to go on the patch is the overply. As previously mentioned, three different geometries are used for testing. The first shape, round, is representative of the overplies dictated by most structural repair manuals. The patch is sized to the outer scarf diameter plus a half inch. The next two overply shapes are shown in Figure 2.17 and Figure 2.18. Both geometries are built by adding ends to a square which is sized so the length of the sides would equal the diameter of a standard circular overply (described previously). This ensures a minimum overlap. Next, the two geometries were sized so that their area would be constant. The height of the pyramid-shaped end of overply #2 was arbitrarily chosen. Using standard trigonometry, a short Matlab[®] program was written that varied the base angles of the small triangles, outputting the number of triangles in the pattern that would match the area and height constraints. Based on the output, the number of triangles in the first overply pattern was arbitrarily chosen to be five. The dimensions of each non-standard overply were adjusted to reflect the outer

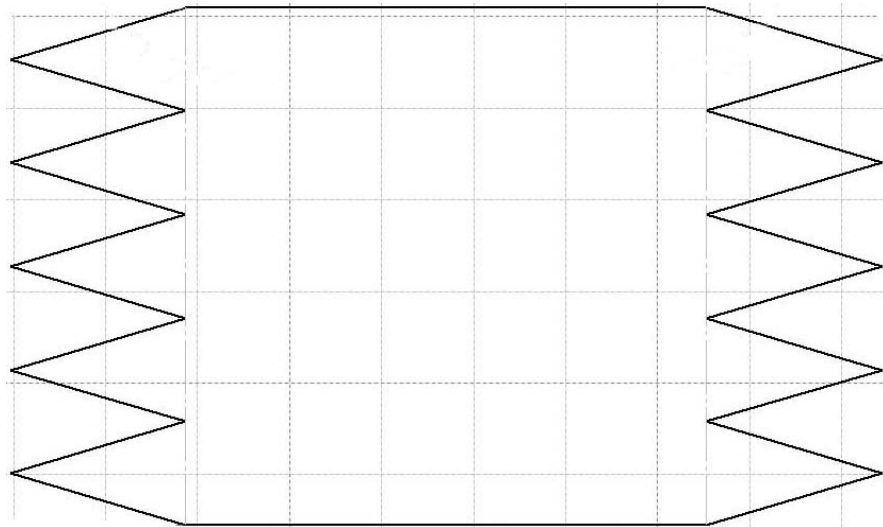


Figure 2.17. Overply Geometry, Configuration #1

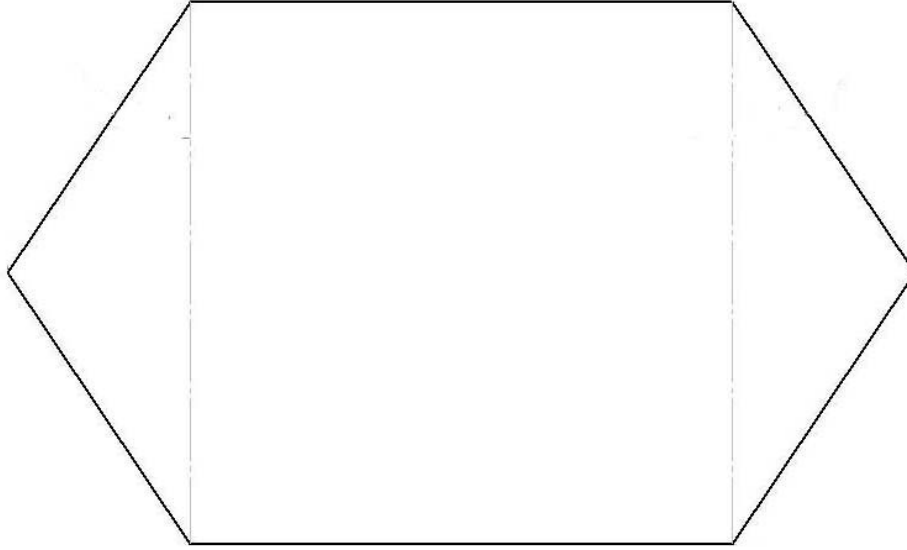


Figure 2.18. Overply Geometry, Configuration #2

scarf diameter of the panel being repaired.

After assembling the patch, a piece of film adhesive was cut out to match the overply, adding about 1.5 mm all around. A small hole, slightly smaller than the scarf inner diameter, was cut from the adhesive center to prevent excess adhesive flow during the cure cycle.

Before the patch and adhesive can be applied, the surface of the panel must be prepared. The bonding area is first solvent wiped using the same process described previously. Using a sheet of 240 grit abrasive paper, the bond area is thoroughly scuffed, following the same guidelines used for grit blasting. Only a light scuffing is required to re-energize the scarfed surface area. Nitrogen, again, is used to blow dust off the sanded surface. Then, the solvent wipe process is repeated.

The panel is now ready to be patched. The entire panel, except for the area to be bonded, was taped off using flashbreaker tape. This prevents the adhesive and epoxy that

will flow out from the patch during cure from accumulating on the panel surface. Additionally, with the two panels placed in close proximity in the vacuum bag, the tape on the edges prevents excess epoxy from gluing the two panels together. The adhesive and the patch are then positioned on the scarfed hole, ensuring proper alignment. Since the scarf is obscured by the patch and adhesive, alignment marks on the panel indicating the center of the hole are useful.

Two patched panels are cured simultaneously in the autoclave. The vacuum bag assembly shown in Figure 2.9 is used, with only two modifications. First, to absorb excess epoxy pressed out of the patch during cure, a thin sheet of nylon fabric is placed between the non-porous and porous sheets. Next, a layer of rubber, roughly 3 mm thick, is placed between the non-porous sheet and the breather cloth. This acts as a caul plate to give the patch a smooth surface.

The patch is cured in the autoclave pictured in Figure 2.19. The film adhesive used has a manufacturer-recommended cure temperature of 177° C (350° F), the same temperature used to cure the prepreg. This permits curing of the patch and the adhesive at the same time, called co-curing. A similar autoclave cycle used for panel manufacture (Figure 2.20) is used here. In this case, however, the debulking cycle is removed.

Note that used of the autoclave to cure the patch deviates from procedures typically used in maintenance, where vacuum pressure only is used when curing the patch. The positive pressure in the autoclave typically results in patch with less porosity in the epoxy matrix and in the adhesive, giving a stronger, more consistent patch. Since the goal of the experiments is to identify loading characteristics of the individual overply geometries, the autoclave cure is used to remove a possible variable in the patch performance.



Figure 2.19. Autoclave for Curing Patch. (Vacuum bag assembly in foreground)

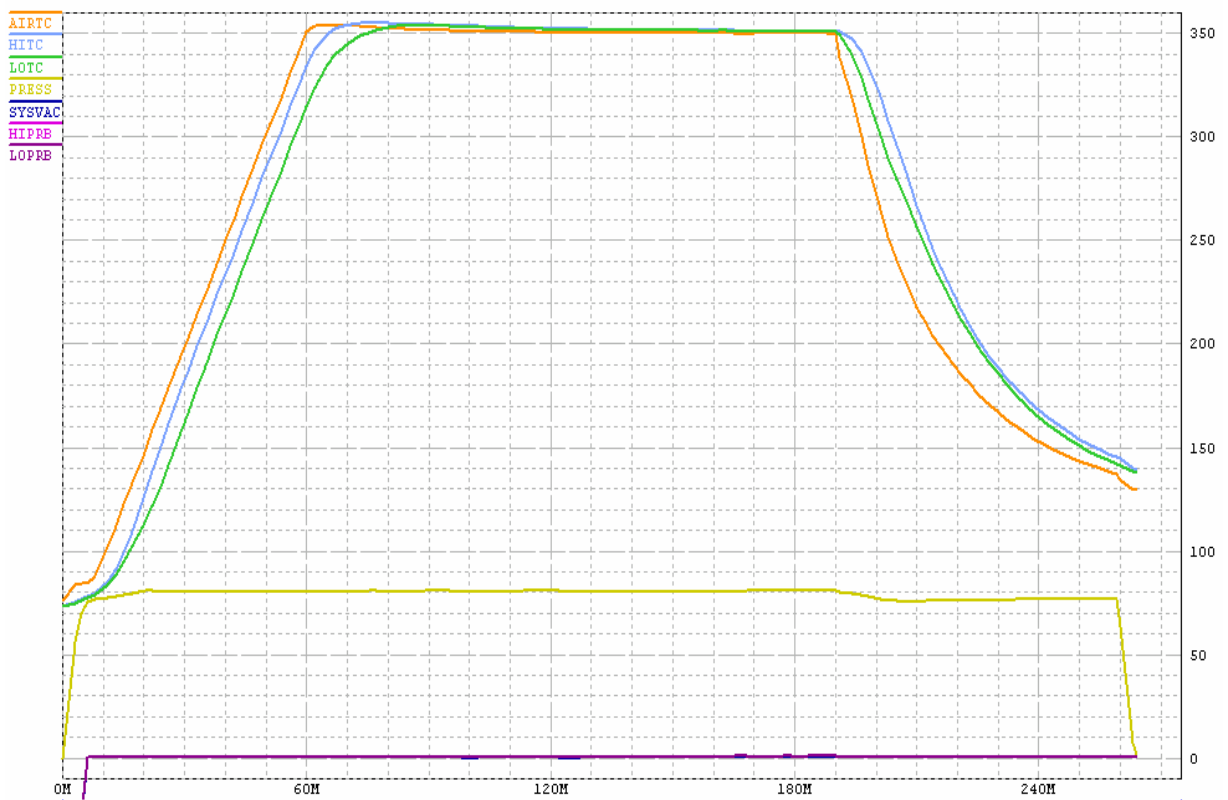


Figure 2.20. Patch Co-Cure Autoclave Cycle

III. Experimental Technique

The experimental technique used to test the physical specimens that were developed in the previous chapter is described here. An emerging full-field strain measurement technique, digital image correlation photogrammetry, described briefly in the first chapter, was selected because of its unique characteristics. Here, the technique is described in further detail, including a discussion of the underlying theory. Next, the physical test process is described. Finally, the method used to evaluate the data will be briefly discussed.

3.1. Digital Image Correlation Photogrammetry (ARAMIS[®])

3.1.1. System Configuration.

ARAMIS is the trademark name of a digital image correlation photogrammetry system manufactured by GOM mbH (Gesellschaft für Optische Messtechnik mit beschränkter Haftung - *Company for Optical Measuring Technique, LLC*). Figure 3.1 shows a typical system. Basic to any system is a computer, a trigger box, and the camera system. The computer (CPU) runs on a 64-bit LINUX operating system and is equipped with 2.4-3.8 GHz dual processors, and 2-4 GB RAM. It serves as the central data and image processing point, as well as the storage point for all images taken. Next, the triggerbox supplies power to the cameras and directs/synchronizes the camera recording. The triggerbox also serves as the input point for load, displacement data, etc. in the form of analog signals from the test machine. The third component of this system, the

cameras, serves as the primary sensing instrument. One camera is required for 2D measurements, two for 3D measurements. The ARAMIS system cameras have a resolution of either a 1.3 mega-pixels (1280 x 1024 pixels) or 4 mega-pixels (2048 x 2048) (used in this experiment). A high speed camera, capable of frame rates up to 960 Hz is also available. A summary of the features for each camera is included in Table 3.1.

Table 3.1. ARAMIS Camera Options (GOM)

System types	ARAMIS 1.3 M	ARAMIS 4 M	ARAMIS HS
Standard measuring volume in mm3	10x8x8 (with 50 mm lens + distance ring) up to 1700x1360x1360 (with 12 mm or 8 mm lens)	25x20x15 to 2000x2000x2000	25x20x15 to 1700x1360x1360
Camera resolution	1280x1024 pixels	2048x2048 pixels	1280x1024 pixels
Camera chip	2/3 inch, CCD	1 inch, CCD	1 inch, CMOS
Max. frame rate	12 Hz, optional 24 Hz	7 Hz	480 Hz at 1280x1024 pixels 960 Hz at 1280x512 pixels
Intermediate image storage	In the main memory (RAM) of the evaluating computer	In the main memory (RAM) of the evaluating computer	On the frame grabber boards of the evaluating computer
Shutter time	0.1 ms up to 2 s, computer-controlled, asynchronously triggerable	0.1 ms up to 2 s, computer-controlled, asynchronously triggerable	0.010 ms up to 1 s, computer-controlled, asynchronously triggerable
Strain measuring range	0.05 % up to >100 %	0.05 % up to >100 %	0.05 % up to >100 %
Strain accuracy	up to 0.02 %	up to 0.01 %	up to 0.02 %
Measuring results	2D or 3D displacements, strain and component contour		
For further information see http://www.gom.com			

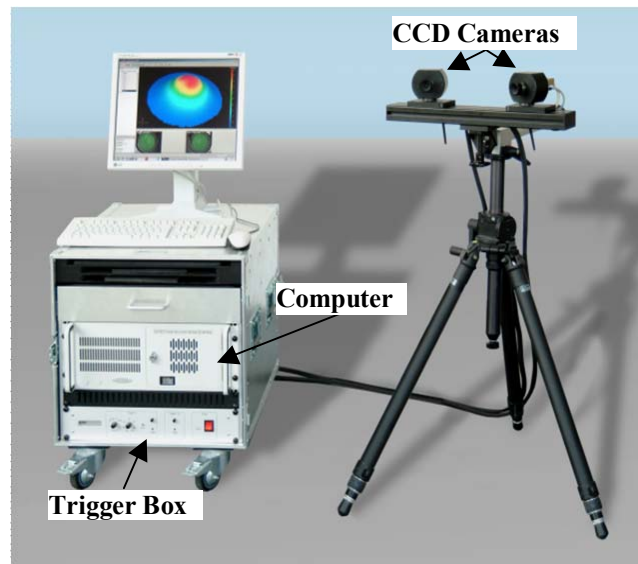


Figure 3.1. Typical ARAMIS System (Trillion)

3.1.2. Theory.

The strain measurement process can be broken down into four distinct sub-processes. First, digital photography is used to capture the basic data, the photos. The next two steps occur simultaneously. Photogrammetry is used to derive data for a three-dimensional object from two-dimensional image(s). A data processing technique known as digital image correlation, meanwhile, is to automate the processing of the digital image by identifying features on the image and, as required, to match the same feature on a different image. Finally, the data generated using photogrammetry and digital image correlation is used to calculate the surface strain. Although the specific processes employed by the ARAMIS software is proprietary information, the theory described will give the reader a relative idea of the digital image correlation photogrammetry technique.

3.1.2.1. Digital Photography.

The images taken by a digital camera are the basic data elements of this method. A basic understanding of the digital image is needed for further discussion of the strain measurement process. The heart of any digital camera is its sensor. Two sensor types, the charge-coupled device (CCD) and the complimentary metal-oxide semiconductor (CMOS), are in common use today (Mikhail, Bethel, & McGlone, 2001). Video cameras commonly use CCDs, while CMOS sensors are the basis for most digital cameras on the market. Either sensor type may be used for the digital image correlation photogrammetry process. Chu and others have demonstrated full-field strain measurement using off-the-shelf digital cameras and a laptop (T. Chu, Mahajan, & Liu, 2002). The ARAMIS system uses cameras equipped with CCD sensors, which has several advantages over CMOS. Images created by CCD sensors generally produce images with lower noise levels and their light sensitivity tends to be higher due to the architecture of the chip. (*What is the difference between CCD and CMOS image sensors in a digital camera?*, 2000) The basic light sensing element of either is a pixel. Each sensor contains

thousands of these pixels, arranged in a 2-D array. A quantity of electrons proportional to the electromagnetic energy of incident light is generated by each pixel in the array. An analog to digital device then converts the charge of each pixel's into a discrete number. For a black and white image, this value may, for instance, be represented by an 8-bit number, between 1 (black) and 255 (white).

3.1.2.2. Photogrammetry.

Photography can be defined as the projection of a three-dimensional object onto a two dimensional plane. A consequence of the projection is that information is lost about the third dimension. Photogrammetry then, is the reconstruction of that third dimension using the 2-D image(s). The basic model used in photogrammetry is shown in Figure 3.2. Point P is a point on some object. Plane **B** represents the image plane typically found in a camera, which produces a negative image. To more easily describe the geometry in the photogrammetric model, however, the equivalent positive image plane

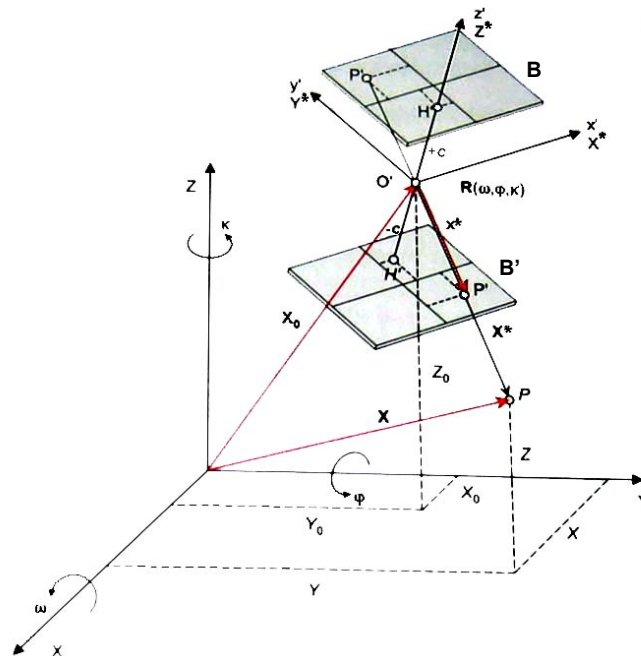


Figure 3.2. Basic Photographic Components. (Luhmann, 2006)

B' will be used in this discussion. A fundamental concept is illustrated in Figure 3.2: collinearity.

Collinearity says that a ray of light is uniquely defined by three points: the point on the ground (P), or “object”, from which the light is reflected; the perspective center it passes through (O'), and the point on the image created by the light (P'). The perspective center, in this case, is the lens of the camera. Although not truly a point, it's a reasonable approximation for the discussion here. For a ray of light reflected off the surface of a 3-D object, there is a corresponding unique point on the 2-D image. The same cannot be said, however, in the reverse direction, where there is an infinite number of points in 3-D space that could intersect the ray. (Mikhail et al., 2001)

Three right-handed Cartesian coordinate systems are commonly used in photogrammetry to define different the different frames of reference in Figure 3.2. Attached to some reference point in the 3-D space is the object space coordinate system, identified as XYZ. A similar coordinate system, $x'y'z'$, defines the image space and is named accordingly, the image space coordinate system. This coordinate system has its origin at the perspective center. A third left-handed coordinate system, $x''y''z''$, used in digital image in accordance with graphics conventions, defines the pixel and line on an image. The origin coincides with the pixel located at the first row and first column in the pixel array (Figure 3.3). The key to re-establishing the 3-D object space, is definition of the physical relationship between these 2-D and 3-D reference frames..

Within the camera are several key parameters required for object reconstruction. The 2-D coordinate frame xy is located at the geometric center of the image. Transformation from the digital coordinate system, $x'y''$, to the image geometric coordinate system xy , is given by the following coordinate transformation: (Delara, Mitishita, & Habib, 2004)

$$\begin{aligned}x &= x'' - \frac{Col+1}{2} \\ y &= \frac{Row+1}{2} - y''\end{aligned}\tag{3.1}$$

where

x'', y'' = digital system coordinates
 x, y = geometric image system coordinates
 Col = total image columns
 Row = total image rows

Point H (or H') in

is defined as the principle point. This is the point where a line orthogonal to the image plane intersects the perspective center. It's usually almost, but not exactly coincident

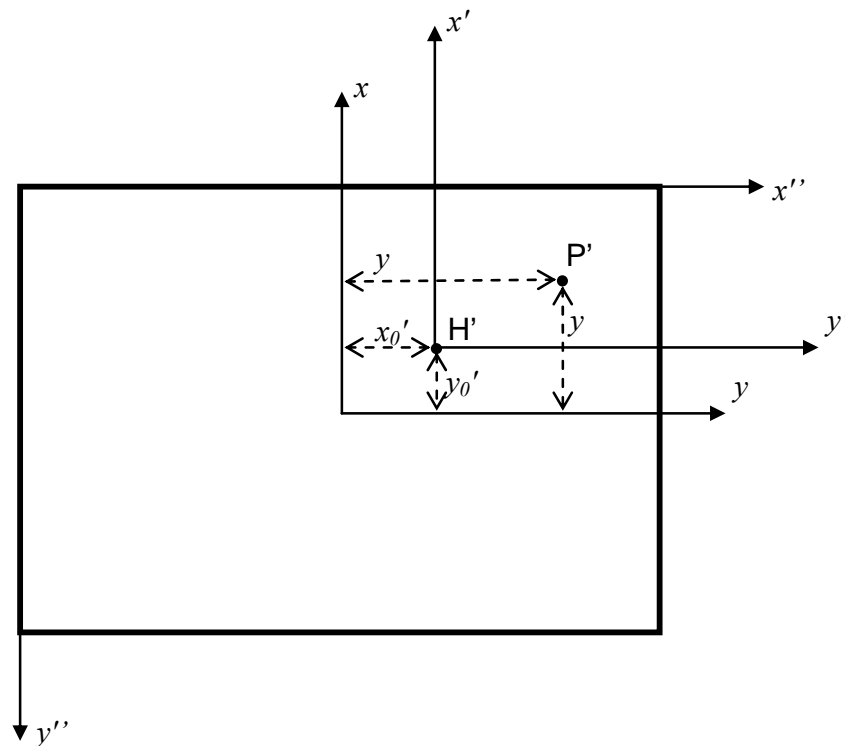


Figure 3.3. Image Parameters (a.k.a. Image Orientation)

with the image center (Figure 3.3). The distance between the principle point and the perspective center is the principle distance, c ($-c$ for the positive image). Although nearly equal to the focal distance of the camera lens, f , this distance varies as the focus ring on the lens is adjusted. For photogrammetric measurements, once the system is calibrated, adjustment of the lens focus will invalidate the calibration. For the point P' defined in the geometric image coordinate system xy , its location in the image coordinate system is then given by

$$x = \begin{bmatrix} x' \\ y' \\ z' \end{bmatrix} = \begin{bmatrix} x - x_0 \\ y - y_0 \\ -c \end{bmatrix} \quad (3.2)$$

This is the relation in its simplest form; typically correction factors to account for factors such as radial and tangential distortion are also included.

Positioning the image space coordinate system requires six parameters. The image space position in the object coordinate system is defined in Figure 3.2 by \mathbf{X}_O , where

$$\mathbf{X}_O = \begin{bmatrix} X_o \\ Y_o \\ Z_o \end{bmatrix} \quad (3.3)$$

Its orientation in space is defined by the rotation matrix

$$R = R_\omega R_\phi R_\kappa \begin{bmatrix} r_{11} & r_{12} & r_{13} \\ r_{21} & r_{22} & r_{32} \\ r_{31} & r_{32} & r_{33} \end{bmatrix} \quad (3.4)$$

where ω , ϕ , and κ represent rotations about the X, Y, and Z axis. The image space coordinates can then be transformed into object space coordinates using

$$\begin{bmatrix} x - x_0 \\ y - y_0 \\ -c \end{bmatrix} = k\mathbf{R} \begin{bmatrix} X - X_o \\ Y - Y_o \\ Z - Z_o \end{bmatrix} \quad (3.5)$$

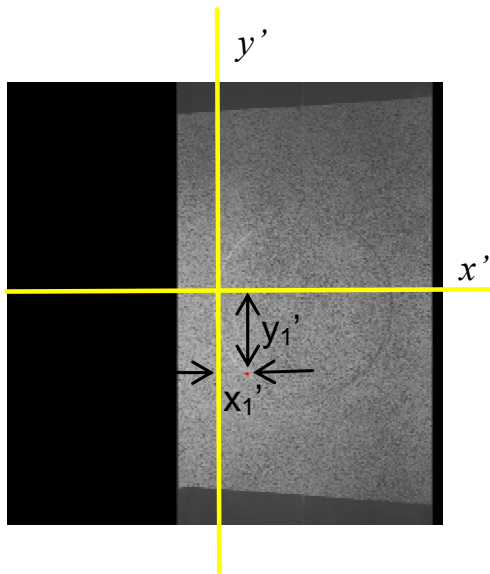
where k is a scaling constant. Expanding (3.5) and dividing the first two equations by the third yields the fundamental equations of photogrammetry, the collinearity equations:

(Mikhail et al., 2001)

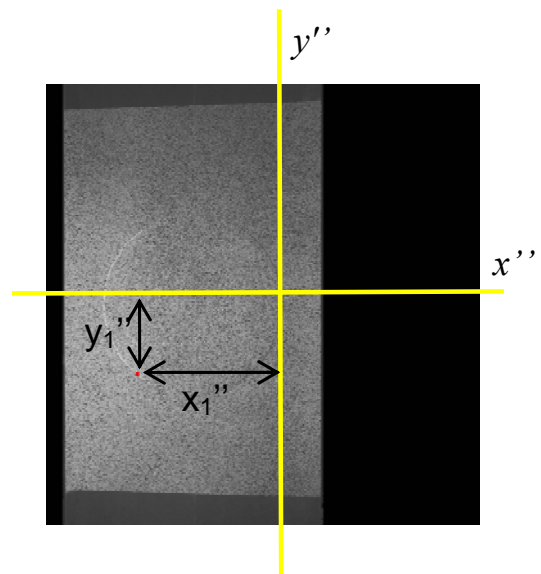
$$\begin{aligned} x - x_0 &= -c \frac{m_{11}(X - X_o) + m_{12}(Y - Y_o) + m_{13}(Z - Z_o)}{m_{31}(X - X_o) + m_{32}(Y - Y_o) + m_{33}(Z - Z_o)} \\ y - y_0 &= -c \frac{m_{21}(X - X_o) + m_{22}(Y - Y_o) + m_{23}(Z - Z_o)}{m_{31}(X - X_o) + m_{32}(Y - Y_o) + m_{33}(Z - Z_o)} \end{aligned} \quad (3.6)$$

Figure 3.4 shows a simplified case in which two cameras, having identical interior orientation and parallel optical axis which are normal to the object space coordinate system XYZ. We can apply the collinearity equations (3.6) to solve for the object space coordinates of point P. The collinearity equations are repeated for each point in each image (two sets in this case). For convenience, the object coordinate system is placed at the perspective center of the first camera (co-linear with $x'y'z$). A fixed distance along the X-axis, b , separates the two cameras. Assume, for convenience, that the interior parameter c and the base distance, b , has been previously determined. For simplicity, assume that the geometric image coordinate system xyz is coincident with the image coordinate system (*i.e.* $x'_0 = y'_0 = x''_0 = y''_0 = 0$). Also, based on the camera positions previously identified, the position and rotation of the two image coordinate systems, with respect to the object space, are as follows:

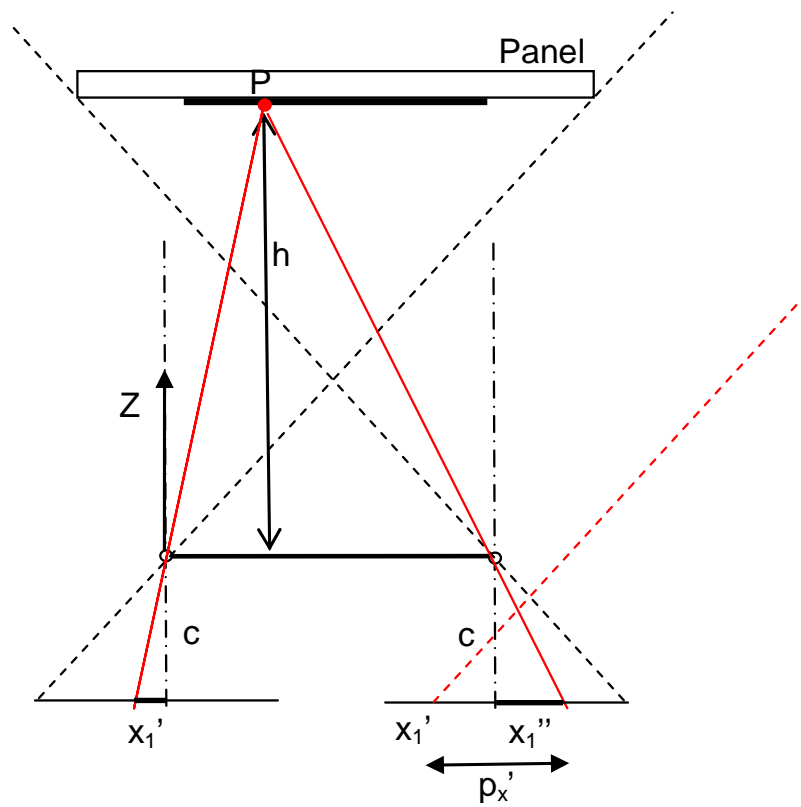
$$\begin{aligned} X_{01} &= Y_{01} = Z_{01} = Y_{02} = Z_{02} = 0 \\ X_{02} &= b \\ \omega_1 &= \varphi_1 = \kappa_1 = \omega_2 = \varphi_2 = \kappa_2 = 0 \\ \text{then } \mathbf{R}_1 &= \mathbf{R}_2 = \mathbf{I} \end{aligned}$$



(a) LH



(b) RH Image



(c) Photogrammetry: Orthogonal Case

Figure 3.4. Photogrammetry: Orthogonal Case

The collinearity equations start off as

$$\begin{aligned}
x'_1 - x_{01} &= c \frac{r_{11}(X - X_{01}) + r_{12}(Y - Y_{01}) + r_{13}(Z - Z_{01})}{r_{31}(X - X_{01}) + r_{32}(Y - Y_{01}) + r_{33}(Z - Z_{01})} \\
y'_1 - y_{01} &= c \frac{r_{21}(X - X_{01}) + r_{22}(Y - Y_{01}) + r_{23}(Z - Z_{01})}{r_{31}(X - X_{01}) + r_{32}(Y - Y_{01}) + r_{33}(Z - Z_{01})} \\
x''_1 - x_{02} &= c \frac{r_{11}(X - X_{02}) + r_{12}(Y - Y_{02}) + r_{13}(Z - Z_{02})}{r_{31}(X - X_{02}) + r_{32}(Y - Y_{02}) + r_{33}(Z - Z_{02})} \\
y''_1 - y_{02} &= c \frac{r_{21}(X - X_{02}) + r_{22}(Y - Y_{02}) + r_{23}(Z - Z_{02})}{r_{31}(X - X_{02}) + r_{32}(Y - Y_{02}) + r_{33}(Z - Z_{02})}
\end{aligned} \tag{3.7}$$

Note that in this case, since we're working with the coordinates of the negative image plane, c is defined as a positive scalar. Plugging the known values into (3.7) yields

$$\begin{aligned}
x'_1 &= c \frac{X}{Z} & x''_1 &= c \frac{X - b}{Z} \\
y'_1 &= c \frac{Y}{Z} & y''_1 &= c \frac{Y}{Z}
\end{aligned} \tag{3.8}$$

Then

$$x'_1 - x''_1 = c \left(\frac{X}{Z} - \frac{X - b}{Z} \right) = c \frac{b}{Z} = b \frac{c}{h} \tag{3.9}$$

Where p_x' is defined as the parallax. Rearranging (3.9) yields

$$Z = h = \frac{bc}{x'_1 - x''_1} \tag{3.10}$$

Using the remaining equations, we get

$$X = \frac{x'_1 h}{c} \text{ and } Y = \frac{y'_1 h}{c} = \frac{y''_1 h}{c}$$

The setup used in the above example is rarely, if ever, achievable. In most applications, a closed form solution isn't achievable. Added to the problem is the fact that the interior camera orientation parameters and the image space orientation parameters of the two cameras must also be determined. One of the most accurate

methods to achieve this is a process known as Bundle Adjustment (*a.k.a.* bundle triangulation), which yields the most accurate image and object values (Luhmann, 2006). The term “bundle” refers to the group of rays that make up an image. Using linearized versions of the collinearity equations as a mathematical basis, it solves simultaneously for position and orientation of each bundle. Included in this are the interior orientation parameters, the image space orientation parameters, and the object coordinates. Least squares adjustment assumes that the variables are stochastic in nature. The goal of least squares is to minimize these residuals. For further discussion, readers are encouraged to consult text by Mikhail (Mikhail et al., 2001) and Luhmann (Luhmann, 2006).

The ARAMIS system uses an initial calibration process to establish both the interior and exterior orientation parameters. In addition to the basic internal orientation parameters previously discussed, additional parameters account for such factors as radial, tangential, and de-centering distortion. To accomplish the calibration, a total of 13 calibration “shots” of a flat calibration panel, similar to those in Figure 3.5 are used. The calibration panel has a high contrast (white on black) array of circular dots with known position on the panel. The first five “shots”, taken by both cameras, are used to establish the basic camera geometry and the exterior orientation. An absolute coordinate system is established within the camera field of view. The next eight shots, four images per camera, further refine the distortion corrections for each camera. (Schmidt, Coe, & Tyson, 2004). The accuracy of the calibration may be affected by problems with correlation between interior and exterior parameters. Correlation between parameters exists when effects of small changes in interior parameters are indistinguishable from effects of small changes in exterior parameters. For example, when using a narrow angle lens, the image displacements created by a change in principle point location are nearly identical to displacements created by a tilt or shift in camera. This effect is combated in

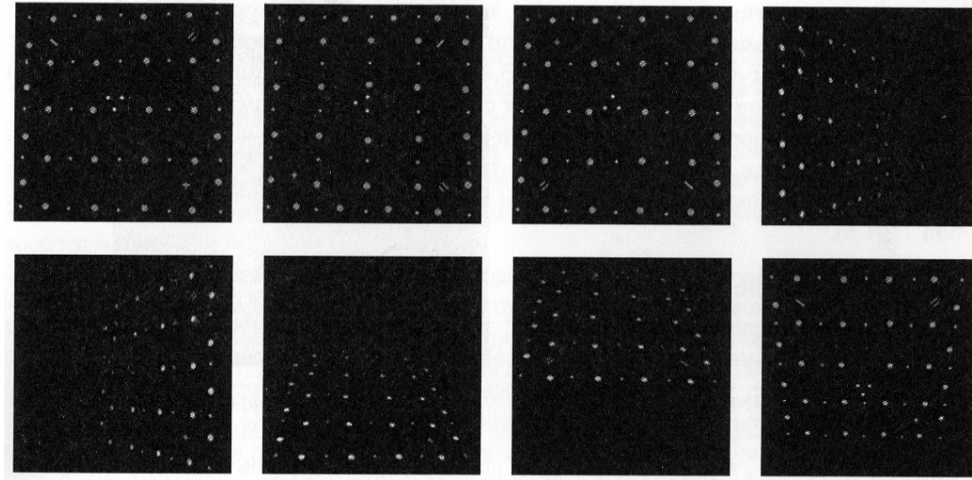


Figure 3.5. Sample Calibration Plate Images Taken During Camera Calibration

the calibration process by taking rotating the calibration panel on its axis a full 90 degrees.

3.1.2.3. Digital Image Correlation.

Digital image correlation is the process used by the software to automate the photogrammetry process for each point in the image. The ARAMIS software employs image correlation when identifying the same point in the left and right image to determine its 3-D coordinates, and when comparing the un-deformed image of a specimen to its deformed image to determining the point's relative displacement.

As previously discussed, during the analog to digital conversion, each pixel is assigned a discrete intensity value, varying in this case from 0 to 255. The ARAMIS process requires that a stochastic “speckle” pattern be applied to the surface of the test specimen. A sample image intensity resulting from a speckle pattern is shown in Figure 3.6. This figure highlights a small subset, called a facet, which is used in the image correlation process. The speckle pattern ensures that each facet is statistically unique

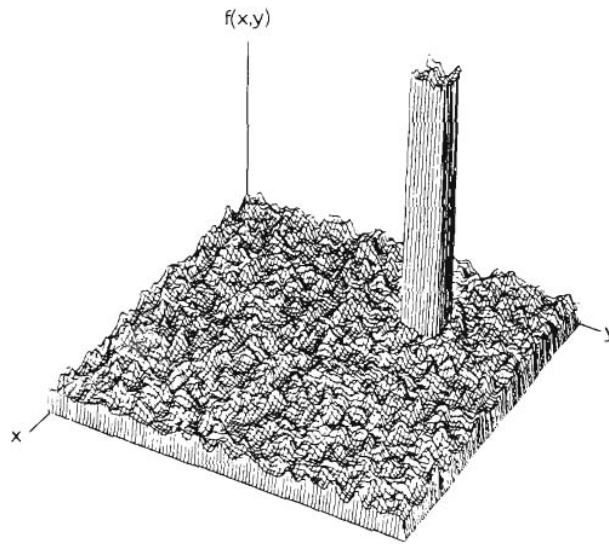


Figure 3.6. Intensity Field of Digitized Speckle Image w/ Elevate Portion Showing Pixels Used in Correlation. (Peters et al., 1982)

within the image (Chu, Ranson, Sutton, & Peters, 1985). Several approaches exist for matching the facet of an undeformed image to its deformed counterpart. In the facet matching process, the cross-correlation constant, C , is used to compare the two subsets, looking for the one which maximizes C . Interpolation, using for example, a bilinear method, allows sub-pixel accuracy in determining the center location of a deformed pixel. (T. C. Chu et al., 19850901). A number of search techniques have been identified, including an iterative approach (coarse to fine), a second-order Newton-Raphson method, and a genetic optimization algorithm (Chu et al., 2002)

3.1.3. Strain Measurement.

The deformation of a surface, or its strain, is determined by ARAMIS using a deformation gradient tensor. A deformation gradient, in its simplest illustration, describes the deformation of infinitesimal squares into infinitesimal parallelograms. The formal definition of the deformation gradient tensor is given as

$$d\bar{x} = \mathbf{F} \cdot d\bar{X} \quad (3.11)$$

Using the chain rule on (3.11) yields

$$\mathbf{F} = \frac{d\bar{x}}{d\bar{X}} \quad (3.12)$$

$$F_{ij} = \frac{\partial x_i}{\partial X_j} \text{ (cartesian coordinates)}$$

To determine the displacement gradient, suppose you have three un-deformed vectors on a surface, \bar{M}_1, \bar{M}_2 , and \bar{M}_3 . As the surface deforms, the original vectors will deform with the material into the new vectors, \bar{m}_1, \bar{m}_2 , and \bar{m}_3 . The consequence of the ARAMIS assumption of homogeneous deformation of surrounding points is that straight lines will deform to straight lines. For the 2-D case, let's assume that no deformation occurred out-of-plane, so that $\bar{M}_3 = \bar{e}_3$ and $\bar{m}_3 = \bar{e}_3$, where $\bar{e}_1, \bar{e}_2, \bar{e}_3$ are unit vectors in the coordinate directions. If we assemble the un-deformed and deformed vectors into the tensors

$$\begin{aligned} [f_0] &= [\bar{M}_1 \quad \bar{M}_2 \quad \bar{M}_3] \\ [f] &= [\bar{m}_1 \quad \bar{m}_2 \quad \bar{m}_3] \end{aligned} \quad (3.13)$$

Then the deformation gradient is given by

$$[F] = [f][f_0]^{-1} \quad (3.14)$$

Polar decomposition says that deformation gradient tensor can be separated into a rotation and stretch tensor. Two different variations are given, depending on whether the element is stretched or rotated first. (Brannon, 2003) ARAMIS uses the “stretch first” tensor, which is given by

$$\mathbf{F} = \mathbf{R} \cdot \mathbf{U} \quad (3.15)$$

where

\mathbf{R} = Rotation Tensor

\mathbf{U} = Right Stretch Tensor (Stretch First)

The values of the strain, then, can be directly determined using (*ARAMIS User Manual*, 2005)

$$\mathbf{U} = \begin{bmatrix} U_{11} & U_{12} \\ U_{21} & U_{22} \end{bmatrix} = \begin{bmatrix} 1 + \varepsilon_{xx} & \varepsilon_{xy} \\ \varepsilon_{xy} & 1 + \varepsilon_{yy} \end{bmatrix}$$

To calculate the deformation gradient from a 2-D displacement field, ARAMIS uses a neighborhood of points (facet centers). Three points will give a closed form solution for the deformation gradient tensor. For more than three points, a Gaussian least squares adjustment process is used. ARAMIS allows definition of the neighborhood of points used to determine the strain: the minimum size is 3 x 3, with additional sizes available in increments of two (5,7,9, etc.). Only the outer-most facets are actually used in the calculation. Since facet location is three-dimensional, ARAMIS uses an orthogonal projection of the points in the specified neighborhood of the point of interest onto a plane tangent to the surface at that point. For further information on use of the deformation gradient to determine strain, readers are encouraged to consult literature on continuum mechanics.

3.2. Test Procedure

The basic test procedure using the ARAMIS system includes applying the speckle pattern to the specimen, setting up the cameras, calibrating the system, a noise floor check, data acquisition (testing), and analysis post-processing.

3.2.1. Panel Preparation.

The preparation of the panel for grip attachment was described in-depth in Chapter II. Before testing, the panels also must be painted with the speckle pattern. After masking off the rest of the panel to prevent overspray, a uniform layer of flat, white spray paint is applied to the region of interest on the panel. On top of this, a uniform “splattering” of black spray paint is applied. This random pattern is best achieved by

pushing down the spray nozzle only part-ways, preventing full atomization of the paint and resulting in small “blobs” of paint on the surface. Areas of higher black paint density may create problems with correlation. The best application technique is a smooth, sweeping motion, starting and stopping the spray beyond the edges of the surface. Depending on the facet size expected, the individual dots should be small enough so that there are several dots on the perimeter of each facet. Dots that are too large will create non-unique facets, creating problems during correlation. Dots too small may lack the necessary contrast (gives uniform intensity level) for unique identification of the facets. When the software can’t correlate a facet between two images, the data for that point is discarded, resulting in a hole in the data surface. Although not done during these experiments, ensure the specimen has unique features that will permit proper alignment of the user-defined reference system during data post-processing. For specimens that lack an intrinsically definable feature within the experimental field of view, small indicators such as a dark “tick marks” or a dotted black line may be applied with a fine-tip sharpie outside the area of immediate interest (there is a risk these features may prevent image correlation, resulting in data voids at those locations).

3.2.2. Camera Setup.

The approximate distance between the cameras and the test specimen during testing should be determined so that the test specimen fills up the camera’s field of view. This gives the highest possible image resolution for the setup, which translates into better displacement sensitivity. The focus also needs to be sharp. Finally, the cameras need to be positioned so that the area of interest is captured by both cameras. The two cameras are mounted on a horizontal bar, which is mounted on a tripod (Figure 3.1). The ideal angle of intersection for the two cameras should be around 24° , although angles as high as 40° may work (T. Schmidt et al., 2004). Once the camera adjustments have been

made, the focus should be locked and the cameras tightened to the horizontal bar. Any movement of either the focus or the cameras on the bar (with respect to each other) will invalidate the calibration.

3.2.3. Camera Calibration.

Much of the calibration process has been described previously in the theory section. Several calibration plates are supplied with the system; the calibration plate with the overall size closest to the specimen size is used. For testing of the panels, a 0.3 m calibration panel is used. The calibration plate is mounted on a separate tripod. The plate is located at approximately the same distance from the cameras as will be the specimen during testing. Additionally, the plate should fill the camera's field of view. Step by step prompts by the ARAMIS software takes you through the calibration process. Note that the location of the camera tripod may be moved around after calibration, provided that the cameras don't move on that horizontal bar and that the focus or aperture isn't adjusted.

3.2.4. Physical Test Setup.

The panels are tested using a Tinius Olsen 4-post 60 kip load frame (S/N Q2220-1-4). The panels are attached to the load frame using steel grips. These grips, attached to either end of the panel, are two steel plates that sandwich the tabbed area of the panels. The holes previously drilled in the tabbed areas match the holes in the steel plates. Nineteen stainless $\frac{1}{4}$ -20 bolts and nuts attach the plates to the panel. Between both the bolt and the nut are flat washers to prevent damage to the grips. To ensure uniform clamping pressure, the bolts are torqued to 210 in lbs. in a clockwise pattern, tightening the four bolts on at the ends of the two rows, then the next four bolts in, and so on until the bolts at the center are tightened. After both sets of grip plates are attached to the panel, the panel is loaded into the load frame using approximately 3 in. diameter steel

pins. The upper head of the load frame moves while the bottom remains stationary. To absorb some of the recoil anticipated after fracture, a heavy spring and washer are placed around the shank of the bottom load frame attachment fixture. After testing, several panels, however, we found that using a single washer was insufficient. The recoil was completely compressing the heavy spring and driving it down through the washer (into the larger diameter hole below).

3.2.5. Noise Floor Measurement.

The noise floor is determined by capturing data at two stages (both with zero load conditions) and observing the strain values calculated. Ideally, there should be zero strain. However, due to analysis round-off, etc., a “noise floor” does exist. A noise floor measurement wasn’t performed before conducting these tests. According to the distributor, a typical value is 50-100 $\mu\epsilon$ for a 1280 pixel camera (Trillion Quality Systems, LLC, 2004). The noise floor for a 2048 pixel camera is expected to be slightly lower. Also, lower displacements generally have a low signal to noise ratio, resulting in noisier strain data.

3.2.6. Testing and Data Acquisition.

After installation into the test fixture, the slack is removed from the machine by moving the frame head up to the point just before additional travel would begin to pull on the panel. The load indicator on the load frame controller is zeroed at this point. The load rate during testing is controlled using a specified crosshead speed of .05 in/min (using ASTM 3039M as a guide). An analog signal sent from the load frame controller provides the camera system capturing the front of the panel with load information for each stage. The calibration constant is used in ARAMIS to translate the volts (DC) signal to a corresponding load value, accurate to within 100 lbs. An irresolvable problem with the system prevents the analog load signal from reaching the second ARAMIS system

capturing strains on the backside of the panel. When each test run is initiated, the two systems are triggered manually one after the other. This means that the loads at corresponding frame numbers should be close, but are not exactly equal.

The system capture rate for the system is set at 3 frames (stages) per minute. For the load speed used, this allows a capture rate fast enough so that the necessary specimen changes can be captured, but not so fast that available disk storage is exceeded before testing completion.

3.2.7. Data Analysis.

Each panel was taken to, or just below, its failure limit, resulting in over 100 different stages. As discussed previously, however, the focus of this study is behavior of the patched panel in the material elastic range. During testing, each panel had a loud “pop” in the range of 75-93 kN. This is assumed to correspond to failure of the 90° plies. No inspection was done at this point, however, to verify this assumption. The clearly defined vertical lines in Figure 3.7 from the post-test Ultrasonic C-scan inspection indicates that these plies had failed during the course of the test.

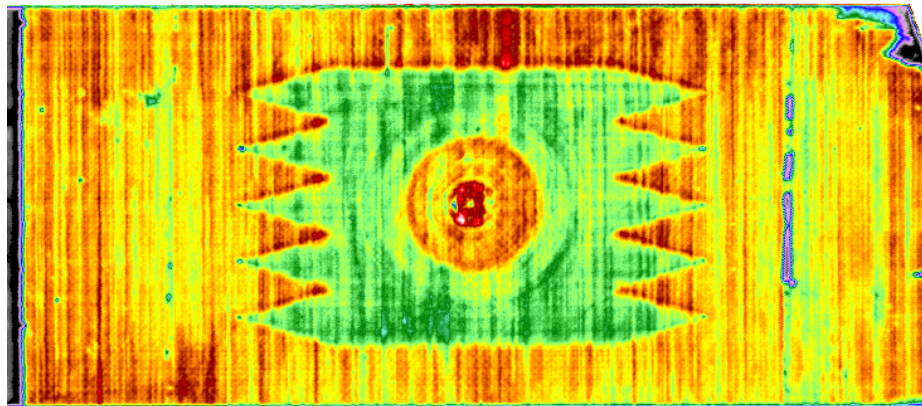


Figure 3.7. Post-Test Ultrasonic Inspection (C-Scan) of Repaired Panel

3.2.7.1. Project Mode.

After testing, the data (pictures) must be processed into desired strain values. For detailed processing steps and techniques, refer to the ARAMIS User's Manual (*ARAMIS user manual*2005). In the *Project* mode of the software, each stage of interest is selected. All the stages in the test may be selected; however, to minimize processing time, only those corresponding to loads of interest (66.72 kN in this case) and the reference stage are selected. The reference stage, used to define the total strain, is set here at the zero load stage, stage 0. All strain calculations will be conducted relative to the stage 0 position information. To help reduce the computational time, the regions of the images outside the area of interest (areas without the speckle pattern applied) are masked off. Next, a starting point is automatically calculated by the software, with operator verification to ensure the point is the same in the left and right image. Finally, the software computes the project, calculating the position, strain, displacement values, etc. for each stage.

3.2.7.2. Analysis Mode.

In analysis mode, the user can observe the strain output and extract data from specified points. By default, the fields of the strain, position, displacement, etc. are displayed using a color contour plot. The scale is adjusted to get the best resolution in the areas of interest. All of the directional displacements, etc. are displayed with respect to a local coordinate system assigned by the software using a datum coordinate system. For the panels, this didn't necessarily correspond to the longitudinal and transverse directions needed for measurement of the in-plane strains. The coordinate system for each panel is re-specified by first defining a combination of primitive planes and points. The distance between the edge of the speckle pattern mask and the panel is measured for the respective panel. After defining the plane, applied to the surface of the panel using "best fit", points are projected onto the plane which corresponds to the left-hand edge of

the panel, in the middle, and at the edge of the mask where the manual measurements were taken. The coordinate system was then re-located to the mask edge, which enables definition of a point at a specified distance (determined with measurements) from the origin, corresponding to the transverse centerline of the panel. The origin is re-positioned at this point, with the x-axis aligned with the longitudinal panel edge and the y-axis along the transverse centerline.

To extract a string of data points that can be used for comparison with finite element modeling output, a section line is defined down the longitudinal center of the panel (parallel to the x-axis). All data points along this line for the desired parameter (strain, displacement, etc.) are then exported to a text file for further analysis and comparison.

3.3. Influence of ARAMIS System Parameters on Strain Measurement

3.3.1. General Displacement and Strain Sensitivity.

Several parameters in the ARAMIS system, both hardware and software, affect the displacement and strain sensitivity. (Trilion Quality Systems, LLC, 2004) Values calculated based on hardware and software parameter settings used in the experiment are given in Table 3.2.

The displacement sensitivity is controlled by three factors, two of which are controllable. First, the image correlation procedure in the software yields a 1/30 pixel displacement accuracy. This parameter is fixed and cannot be changed by the user. The field of view and the digital camera resolution are the two parameters that can be controlled. Field of view is the 3-D area captured by the image, measured along the horizontal and vertical image axis. For example, the field of view used for panel testing

was roughly 0.3 m. Each pixel, then, captures a fraction of the total distance along the axis, defined as the spatial resolution. Multiplying this value by the displacement accuracy (1/30 pixel), yields the displacement sensitivity.

Table 3.2. ARAMIS Displacement & Strain Sensitivity/Accuracy

Displacement	
Field of View* (Using a 50mm Lens)	0.3 m
Sensor Dimension (Pixels)	2048 x 2048
Spatial Resolution (mm/pixel)	0.147
Interpolation Accuracy (Pixel)	1/30
Overall Accuracy	1/61440
Displacement Accuracy (μm)	4.89
Strain	
Facet Size* (pixels)	15
Step Size* (pixels)	7
Strain Length* (data points)	3 x 3
Gauge Length (pixels)	28
Gauge Length (mm)	4.1

* Parameters values used during testing and data processing

Four parameters control the strain resolution. The first three, facet size, step size, and strain length, determine the gauge length in pixels (independent of the field of view). The pixel gauge length is calculated according to the following relation: Gauge Length=(Facet Size-1)+Facet Step(Strain Length-1). The field of view, then, will determine the physical gauge length.

3.3.2. Parameter Tradeoff Study.

A short tradeoff study is conducted for each of the parameters mentioned above and also for the filtering level. All measurements are taken using data collected from panel #696 loaded at approximately 66.72 kN.

3.3.2.1. Facet Size.

Three different facet sizes are evaluated: 19, 15, and 11 pixels. The step size is held at 9 pixels and the strain length is 3 x 3. A segment of the data collected is given in Figure 3.9. The oscillation in the data is seen to increase for 11-pixel facets. Additionally, the data appears to lose correlation with the other two curves. Data for the facet sizes 15 and 19 pixels correlates better. Both show similar trends; however, the 15 pixel values appear to be slightly lower than those of the 19 pixel facets. This is counter-intuitive; a reasonable explanation cannot be provided. Although not apparent in the data provided, at 11 pixels, the software began having troubles correlating the speckle pattern: 38 holes existed, compared to only a few under normal circumstances. Facet size had no effect on the facet field size (number of facets in the measured area), which remained 226 x 226 for each iteration. Facet overlap did increase though, with increasing facet size.

3.3.2.2. Step Length.

The step length is the distance from the edge of one facet to the corresponding edge of an adjacent facet. Step length is the primary variable that determines the number of facets (field size) on the measured surface. For this study, data for step sizes of 17, 15, and 11 facets is collected. The resulting size of the facet field is 120 x 120, 136 x 136, and 185 x 185, respectively. The results are displayed in Figure 3.8. It appears that the step effect of step length on data variability isn't as pronounced as that of the facet size. The curves corresponding to all three values show similar trends, especially in the areas of significant troughs or peaks. As the step length is increased, it appears to have a dampening effect. This is presumably due to the step length's influence in the on the effective strain length. While the variation for the 11 pixel step length is higher, the magnitude of the peaks and troughs are relatively higher. If areas of high strain gradient are expected, a shorter step length may be useful in capturing its characteristics.

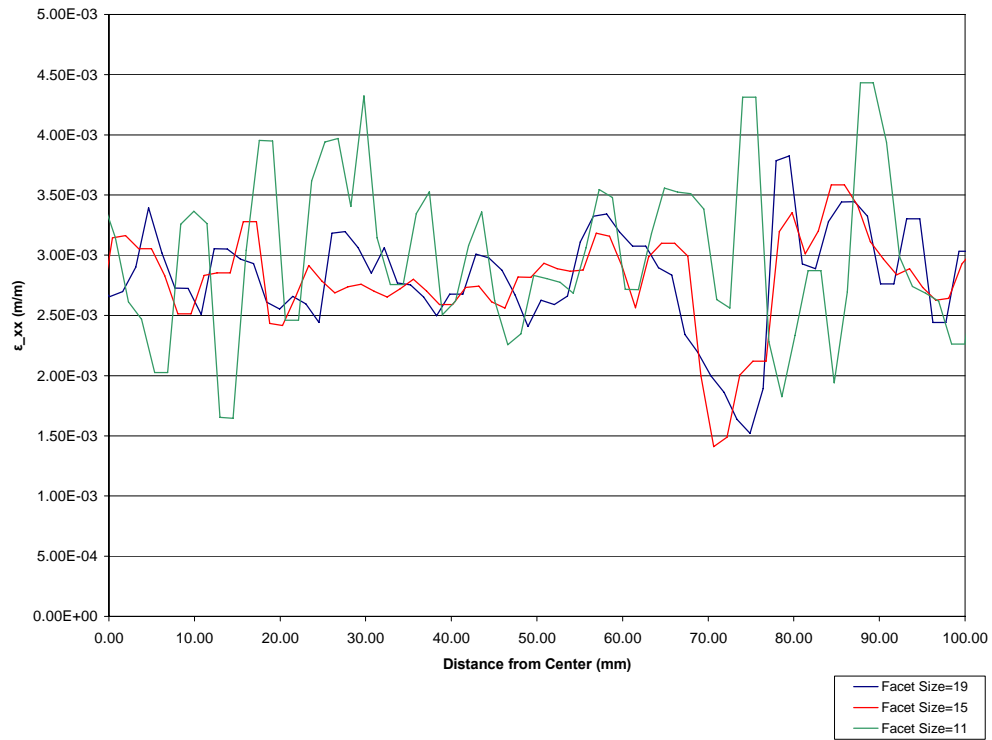


Figure 3.9. Facet Size Variation Effects

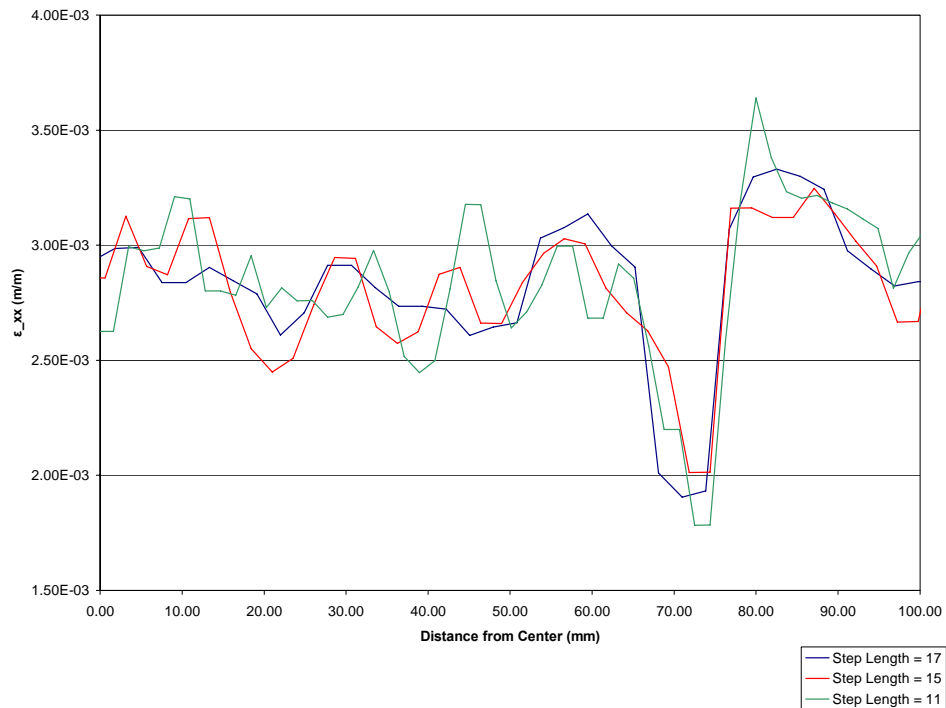


Figure 3.8. Step Length Variation Effects

3.3.2.3. Strain Length.

Only two different strain field sizes are studied: 3 x 3 and 5 x 5 data points. Results are shown in Figure 3.10. The primary effect of the larger strain length, it appears, is a damping of the strain values. The penalty of increased noise, seen with lower values previously, doesn't seem to exist with strain length.

3.3.2.4. Filtering.

The final tradeoff study involves a look at data filtering methods available in ARAMIS. What we'll call "tiger striping", evident in Figure 3.11, doesn't appear to be a true physical phenomenon and demonstrates a clear need for some level of filtering to remove noise present in the data. Two primary options are available to the ARAMIS user. Averaging, replaces a data point with the mean value of data points in the neighborhood of that point. The other option, median filtering, operates on a similar

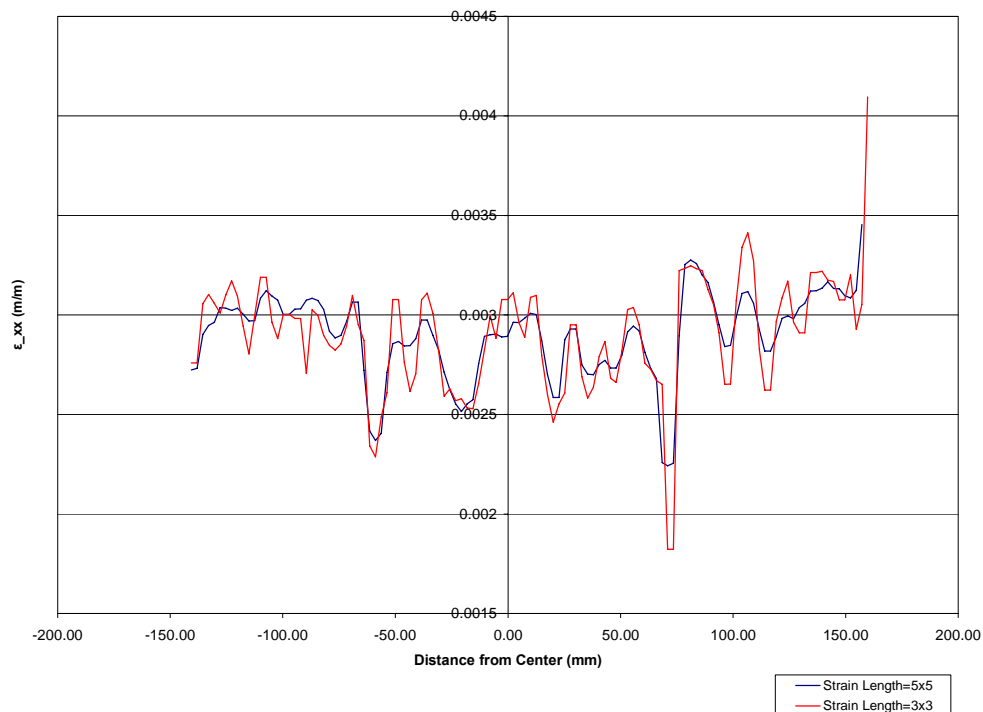


Figure 3.10. Strain Length Variation Effects

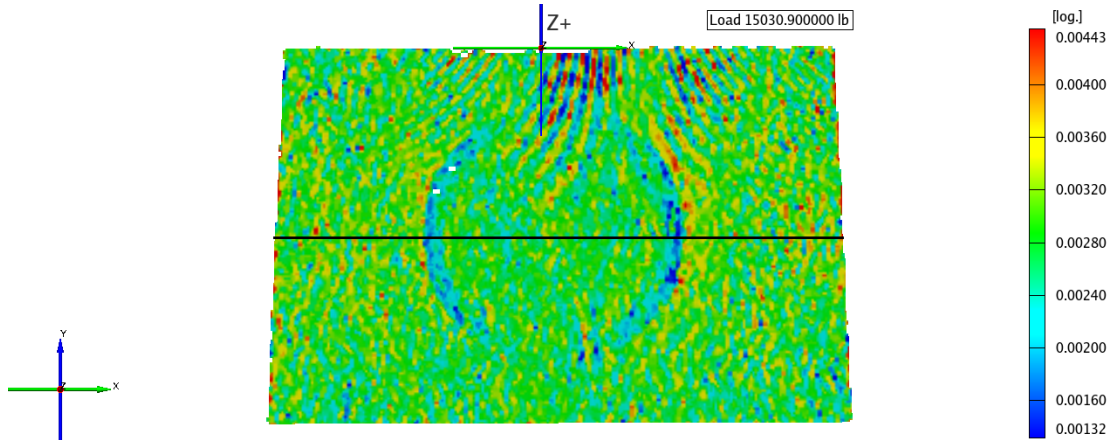


Figure 3.11. Un-filtered ϵ_{xx}

principle, except that instead of finding the mean, the median value of existing data points is determined. This latter option has an advantage in that it replaces a data point with another observed data point; no new data values are introduced. Median filtering is very good at filtering out sporadic random noise while still preserving the data trend. The focus of this tradeoff study will be the median filter, chosen for the benefits mentioned.

Initially, the filter size is held constant at three and the number of filter repetitions (runs) is varied. After seeing only insignificant changes in the first three values, both the number of runs (13) and the size of the filter (7) are dramatically increased. The results are displayed in Figure 3.12. As anticipated, the median filter does an excellent job in preserving the trends. There appears to be no shift in the location of the trough; only the relative magnitude varies. Additionally, there seems to be a “squaring” of the peaks with increasing number of runs and/or size. Finally, there is a general smoothing of the curve.



Figure 3.12. Variation Effects of Filter Runs and Size

3.3.2.5. Parameter Selection.

For analysis of the data, a 15 pixel facet size, 7 pixel step size, and a 3x3 strain length are used. Additionally, a 12 x 5 median filter is chosen for the longitudinal strain, while a 13 x 7 filter is select for both the lateral and shear strain. The “larger” filter for the latter two is needed since these strains are lower, resulting in a higher noise content in the data.

IV. Finite Element Analysis

The use of digital image correlation photogrammetry for experimental measurement yields a full-field picture of the strain on the top and bottom of the panel surfaces. However, to gain insight into the strain behavior of the panel, the patch, and the adhesive interface below the surface, we must model the patched panel numerically using a finite element model. The development of the finite element model is examined in this chapter.

4.1. Geometry and Material of the Finite Element Model

4.1.1. Global Dimensions

The dimensions of panel number 696, given in Table 4.1 and Table 4.2 are used as the basis for the finite element model geometry. The thickness is an average, measured at four points located 51 mm from the panel's center. A deep throat micrometer with a flat anvil interface is used to take the measurements. A micrometer with a double ball interface, usually used for thickness measurements, wasn't available. To ensure an accurate measurement, special care was taken to make sure the micrometer was perpendicular to the surface. Additionally, the average of several readings at each point is used.

Table 4.1. FE Model: Panel Dimensions

	(mm)
Average Ply Thickness	0.141
Panel Thickness	2.301
Panel Length'	457.200
Panel Width	203.200
Inner Scarf Diameter	17.424
Outer Scarf Diameter	128.575

Table 4.2. FE Model: Patch Layer Dimensions

Layer #	Diameter (mm)
1	17.424
2	24.765
3	31.699
4	36.881
5	41.504
6	48.158
7	54.000
8	60.223
9	66.319
10	72.136
11	79.121
12	85.141
13	91.110
14	97.587
15	103.683
16	111.862
17	141.275

4.1.2. Material Properties.

The properties used for AS4/3501-1, given in Table 4.3, are based on experimental data (as indicated) supplied by the Air Force Research Laboratory, AFRL/MLBC. The experimental findings of Capt Cook (Cook, 2005) are used for the properties of the adhesive, FM 300M (.05 psf).

Table 4.3. FE Model: Material Properties

AS4/3501-6		FM 300M (.05 psf)	
E_{11}^* , GPa	137.896	E, GPa	3.121
E_{22}^* , GPa	10.342	G^* , GPa	1.131
E_{33} , GPa	10.342	ν^*	0.38
E_{12}^* , GPa	5.516		
E_{13} , GPa	5.516		
E_{23}^* , GPa	3.103		
ν_{12}^*	0.30		
ν_{23}	0.67		

* - Denotes Experimental Data

To determine the remaining engineering constants for the lamina (ply), the material is assumed to be transversely isotropic, with X_2X_3 the plane of isotropy. Then $E_3=E_2$, $G_{13}=G_{12}$, and $\nu_{13}=\nu_{12}$. Additionally, we can say that

$$G_{23} = \frac{E_2}{2(1+\nu_{23})} \quad (4.1)$$

which can be solved for ν_{23} . Finally, because of the symmetry of the compliance matrix, we can say that

$$\frac{\nu_{21}}{E_2} = \frac{\nu_{12}}{E_1} \quad \frac{\nu_{31}}{E_3} = \frac{\nu_{13}}{E_1} \quad \frac{\nu_{23}}{E_2} = \frac{\nu_{32}}{E_3} \quad (4.2)$$

In ABAQUS, properties for the lamina with individual fiber orientations, within the laminate, are defined in the laminate (global) coordinate system using the stiffness coefficients for an anisotropic material. Using the engineering constants above, we first determine the compliance coefficients $[S_{ij}]$ in the lamina (local) coordinate system

$$\begin{aligned}
S_{11} &= \frac{1}{E_{11}} & S_{12} &= -\frac{\nu_{21}}{E_2} & S_{13} &= -\frac{\nu_{31}}{E_3} \\
S_{12} &= -\frac{\nu_{12}}{E_1} & S_{22} &= \frac{1}{E_{22}} & S_{23} &= -\frac{\nu_{32}}{E_3} \\
S_{31} &= -\frac{\nu_{13}}{E_1} & S_{32} &= -\frac{\nu_{23}}{E_2} & S_{33} &= \frac{1}{E_{33}} \\
S_{44} &= \frac{1}{G_{23}} & S_{55} &= \frac{1}{G_{13}} & S_{66} &= \frac{1}{G_{12}}
\end{aligned} \tag{4.3}$$

Then, compliance coefficients $[S_{ij}]$ are transformed to the laminate coordinate system (denoted as $[\bar{S}_{ij}]$) by

$$[\bar{S}_{ij}] = [T_2]^{-1} [S] [T_1] \tag{4.4}$$

where, using $m = \cos\theta$ and $n = \sin\theta$,

$$[T_1] = \begin{bmatrix} m^2 & n^2 & 0 & 0 & 0 & 2mn \\ n^2 & m^2 & 0 & 0 & 0 & -2mn \\ 0 & 0 & 1 & 0 & 0 & 0 \\ 0 & 0 & 0 & m & -n & 0 \\ 0 & 0 & 0 & n & m & 0 \\ -mn & mn & 0 & 0 & 0 & m^2 - n^2 \end{bmatrix} \tag{4.5}$$

and

$$[T_2] = \begin{bmatrix} m^2 & n^2 & 0 & 0 & 0 & mn \\ n^2 & m^2 & 0 & 0 & 0 & -mn \\ 0 & 0 & 1 & 0 & 0 & 0 \\ 0 & 0 & 0 & m & -n & 0 \\ 0 & 0 & 0 & n & m & 0 \\ -2mn & 2mn & 0 & 0 & 0 & m^2 - n^2 \end{bmatrix} \tag{4.6}$$

Finally, the stiffness coefficients in the laminate coordinate system are found by

$$[\bar{C}_{ij}] = [\bar{S}_{ij}]^{-1}. \text{ (Herakovich, 1998)}$$

It's important to note ABAQUS uses a different arrangement for the stiffness coefficient matrix. Using the notation above, the ABAQUS matrix has the number four row and column switched with the number six row and column.

4.2. Model Definition in ABAQUS

The solid modeling feature was used in ABAQUS to define the geometry of the panel, the adhesive, the patch, and the overply (Figure 4.1).

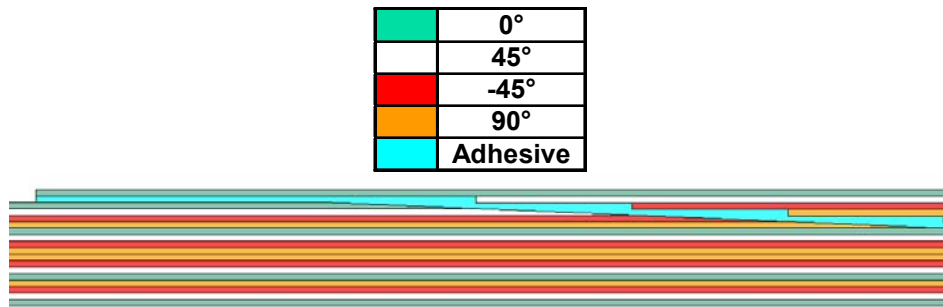


Figure 4.1. Scarf Joint Cross Section.

As discussed in Chapter 1, most models created to model scarf joint behavior use smoothly tapered sides for both the patch and the panel. While this may reflect a joint created during manufacturing, it doesn't represent the interface of a scarf repair. To more accurately model the joint, the panel is smoothly tapered, but the patch exhibits a taper comprised of discrete steps. Admittedly, the approximation of a smooth taper on both sides may be an adequate approximation for the elastic range being examined; no studies have been found that validate this assumption. To prevent any gaps between the adhesive and the patch, the adhesive is first defined as a solid cone. Then, as the individual parts are assembled in the ABAQUS Assembly Module, Boolean operations are used to subtract material from the adhesive in the region that's occupied by the patch.

Once the panel is assembled, the assembly must be merged to ensure a continuous mesh. If the individual parts were not merged, tie elements would have to be used at

each part interface, greatly increasing the complexity of the model and reducing its accuracy (*Analysis/CAE users manual*2006). Despite the merging process, the boundaries of each separate part are retained as model partitions, allowing assignment of different material properties to different regions defined by the partition. Partitions are respected as a boundary during automated meshing, as well. Using the partition feature, the panel and the patch are further divided up into sixteen separate layers to represent the individual plies. A separate set of material properties, each representing properties in the global coordinate system for a given fiber orientation, are assigned to each layer (lamina), to include the 0°overply. The adhesive is modeled as an isotropic material exhibiting pure elastic behavior. Although numerous studies, some of which are discussed in Chapter 1, have pointed to the significance of the adhesive non-linearity in determining the joint strength, such an investigation is beyond the scope of this study.

4.3. Boundary and Loading Conditions

At the end of the panel in the $x=0$ plane, a pressure load is created which simulates the 44.48 kN (10k lbf) load applied by the load frame during testing. The pressure magnitude is determined by dividing the applied load by the end plane surface area. The response to different load values can then be determined by scaling this load (done in ABAQUS using load case). For this study, a scaling factor of 1.5 (yields 66.72 kN) is used to bring the equivalent load equal to the load used in the experimental analysis.

At the $x=0$ end, all degrees of freedom are fixed except U1, which corresponds to the direction of the applied load, and rotation about the z-axis R3, which simulates conditions of the test equipment. At the other end, located at $x=457.200$, only R3 is unconstrained. Note that although boundary conditions during actual testing probably

had some flexibility, using fixed-fixed conditions in the model were a closer approximation than would be a pinned-pinned condition. With more time, the boundary conditions could have been more closely approximated using spring elements at the boundaries.

4.4. Finite Element Model Definition

The small thickness of the individual ply, several orders of magnitude smaller than the global panel dimensions, created a challenge in achieving a good mesh with relatively few elements.

4.4.1. Model Meshing.

Before a mesh could be created, several variables must be defined in the model. First, a global mesh seed of 1.44 mm was applied to the model – ten times the lamina thickness. A global seed applies a default element length along every edge in the model. This size, however, by default, is not fixed; it's treated purely as a recommendation. During the automatic meshing routine, ABAQUS will adjust the size accordingly to reach an adequate meshing solution. This size was chosen to help reduce the size of the model without significantly affecting accuracy. Its effect on accuracy will be examined later using a convergence study.

Next, a meshing routine and the general element class to be used must be defined. Choices made here, have a big impact on the quality of the mesh and the number elements created. The general element class choices available for this model were 1) Hexahedral (Hex) Only; 2) Hex Dominated, which allows for wedge and tetrahedral (Tet) elements; 3) Wedge; and 4) Tet elements. Generally, hexahedral elements are more

accurate than either wedge or tet elements of the same characteristic length. The latter two tend to be overly stiff.

The meshing methods available are swept and structured. Within each of these, the algorithm used to develop the mesh can be specified as either *medial axis* or *advancing front*. Refer to the ABAQUS/CAE User's Manual (*Analysis/CAE users manual*2006) for further information on the techniques available. The final meshing routine selected used swept meshing with the advancing front algorithm. This minimized the number of errors and warnings (both zero), and the number of elements with shape problems such as aspect ratio, minimum angle, and maximum angle.

Finally, the last parameter requiring specification before mesh generation is the polynomial order of the element: either linear or quadratic. Three-dimensional quadratic iso-parametric hexahedral elements with reduced integration, C3D20R, and wedge elements, C3D15, are selected for several reasons (Figure 4.2). First, the linear elements have the tendency to exhibit spurious shear strains in bending, leading to an overly stiff structure. Although this model is loaded in uni-axial tension, due to the asymmetry in the patch region, some level of bending will be present. Element sensitivity to distortion is

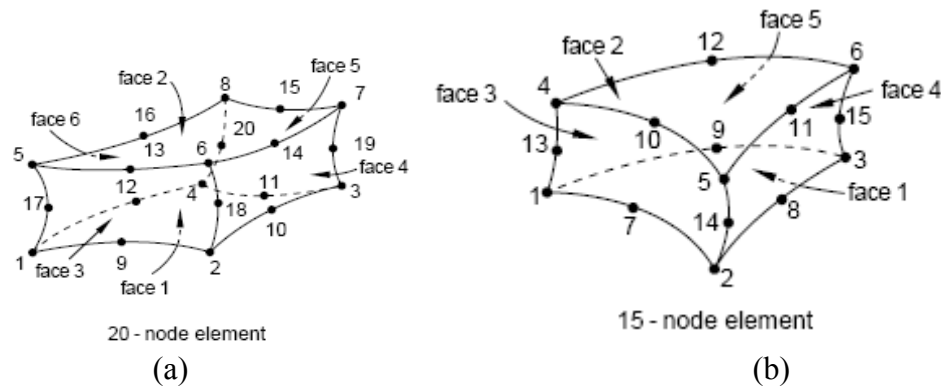


Figure 4.2. Basic Element Shapes Used (ABAQUS, 2006)

the next consideration in element selection. Reduced integration linear elements, designed to overcome problems with spurious shear strain, have very poor accuracy when they have either parallelogram or trapezoidal initial element shapes. Because of the extremely shallow scarf angle (2° - 3°), it's probable that many elements will exhibit one of these shapes. According to the ABAQUS Benchmark Manual (*ABAQUS benchmarks manual*2006), both regular and reduced integration linear elements show strong sensitivity to initial shape distortions. For the quadratic reduced integration element, the ratio of the predicted tip deflection of a cantilever beam compared to the Euler-Bernoulli theoretical value is between 0.896 and 1.001, depending on the skew angle. For linear 3-D elements, this ratio is as low as 0.121. Additionally, the quadratic elements are able to mesh a curved with fewer elements than can linear elements. Reduced integration for the 3D-element reduces the size of the model. For example, a full third order Gaussian integration has 27 integration points per element. The reduced, 2nd order integration has just 8 points. A full summary of the mesh characteristics is given in Table 4.4.

Table 4.4. Mesh Characteristics Using Swept, Advancing Front Meshing

Mesh Summary		
# Elements	Hexahedral (C3D20R)	545430
	Wedge (C3D15)	30542
	Tetrahedral	0
	Total	0575972
# Nodes		2373301
# Model Variables		7,119,903
Analysis Errors		0
Analysis Warnings		708 (0.122923%)
Mesh Geometry Statistics		
Aspect Ratio> 10	Total	355668 (65.2087%)
	Average	12.13
	Worst	24.23
Min Angle <10°	Total	0
	Average	85.68°
	Worst	30.45°
Angle >160°	Total	0
	Average	94.53°
	Worst	149.21°

4.5. Reducing the Model Size

Achieving a meshed model with acceptable quality and a minimum number of elements proved to be difficult. First attempts at meshing the model resulted in as many as 2.7 million elements and 11 million nodes. This created problems with the pre- and post-processor, either excessively slowing the response to command inputs or crashing the software altogether. Even as the model was reduced small enough to allow graphical processing, problems were encountered with insufficient RAM or hard disk space to execute the model computation. Experimentation using different meshing techniques, algorithms, and partitioning finally gave a model that the computers available could process.

Often, a plate is modeled using symmetry conditions about the X_1 axis, X_2 axis, or both. This results in a model that uses only one quadrant to model stress and strain behavior in the entire plate. In this case, due to the existence of the lamina oriented at $\pm 45^\circ$, such symmetry conditions do not exist and the entire panel/patch must be modeled. Consideration was given to decreasing the length of the model to reduce the number of elements required. To investigate this possibility, a finite element model of an undamaged panel was created, using the same length, width, boundary conditions, and loading that will be used for the repaired panel. The resulting strain contours shown in Figure 4.3 indicate that while the boundary effects for the longitudinal strain dissipates quickly into a uniform strain field, the transverse strain is significant up to 76 mm from either end. To avoid interaction of the edge boundary conditions and conditions created by the patch, the decision was made to model the original length of the panel outside the tabs.

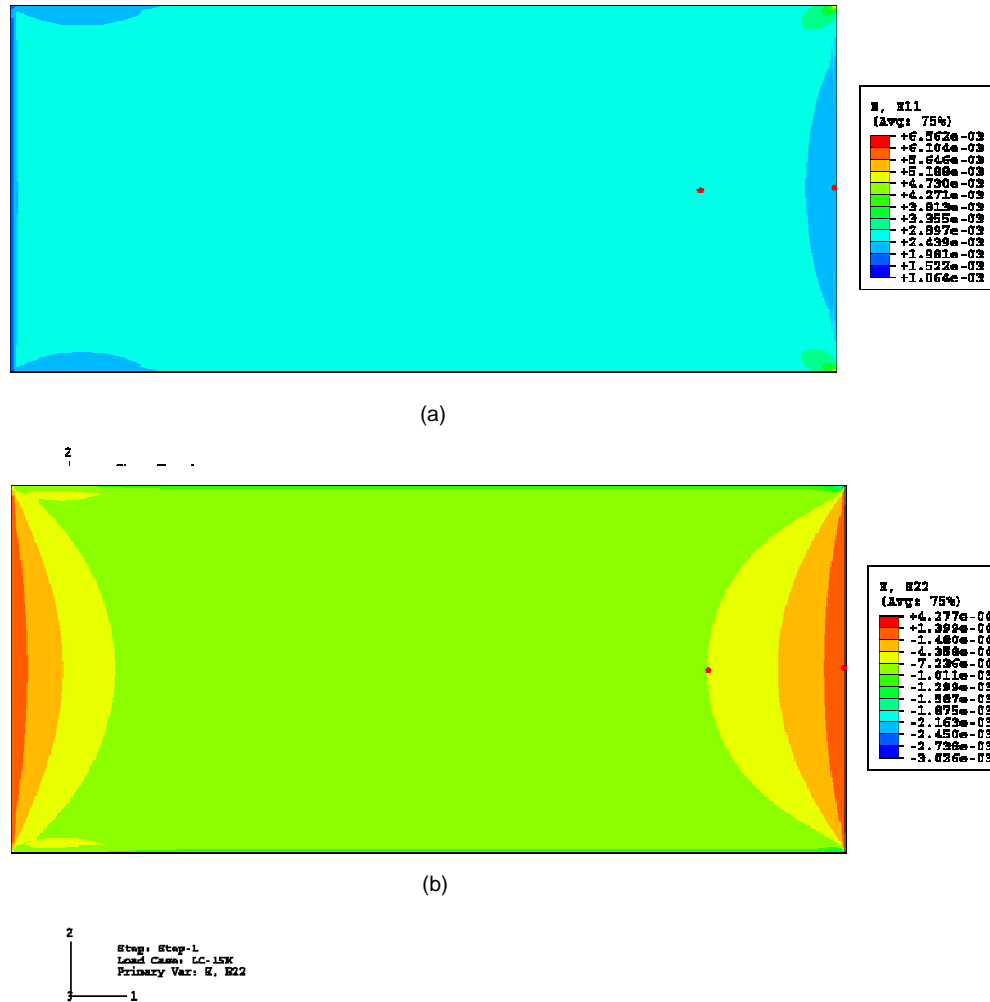


Figure 4.3. Model of Undamaged Panel: (a) ϵ_{11} ; (b) ϵ_{22}

To further reduce the number of elements in the model, the last three inches on either end of the panel were partitioned. In these regions, the edges were seeded with an element size of 2.88 mm, or 20 times the lamina thickness. This should have little effect on the accuracy of the solution in the area of interest in the immediate vicinity of the patch because it's well-removed from the patch region, the geometry in this region is uniform, and bending is less-pronounced. This reduced the number of elements in the

model by 93 thousand elements. The element quantities in Table 4.4 reflect these changes.

The final model was successfully run on a Linux-based system running 7 hours 52 minutes, using 12 CPUs. The ABAQUS/Standard solver required 36.82 giga-bytes of RAM.

4.6. Model Convergence

4.6.1. Convergence Model Geometry.

Due to the complexity of the model, geometric limitations (lamina thickness), and processing time, a traditional coarse to fine convergence study wasn't feasible.

Alternatively, a convergence study is performed using a plate with a hole of similar size to the scarf model. Comparison of the finite element solution to a known theoretical solution for an infinite plate will give an indication of the element's ability accurately predict stresses and strains around a discontinuity such as a hole. Although this lacks much of the scarf patch model's complexity, it is a reasonable indicator.

The panel is a $[0^\circ/90]_s$ layup, with lamina material and thickness identical to the scarf patch model. The absence of the 45° orientations allows us to take advantage of the symmetry conditions and model only a quarter plate (Figure 4.4). The width was initially set equal to the test panel width. However, after running the model, it was determined that the small net section resulted in an abnormally high stress concentration. The plate was widened to bring the model closer to an "infinite width" condition, assumed by the analytical solution. Final dimensions of the panel are 152 mm along the loading axis and 508 mm along the transverse axis. The hole is roughly the same diameter as the outer

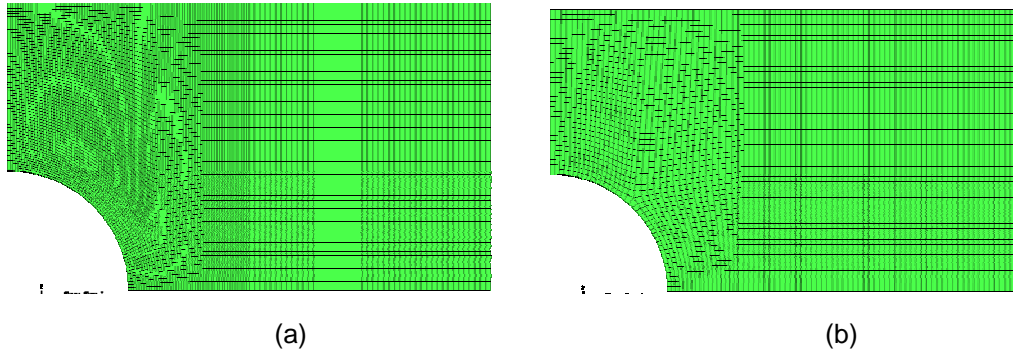


Figure 4.4. Quarter Plate Geometry: (a) Mesh Seed $10t_i$; (b) Mesh Seed $20t_i$

scarf diameter (64 mm). Loading is picked arbitrarily at 45.5 Pa, representing an 89 kN load distributed uniformly across the panel edge.

The model was partitioned into three areas. The inside area is representative of the experimental panel width. This region is meshed using three different global seed sizes, 3, 10, 20, given as multiples of lamina thickness (.1397 mm). The latter two are representative of seed sizes used in the model. The average/worst aspect ratios of the three models are 4.79/13.37, 13.32/21.31, and 21.59/31.13, respectively. For all three models, the seed size in the middle region, the transition region, is fixed at 10. A relatively coarse mesh is prescribed in the outside region using a seed size of 20.

4.6.2. Analytical Solution.

The analytical solution is determined using classical laminate theory. Using the laminate compliance matrices, the effective laminate engineering properties are determined to be

$$\bar{E}_x = 74.491 \text{ GPa}$$

$$\bar{E}_y = 74.491 \text{ GPa}$$

$$\bar{G}_{xy} = 5.516 \text{ GPa}$$

$$\bar{\nu}_{xy} = 0.0419$$

The prediction of the stress concentration around a hole in an infinite composite plate is given by Daniel and Ishai (Daniel & Ishai, 1994):

$$k_\sigma = \frac{\bar{\sigma}_{\max}}{\bar{\sigma}_o} = 1 + \sqrt{2 \left[\sqrt{\frac{\bar{E}_x}{\bar{E}_y}} - \bar{\nu}_{xy} \right] + \frac{\bar{E}_x}{\bar{G}_{xy}}} \quad (4.7)$$

where

$\bar{\sigma}_o$ = Applied far-field average stress

$\bar{\sigma}_{\max}$ = Maximum circumferential stress on hole boundary (at $\varphi=90^\circ$)

\bar{E}_x, \bar{E}_y = Average Young's moduli in x- and y-directions

\bar{G}_{xy} = Average shear modulus

$\bar{\nu}_{xy}$ = Average Poisson's Ratio

The axial stress along the y-axis can then be determined using

$$\bar{\sigma}_x(0, y = 2.5) = \bar{\sigma}_o \left(1 + \frac{1}{2} \rho^{-2} + \frac{3}{2} \rho^{-4} - \frac{k_\sigma - 3}{2} (5 \rho^{-6} - 7 \rho^{-8}) \right) \quad (4.8)$$

where

$\bar{\sigma}_x(0, y)$ = Axial stress along x-axis

$\bar{\sigma}_o$ = Applied far-field axial stress

$$\rho = \frac{y}{a}$$

a = Hole radius

k_σ = Anisotropic stress concentration factor

Using MATLAB, the following values are calculated

$$k_\sigma = 4.9270$$

$$(\bar{\sigma}_x)_{\max} = 1.54 \text{ GPa}$$

4.6.3. FEM Solution and Convergence Values

To compare the FE output to the analytical values, the strain output E_1 must first be transformed to an average laminate stress using the laminate engineering properties,

determined previously, and the mid-plane strain, ϵ_m . Ratios of the FEM average stress to the analytical stress are given in Table 4.5. Increasing the width of the model did lower the stress concentration value; however, the concentrations are still higher than predicted. With the hole still occupying 25% of the panel width, it's likely that the current test panel is still outside the “infinite plate” assumption used in calculation of the analytical value. If time permitted, the width could be increased to achieve the theoretical value. More important for this convergence study, however, is that the stress changed by only 0.75% going from the fine (3t) to medium mesh (10t), and 1.62% going from the fine to coarse mesh (20t). This is an acceptably small change.

Table 4.5. Ratio of FEM Predicted Laminate Stress to Theoretical Anisotropic Plate Prediction

FE Model Global Size (t=0.1397 mm)	$\bar{\sigma}_{fem} / \bar{\sigma}_{analytic}$
3t	1.5005
10t	1.4892
20t	1.4761

V. Results and Analysis

Examined here are the results measured experimentally using the ARAMIS digital image correlation photogrammetry system and also the finite element results. The chapter is subdivided into three focus areas. First, in an effort to validate the finite element model, the results of the finite element model are compared with experimental results of a representative panel. Second, with accuracy of the finite element established, the predictions of the finite element model are examined in-depth. The stresses beneath the surface in the regions immediately adjacent to and within the patch boundary will be looked at. Finally, the strain behavior of the different overply geometries will be compared.

In all cases examined throughout this chapter, the applied load will be equivalent to a 66.72 ± 0.44 kN load. This value, as previously discussed, is chosen in an attempt to remain within the elastic limits of the materials involved.

5.1. Comparison of Experimental Data to Finite Element Data

Elastic surface strain predictions of the finite element model are compared to the actual experimental performance of Panel #696. A combination of 2-D contour plots and line plots will be used in this evaluation of both the top and bottom panel surfaces. To enable a direct comparison, the scales of the finite element model contour plots have been adjusted to match those of the ARAMIS plots. In some cases, over-saturation of the scale on either the top or bottom end will result in white or gray areas on the plot (identified on the scale). The line plots from the ARAMIS model have been generated using data from

a section line down the middle of the plate ($y=4$). Finite element data has been collected using a path defined by nodes at the beginning and end of the path. As the section line transverses the patch, the section line continues following the top surface. In some cases, where a node isn't located precisely on the centerline, the nearest node is selected. Nodal averaging has been turned off.

5.1.1. Top Panel Surface.

As an initial indicator of model quality, the out-of-plane panel deflection (z direction) is plotted in Figure 5.1. Deflection due to bending is expected in a scarf repaired panel with a one-sided doubler. The neutral surface in the repair region is shifted due to increased thickness on one side of the panel, resulting from the doubler, and low stiffness in the joint adhesive. A bending moment results from this eccentricity between the load path and the repair's neutral surface. (ADKINS, PIPES, & Delaware Univ., 1978) Deflection in the finite element model is significantly higher than deflection of Panel #696. Ignoring the obvious rigid body displacement in the experimental values, the deflection of the finite element model is nearly four times that of the experimental panel. A possible explanation for this is the modeling of the adhesive in the patch. The adhesive was modeled at full thickness at the inner diameter of the scarf. The first ply, then, was offset by 0.127 mm - nearly a full ply thickness (0.144 mm). In reality, during patch cure, the adhesive will bleed out of this area and leave a layer much thinner than the thickness modeled. The patch, then, will conform to the lower surface in the middle of the patch, reducing the eccentricity of the load path. The 2 mm deflection of the finite element model is nearly equal to the thickness of the entire ply – pushing the envelope of the small displacement, small rotation assumptions made for this elastic model. As will be evident, however, the FEM model still does a relatively good job in predicting the elastic strain behavior of the repaired panel.

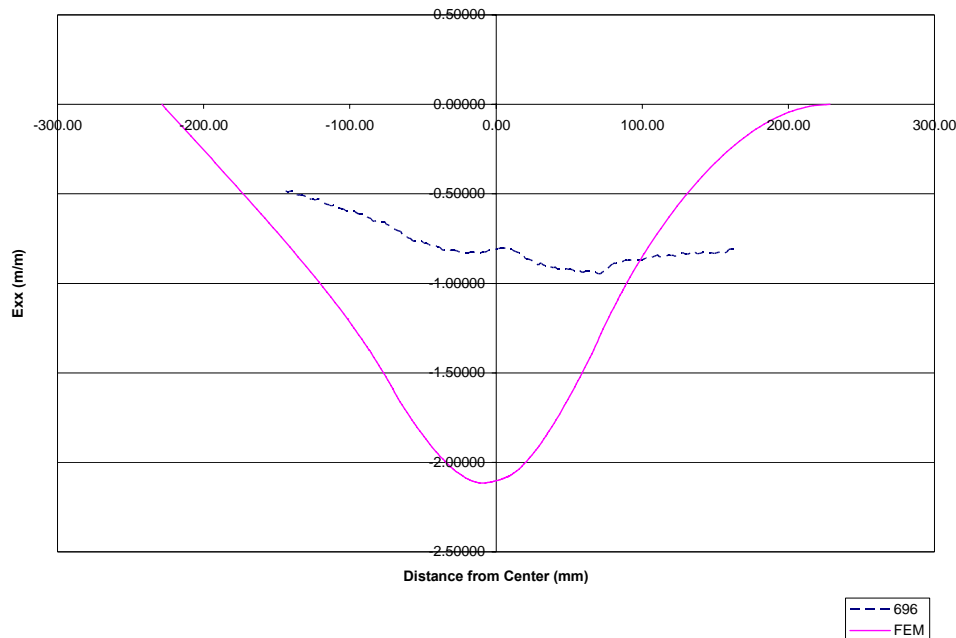


Figure 5.1. FEM vs. Experimental: Z Displacement (mm)

5.1.1.1. ϵ_{xx} .

Longitudinal strain on the panel's top surface is shown in Figure 5.4, Figure 5.5, and Figure 5.6. A qualitative comparison of the two contour plots reveals that both possess a region of lower stain in the region where the overply overlaps the panel, while just outside of this is a region of relatively high strain. This appears to be classic behavior of a single lap joint, where, along the radial length of the overlap, the load in the patch is re-introduced into the panel. In this characterization, the load has been fully re-introduced into the panel at the outside edge of the overply, resulting in very low strain in the patch. To better illustrate what's happening here, Figure 5.2 shows

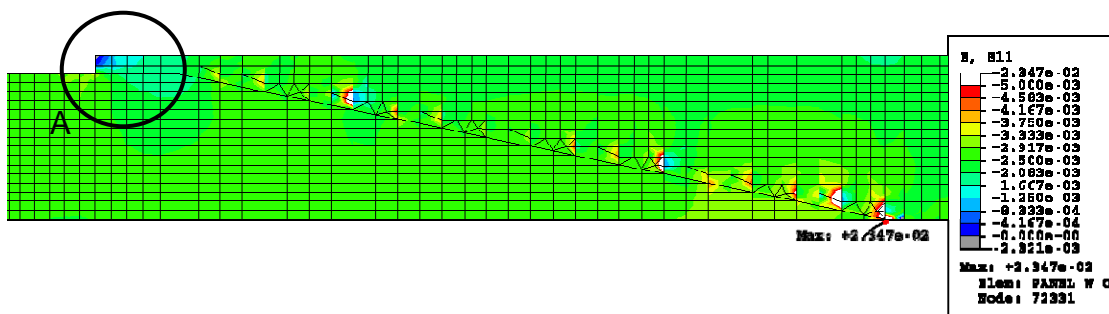


Figure 5.2. ϵ_{xx} : Center Section View, Y=4

a section view taken at $y=4$ in the finite element model. A close-up view of area in the neighborhood of the overply boundary is given in Figure 5.3.

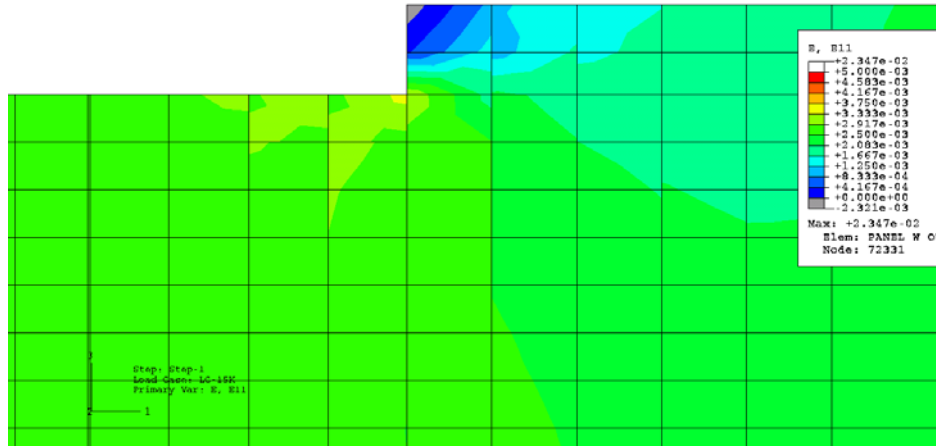


Figure 5.3. ϵ_{xx} : View A (Figure 5.2), Center Section View, XZ Plane, $Y=4$

Examining the line plots in Figure 5.6, a strain “trough” is located approximately between the edge of the scarf and the edge of the overply (measured from the center). The size the discontinuity in the FEM model is somewhat misleading: looking at the LH trough, the finite element model strain is just 80% higher than the experimental strain. This difference in peak magnitude may be attributed to several factors. First, as previously discussed, the equivalent strain gauge length on the ARAMIS system is roughly 4.1 mm. With the distance between the overply edge and scarf edge only 6 mm, any peak value would be averaged out. Second, the “plateaus” in the peaks of the experimental data are characteristic of the median filtering used on the data. Relatively wide plateaus in this region indicate the data was “smoothed” and any relatively high amplitude signal may have been attenuated.

Besides the peak magnitude discrepancy, the two curves show relatively good agreement. Both show the same general trend. At the local peaks just inside the scarf

boundary, for example, the strain magnitude predicted by the finite element model is just 14.3% lower than the experimental value. Not that it appears that the experimental data may be slightly shifted uniformly to the right. This is possible, since the reference coordinate system for the experimental data is set manually in the post-processing, and may be subject to slight error.

5.1.1.2. ϵ_{yy} .

Aside from the area of relatively higher strain in the center of the patch, few apparent similarities exist between the contour plots for the experimental and finite element data shown in Figure 5.7 and Figure 5.8. The centerline plot (Figure 5.9) provides a slightly better picture. First, as seen in the contour plots, there is excellent agreement in strain magnitude at the center of the patch. The scale on this plot is slightly deceiving, however. What looks like a large discrepancy out towards the ends of the experimental data is actually relatively close. At $x=-142$, for example, the finite element strain is only 26% higher than the experimental value. On either end, the finite element strain goes to zero, as would be expected since the longitudinal load that creates the transverse strains has not fully developed.

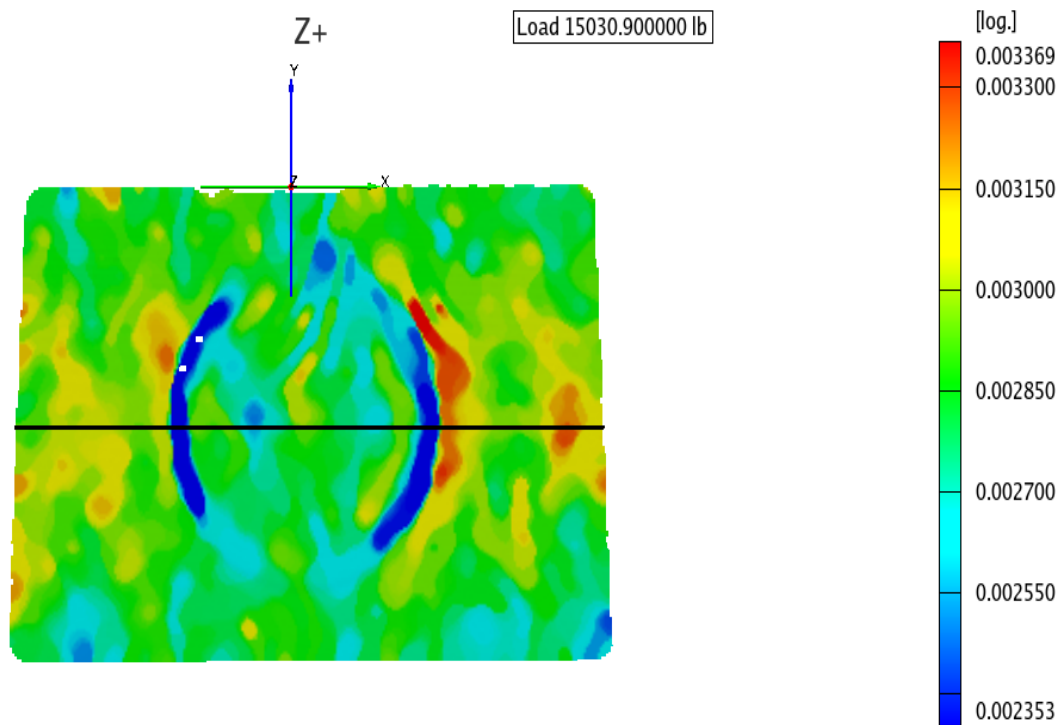


Figure 5.4. ϵ_{xx} : Panel #696 Experimental

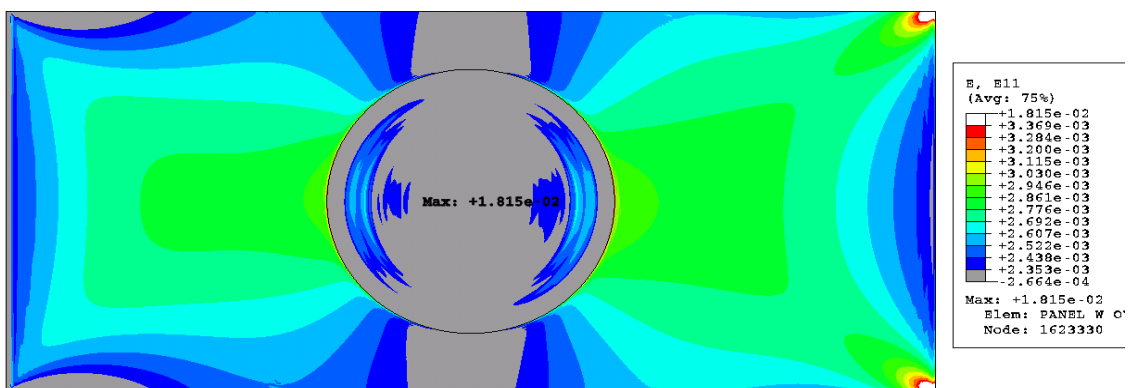


Figure 5.5. ϵ_{xx} : Finite Element Model

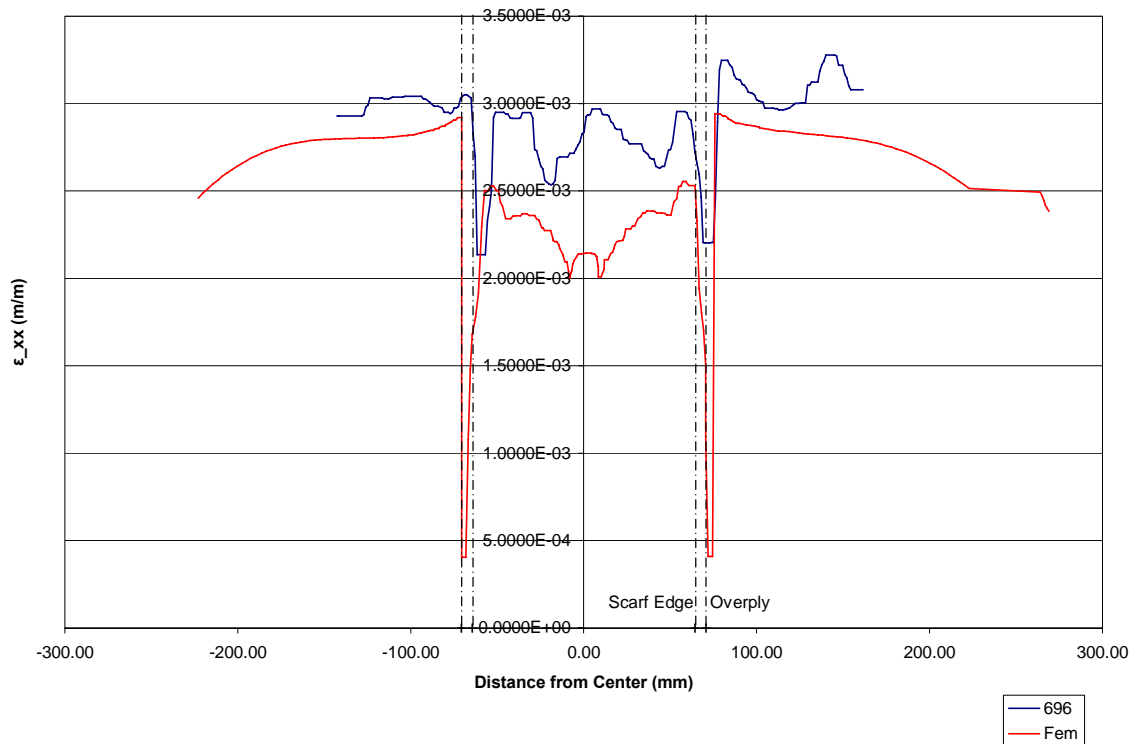


Figure 5.6. ϵ_{xx} : Data Plot, $y=4$, Experimental vs. Finite Element Model

5.1.1.3. ϵ_{xy} .

Although difficult to determine the exact values because of over-saturation, the contour plots of the shear strain show similar trends. If a section line were rotated 45° counter-clockwise from the y -axis, there is a region of negative shear adjacent (radially outward) to a region of relatively high positive shear. In the FEM contour, the negative shear is shown in grey (over-saturation on the low end). Rotating the counterclockwise, we notice a similar pattern, but in reverse. The region of high positive shear, here, is radially inside the region of negative shear. The FEM contour, here, is oversaturated on the high side, showing up white.

Unlike ϵ_{yy} , however, the line plots in Figure 5.12 don't improve the picture. Although the strains are clearly higher in the regions just discussed, I was unable to precisely locate a section line through this region. Added to this is the inability to precisely locate a similar path in the finite element model. Unfortunately, using the centerline, which can be positioned precisely, results in data which is poor for comparison. The maximum strain magnitudes recorded experimentally are less than 100 $\mu\epsilon$, while most are less than 50 $\mu\epsilon$ levels. Although a noise floor measurement wasn't taken for this experiment, the noise floor of the system is typically slightly lower than 50-100 $\mu\epsilon$. In the middle of the panel, the strain varies by just 40 $\mu\epsilon$. Magnitudes of strain in the overlap region located 65 mm from the repair's center differ by just 13 $\mu\epsilon$. Additionally, the relatively large "plateaus" in the experimental data indicate a relatively large amount of the data has been filtered.

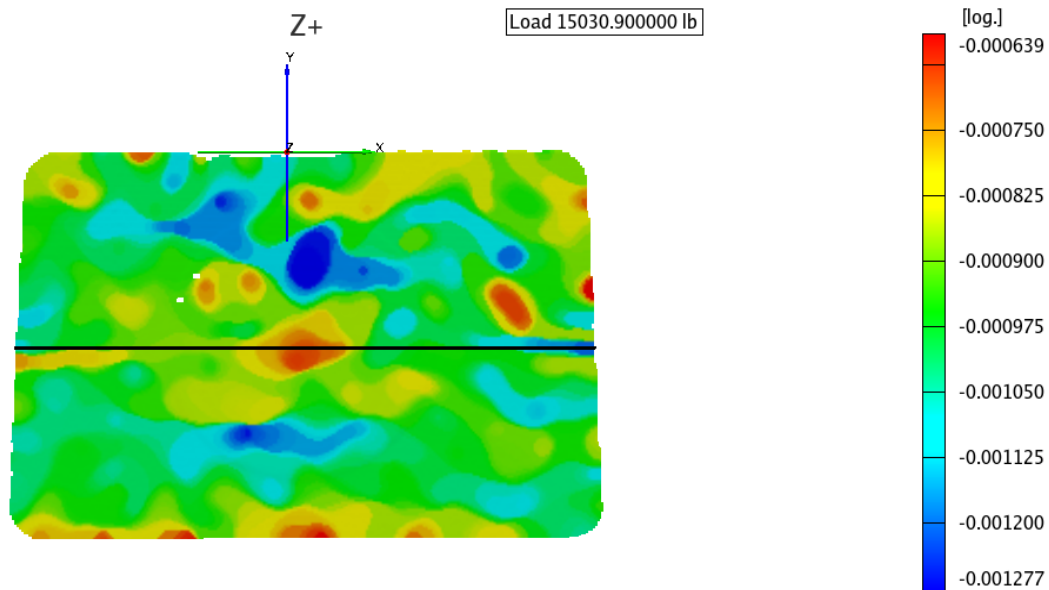


Figure 5.7. ϵ_{yy} : Panel #696 Experimental

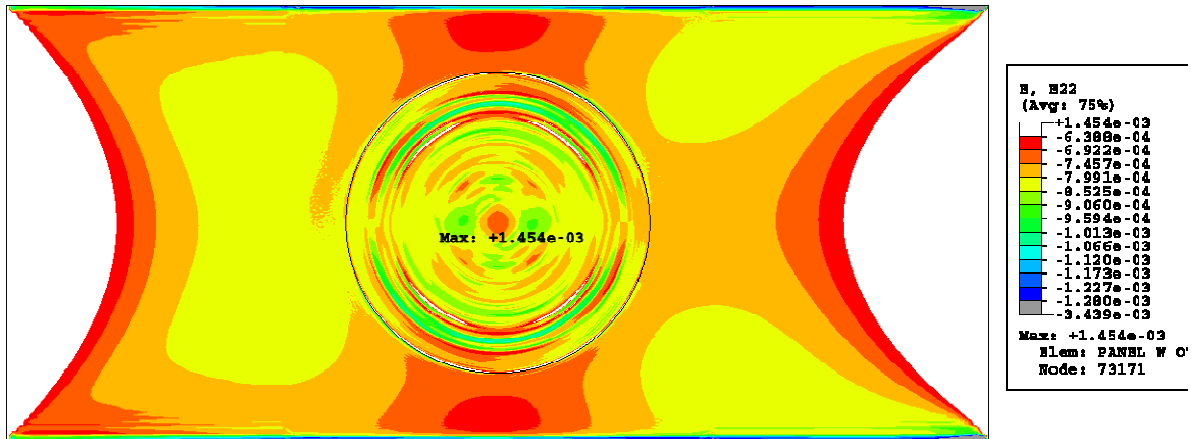


Figure 5.8. ϵ_{vv} : Finite Element Model

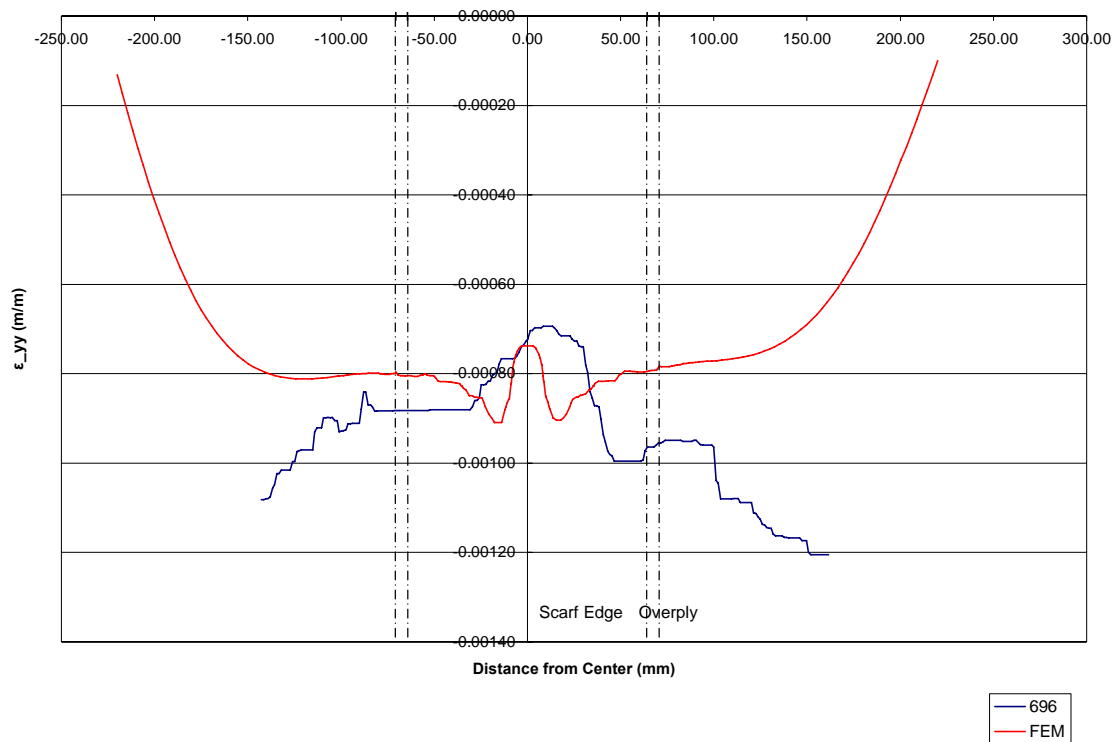


Figure 5.9. ϵ_{vv} : Data Plot, y=4, Experimental vs. Finite Element Model

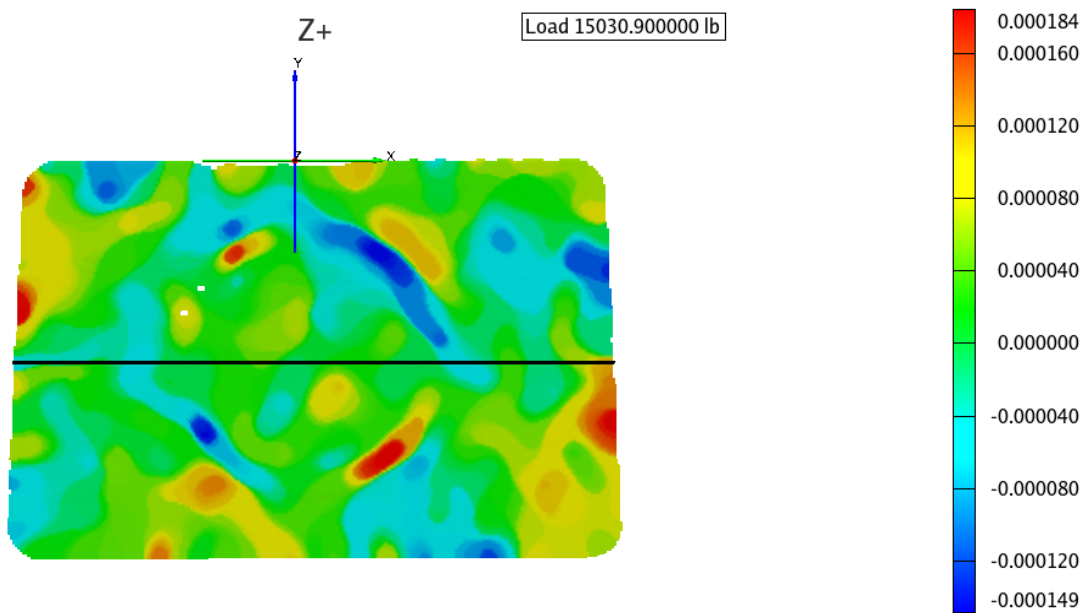


Figure 5.10. ϵ_{xy} : Panel #696 Experimental

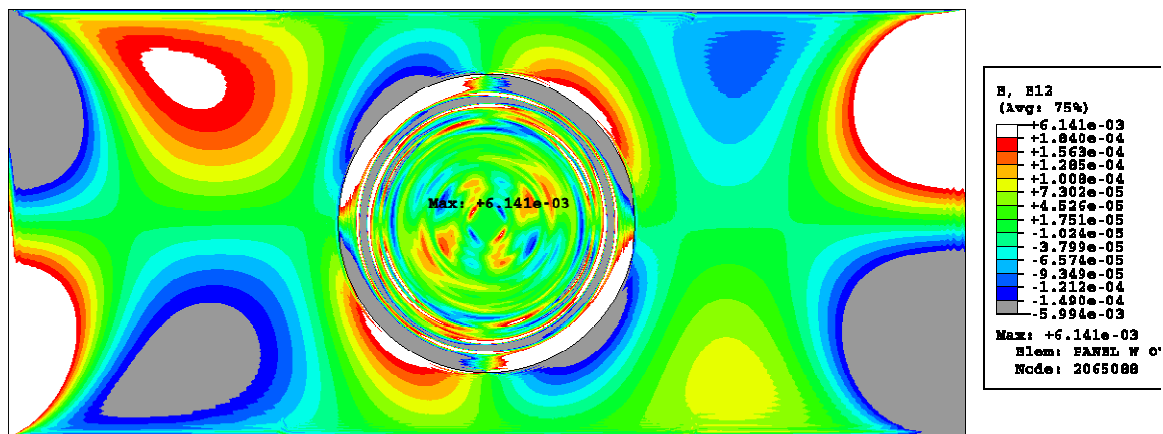


Figure 5.11. ϵ_{xy} : Finite Element Model

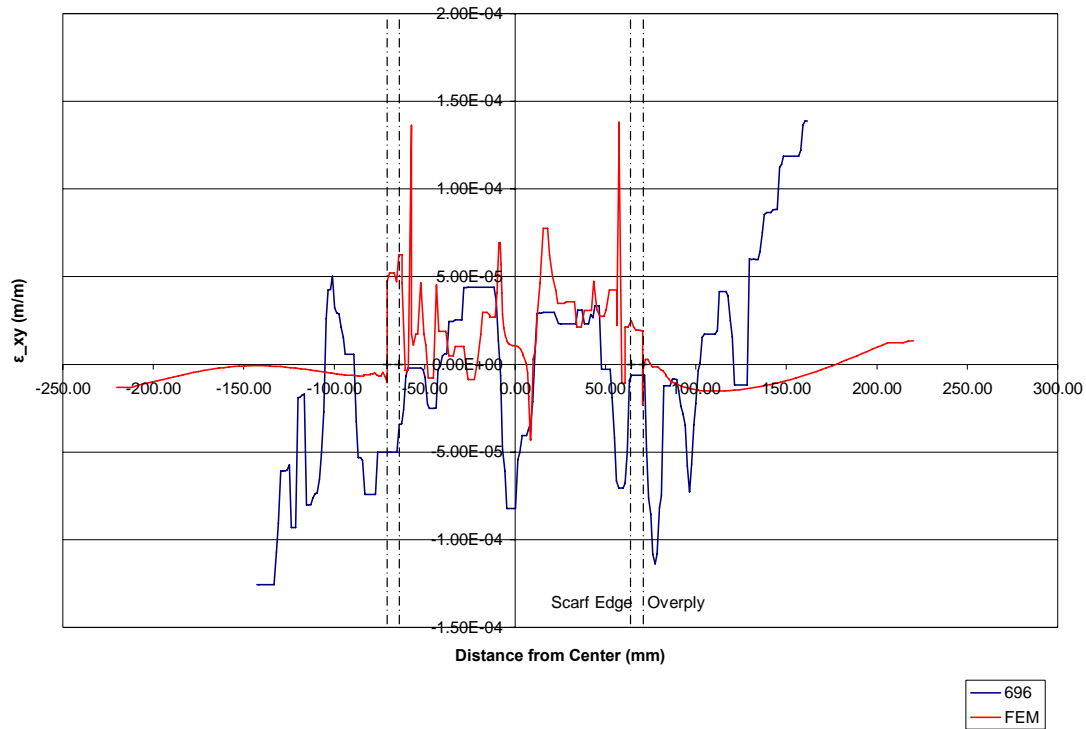


Figure 5.12. ϵ_{xy} : Data Plot, $y=4$, Experimental vs. Finite Element Model

5.1.2. Bottom Panel Surface.

Results from measurements taken on the bottom surface of the panel exhibited similar correlation; however, the variance in the data was much lower.

5.1.2.1. ϵ_{xx} .

The contour plots are shown in Figure 5.14 and Figure 5.15, while Figure 5.16 shows the data plot along the longitudinal centerline. Few conclusions, if any, can be made observing the contour plots. In fact, the finite element model indicates a region of high strain round the edge of the inner scarf diameter. No indication of such a strain level exists in the experimental contour. This may be attributable to the virtual gauge

length discussed earlier. The finite element model, however, may also be slightly inaccurate due to inaccuracies in the modeling approximation. As discussed earlier, the plate/repair was modeled with an adhesive layer on the bottom of the patch. Figure 5.13 shows a discontinuity at the sharp point created by the scarf and the relatively flexible adhesive adjacent to this point. Although the discontinuity is pronounced at the tip of the scarf, according to the model, the most pronounced discontinuity is at the first patch layer. Since this first patch layer has no overlap with adjacent plies, load is transferred in tension by the adhesive to the edge of this first layer.

Aside from the steep discontinuity at the hole boundary, the model and the experimental data agree very well. Both show similar trends. At the overply boundary at $x=-65$, for example, the finite element strain is just 16% lower than the experimental data.

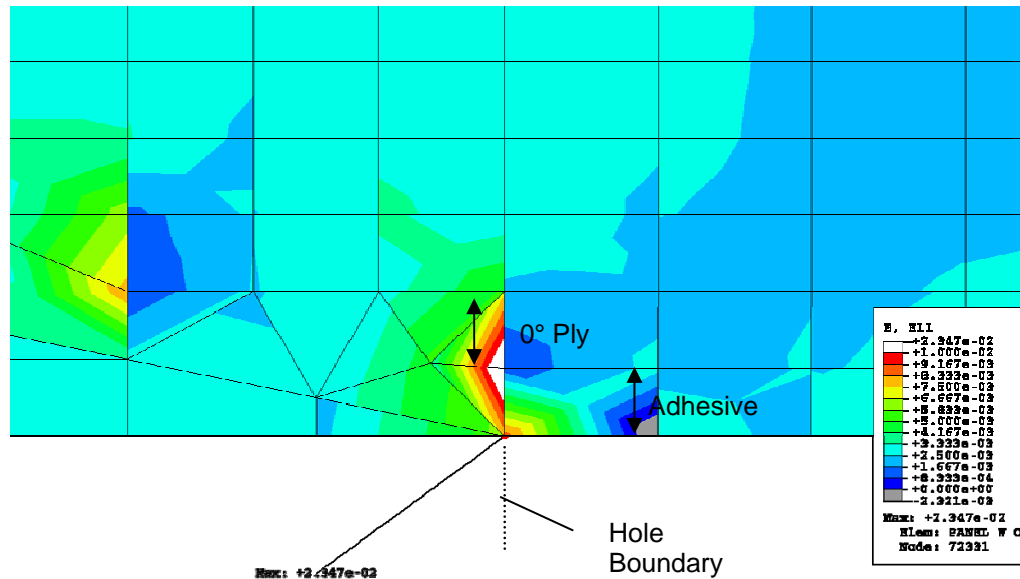


Figure 5.13. ϵ_{xx} Close-Up: Lower Surface FEM Surface at Hole Boundary

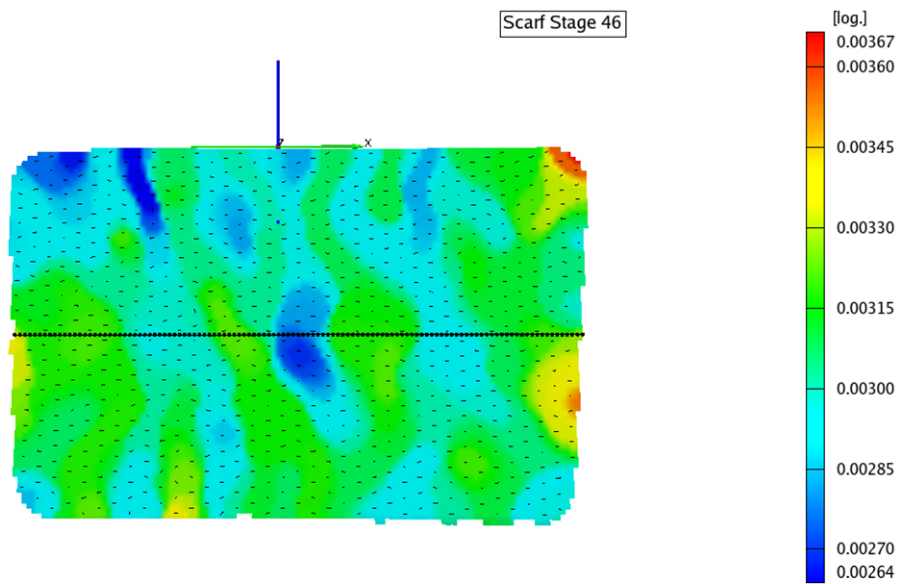


Figure 5.14. ϵ_{xx} : Panel #696 Experimental

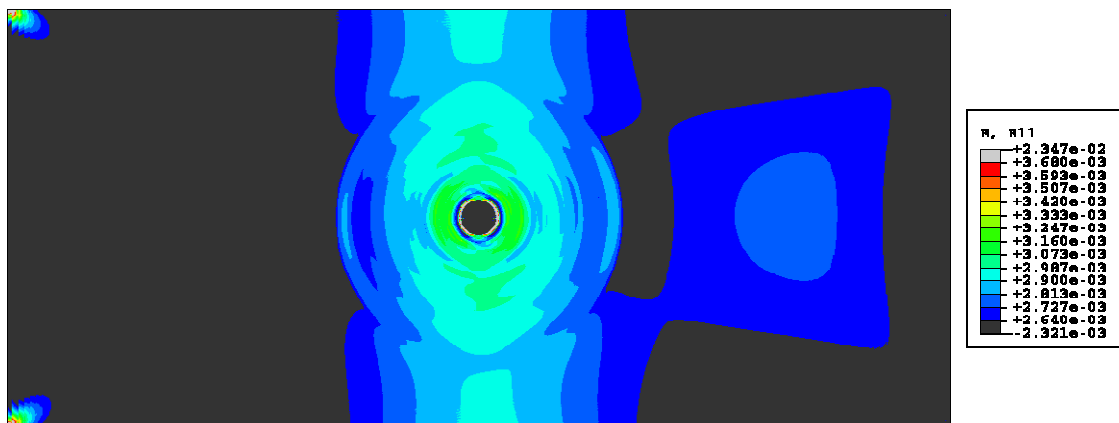


Figure 5.15. ϵ_{xx} : Finite Element

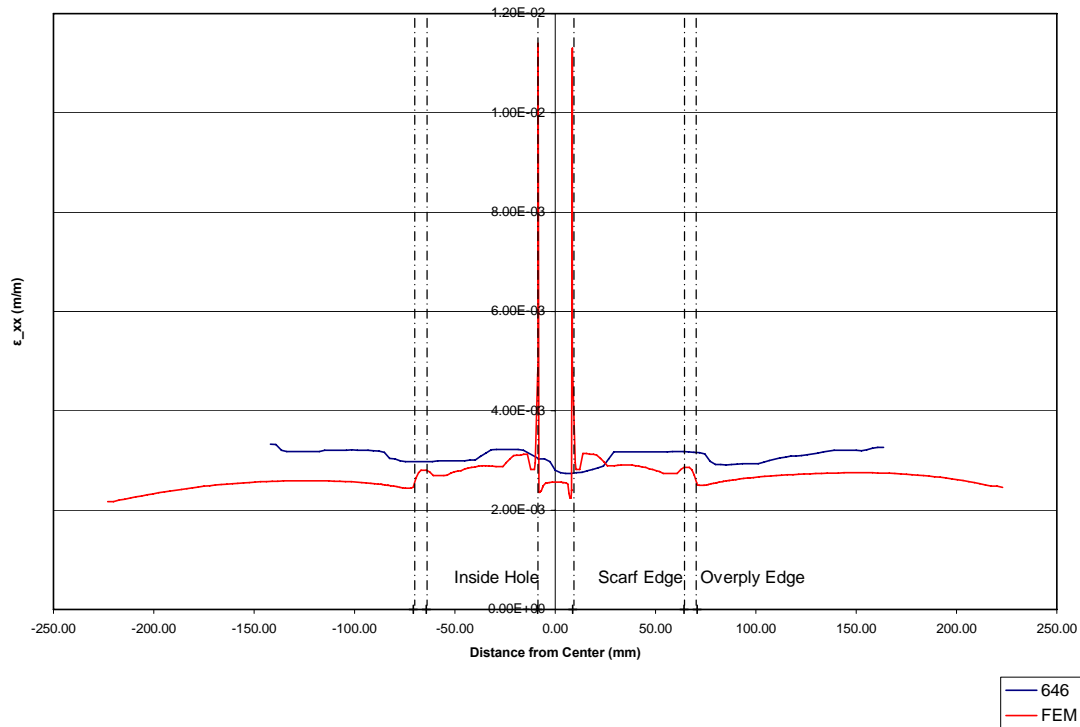


Figure 5.16. ϵ_{xx} : Data Plot, y=4, Experimental vs. Finite Element Model

5.1.2.2. ϵ_{yy}

The contours in Figure 5.17 and Figure 5.18 are similar to those of the previous section in that they show little correlation and that the experimental data is nearly featureless. The only similarity here is that both plots show little more than $1.5\text{E-}4$ strain variation throughout much of the panel. A plot of the strain along the centerline in Figure 5.19 shows a similar shape as than seen on the panel's top surface. It's interesting to note the strain is influenced by the edges of the overply as evidenced by the "humps" located in that region. Although the experimental data shows a similar but less pronounced behavior, it appears that the reference centerline may have been shifted

during analysis. The strain magnitudes in the two data sets show fairly good agreement. In the center, the finite element data is just 28.9% higher. In the overlap region on the positive side of the axis, variation is only 11.3%.

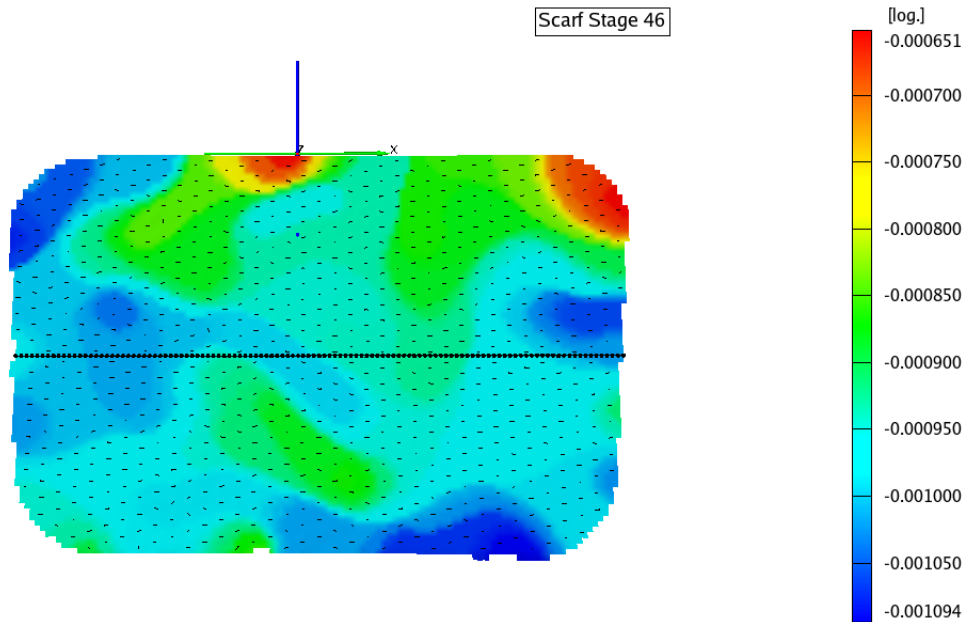


Figure 5.17. ϵ_{yy} : Panel #696 Experimental

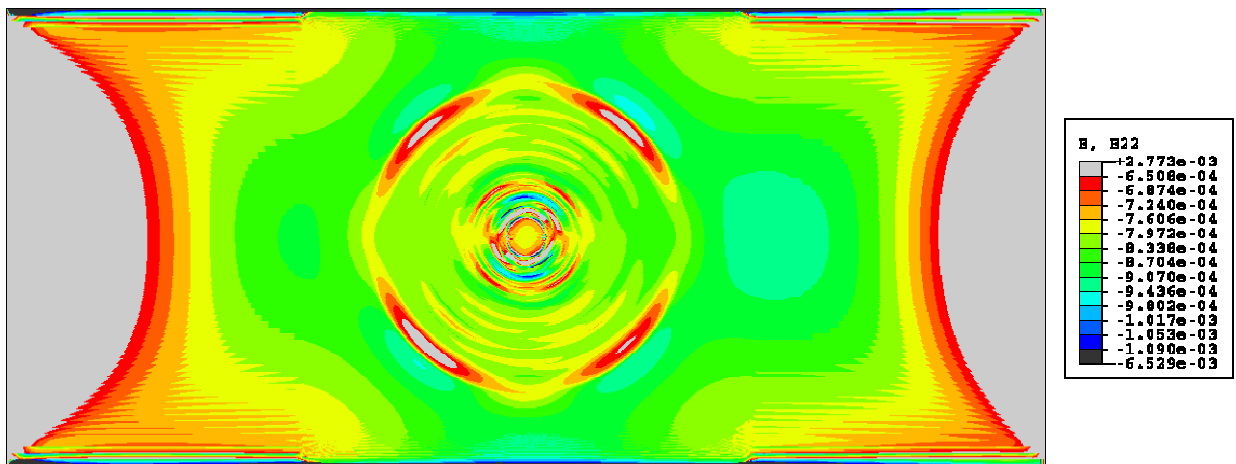


Figure 5.18. ϵ_{yy} : Finite Element

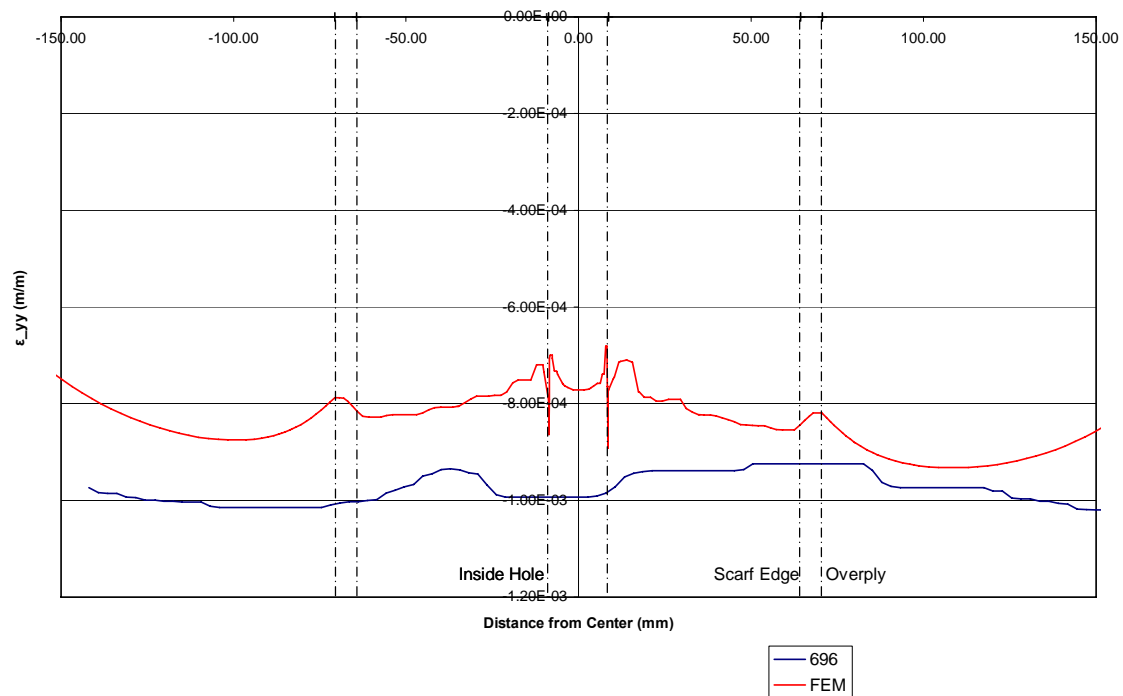


Figure 5.19. ϵ_{yy} : Data Plot, y=4, Experimental vs. Finite Element Model

5.1.2.3. ϵ_{xy}

As seen on the topside of the panel, the finite element model predicts areas of alternating positive and negative shear. The strain levels, however, while showing little variation, are very low. Based on earlier observations of the experimental data, the accuracy of strains this low are suspect. In the middle of the patch, for example, the experimental strain is only $-11 \mu\epsilon$. The distance separating the experimental and model data is just $25.9 \mu\epsilon$.

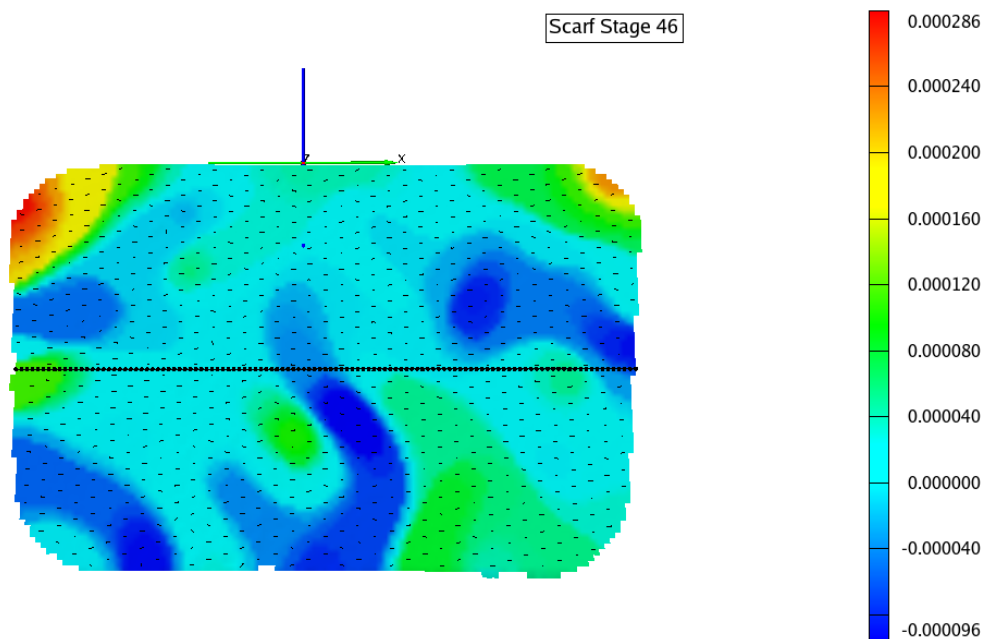


Figure 5.20 ϵ_{xy} : Panel #696 Experimental

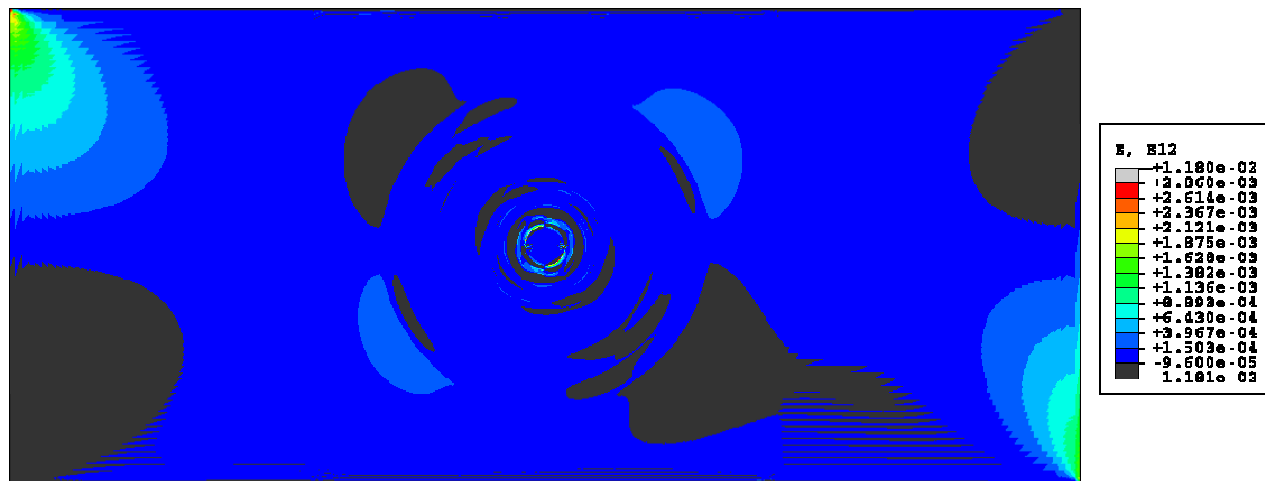


Figure 5.21. ϵ_{xy} : Panel #696 Experimental

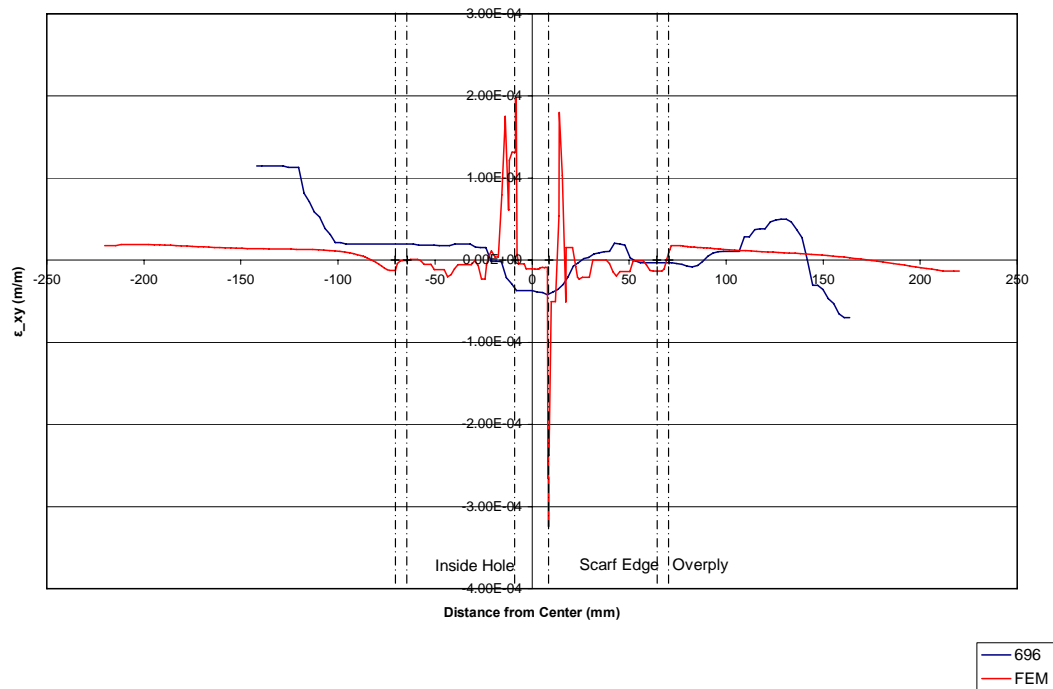


Figure 5.22 ϵ_{xy} : Data Plot, $y=4$, Experimental vs. Finite Element Model

5.2. Finite Element Model Stress Analysis

Having shown reasonably good correlation between the experimental data and the finite element model, it's of interest to look at the stresses in the areas within and adjacent to the repaired region. While strains are a natural extension of the displacement-based experimental measurement system used, it's difficult to use individual strain behavior to understand what's happening in a given region and it's implications on the joint strength. The three regions through the panel thickness that will be examined are shown in Figure 5.23. Of particular interest is the out-of-plane stresses which often contribute to delamination and eventual panel failure. In addition, the in-plane adhesive stresses will be examined.

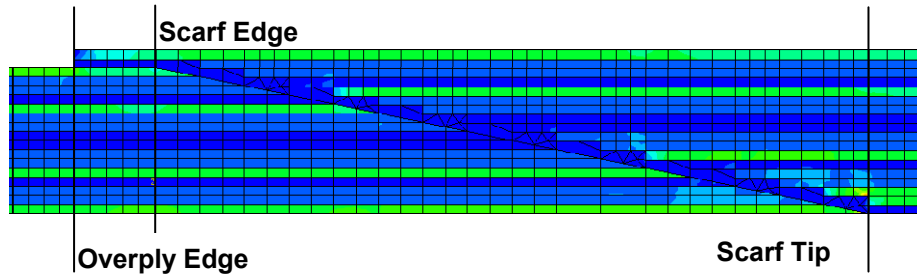


Figure 5.23. Stresses Through the Panel Thickness: Data Path Locations

5.2.1. Stresses Through the Repair Joint Thickness

The stresses in the x direction are shown in Figure 5.24 through Figure 5.26. Evident in the cross-section view is the behavior of the overply in the overlap region, where load is transferred across the joint to the panel. At the upper outside edge of the overply, the zero-stress condition is evident. Not surprisingly, in the rest of the joint, the 0° layers, aligned with the load path, see most of the longitudinal load. Stresses appear to be higher in the area just radially outside the tip of the scarf and in the second patch layer (the first 0° expected to carry a load). The stress distribution in the overply and scarf regions holds no surprises. The stress distribution in the first two layers of the patch, shown in Figure 5.26 is unusual, however. It appears that the stress isn't fully distributed through the 0° plies until the sixth ply in the patch.

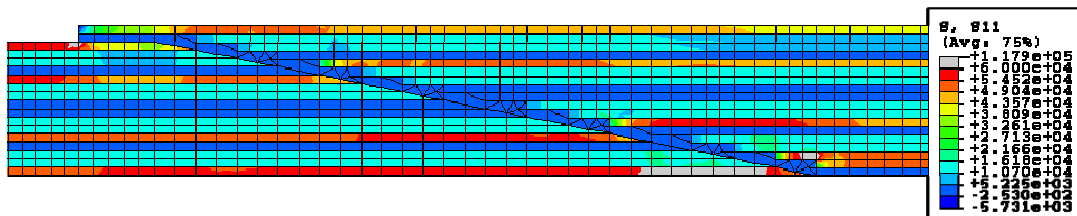


Figure 5.24. σ_{xx} : Repair Cross-Section, $y=4$

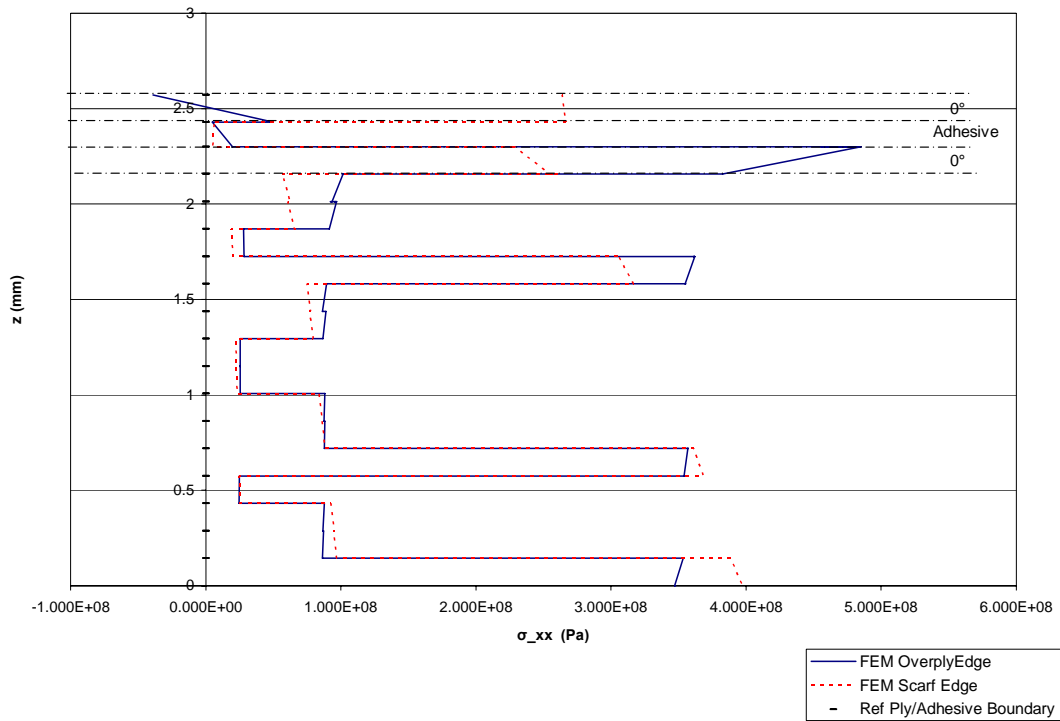


Figure 5.25. σ_{xx} : Overply and Scarf Edge (Figure 5.24)

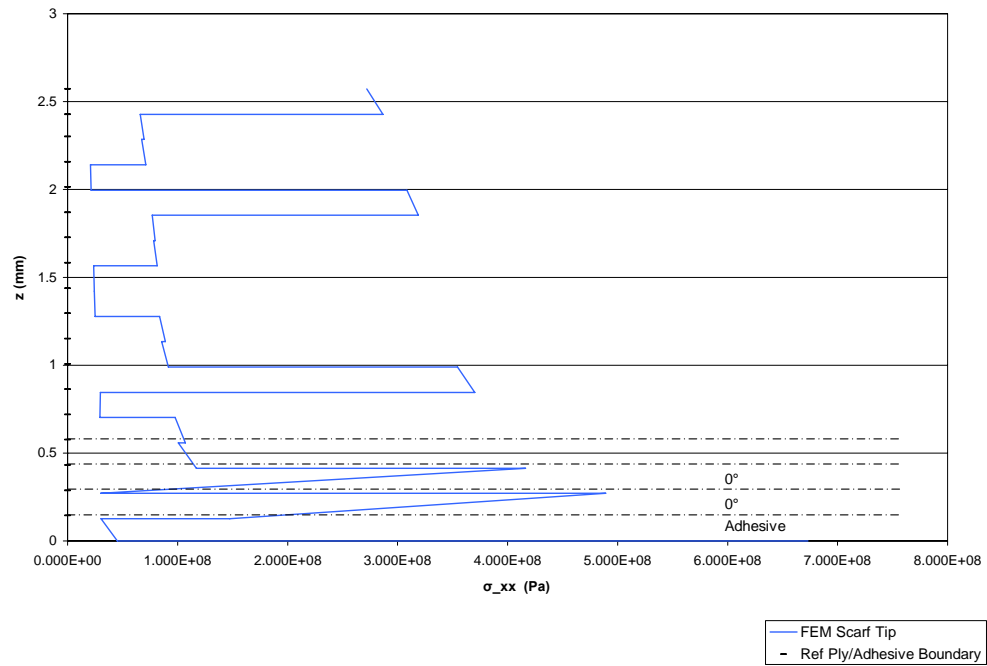


Figure 5.26. σ_{xx} : Scarf Tip (Figure 5.24)

Focusing now on the out-of plane stresses in the joint, we first examine σ_{zz} . Looking at Figure 5.27, we see that most of the stress in this direction is very localized and concentrated around the zero-degree plies. Figure 5.28 and Figure 5.29 show unusually high stress concentrations in the adhesive under the edge of the overply. Z-direction stresses appear to diminish rapidly. Stresses at the scarf edge are almost completely diminished. In the scarf tip region, the adhesive stresses are significant. Also of interest is the stresses between the first two 0° plies. While the first ply is typically considered just a “filler” (not expected to carry load), failure in this region could initiate a crack in the adhesive region which could propagate and lead to ultimate failure. During testing, one of these first layers popped off the panel prior to ultimate load, perhaps due to this σ_{zz} stress.

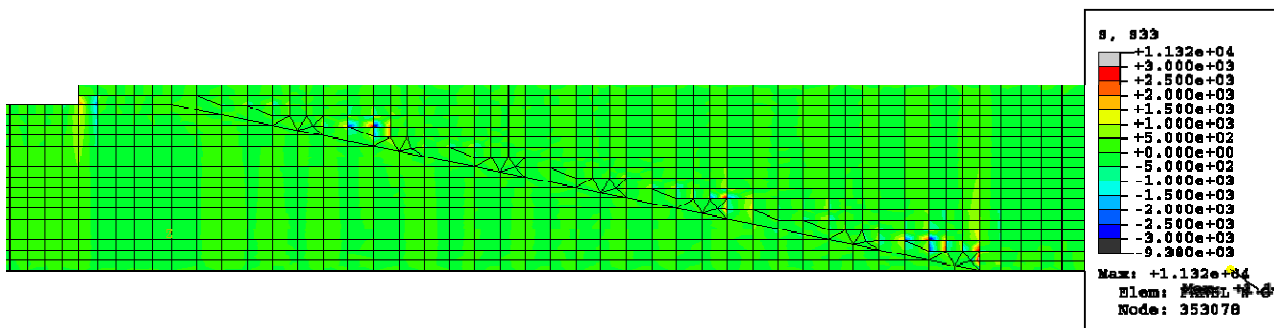


Figure 5.27 σ_{zz} : Repair Cross-Section, $y=4$

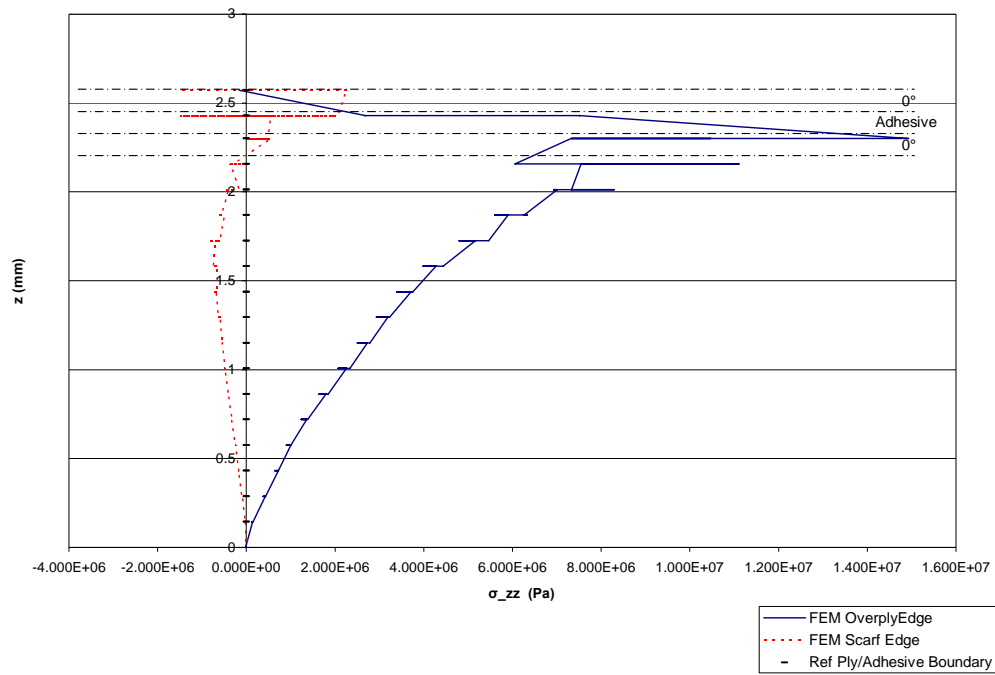


Figure 5.28 σ_{zz} : Overply and Scarf Edge (Figure 5.27)

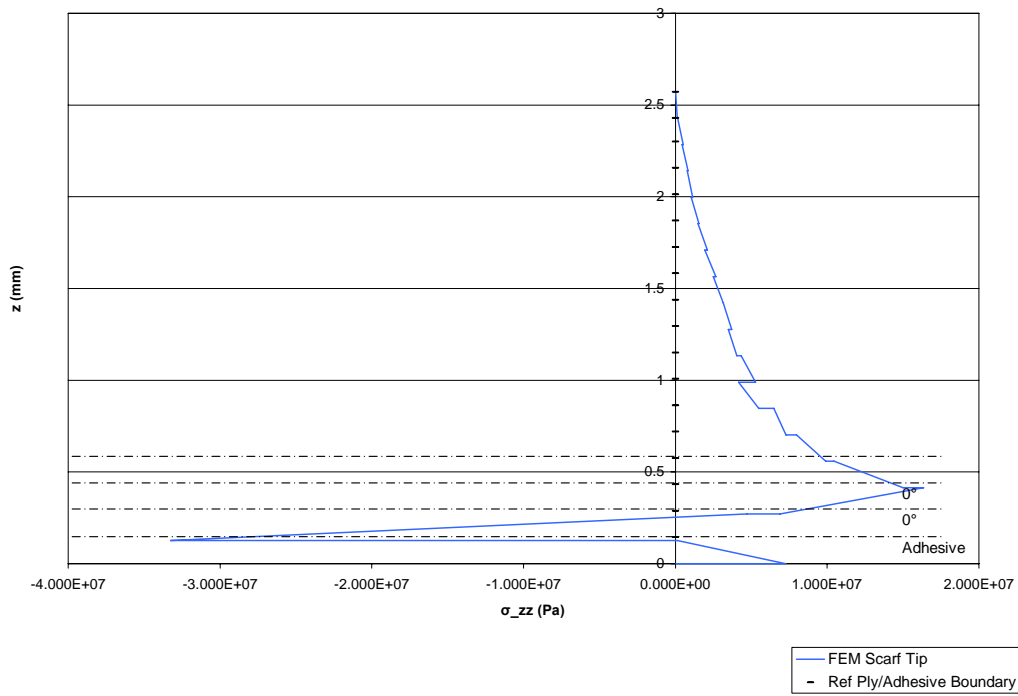


Figure 5.29. σ_{zz} : Scarf Tip (Figure 5.27)

The xz stress component shows similar trends (Figure 5.30 through Figure 5.31). Primary concentrations are in the adhesive immediately below the overply edge and at the tip of the scarf. In all cases, the concentrations appear to be localized around the edges of the 0° plies. Also, we again see that out-of-plane stresses at the edge of the scarf have significantly diminished.

The final out-of-plane stress that will be examined is σ_{23} , shown in Figure 5.33, Figure 5.34, and Figure 5.35. Besides the usual stress concentrations in the adhesive, the contour plot indicates that the highest concentrations are in the patch at the edges of the off-axis plies ($\pm 45^\circ$).

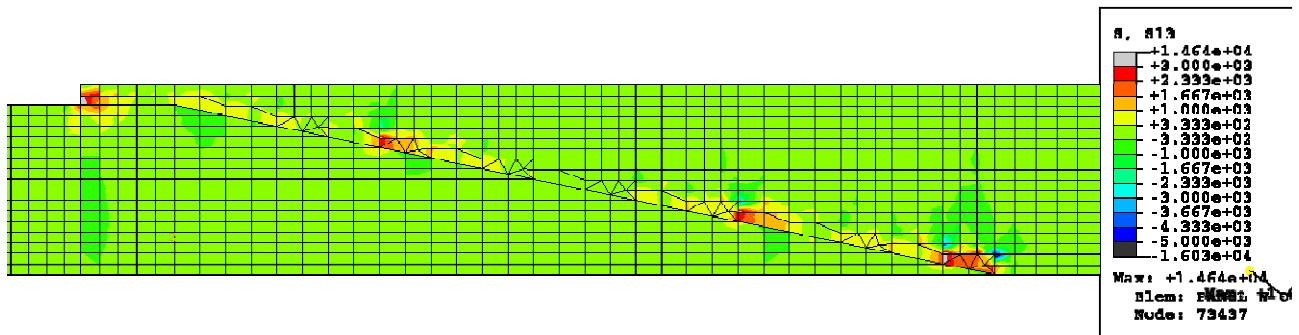


Figure 5.30 σ_{xz} : Repair Cross-Section, y=4

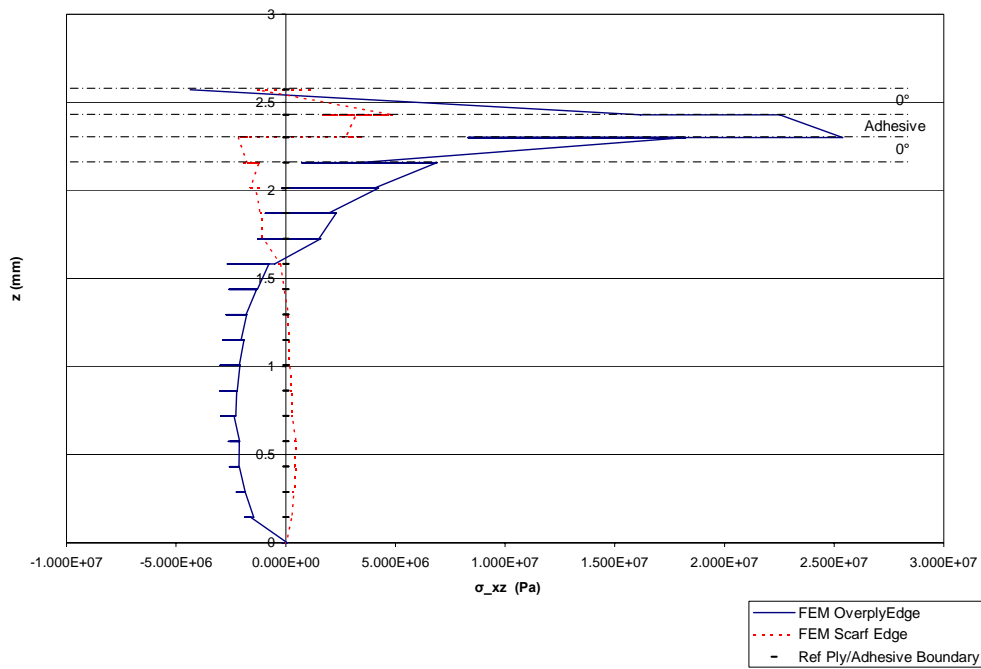


Figure 5.31 σ_{xz} : Overply and Scarf Edge (Figure 5.30)

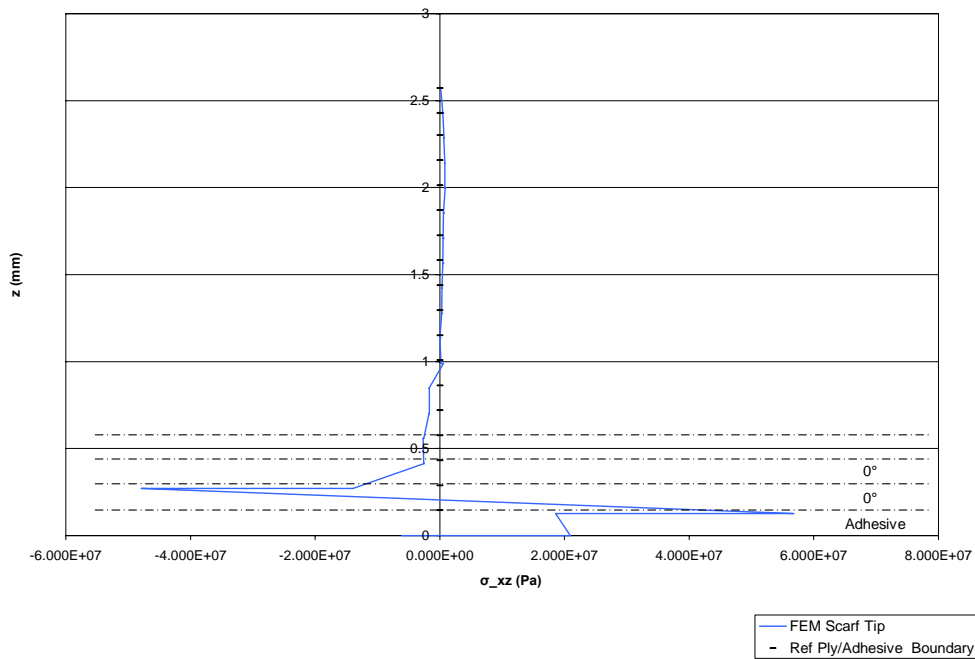


Figure 5.32. σ_{xz} : Scarf Tip (Figure 5.30)



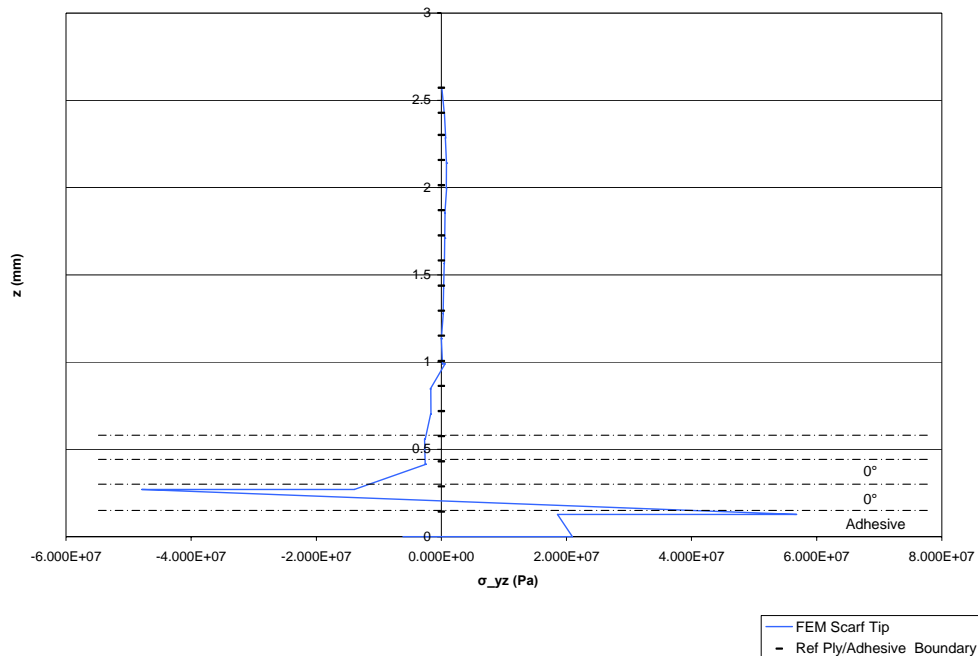


Figure 5.35. σ_{yz} Scarf Tip (Figure 5.33)

5.2.2. In-Plane Scarf Joint Adhesive Stresses

Alignment of the coordinate system with the panel scarf surface so that the x-axis is parallel to the panel scarf surface and the xy plane is perpendicular to this surface allows us to examine in-plane stresses in the adhesive, particularly those in the shear (σ_{xy}) and peel (σ_{yy}). The stress directions are transformed in ABAQUS according to the newly established coordinate system. The line plots were taken along a path drawn from the top of the adhesive down to the top of the bottom layer, intersecting the inside corner of each step in the adhesive.

In the peel direction, the stress peaks appear to be centered on the 0 plies. In shear, concentrations seem to be grouped around the ± 45 plies on both the patch and

panel side; also where a +45° is adjacent (one layer above or below) a -45° ply on the other side of the bond line.

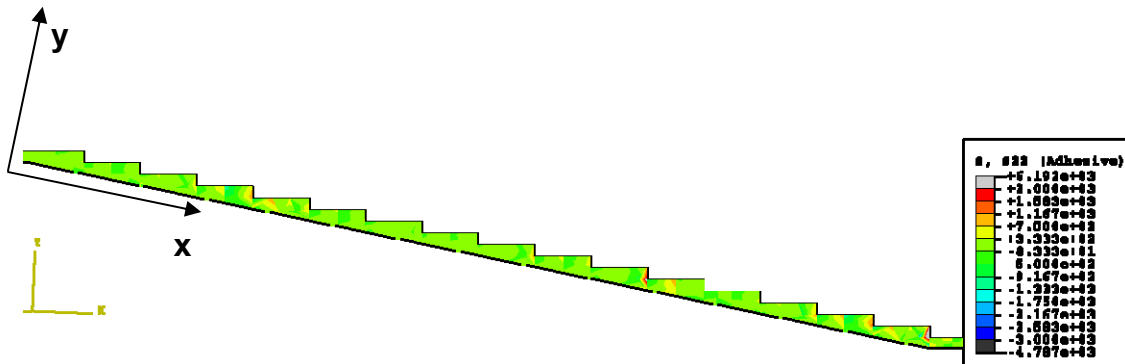


Figure 5.36. σ_{yy} : Stresses Transformed in-Plane with Scarf Edge

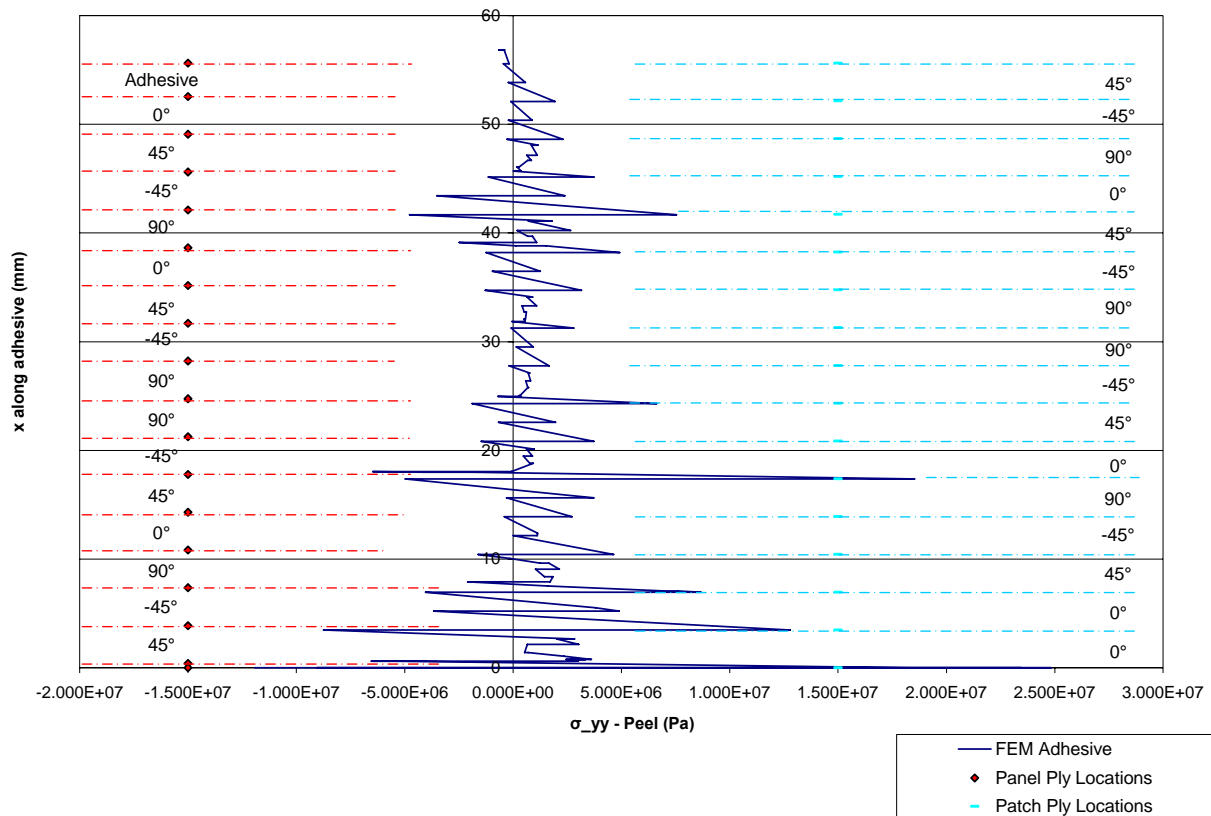


Figure 5.37. σ_{yy} : Line Plot, Stresses Transformed in-Plane with Scarf Edge

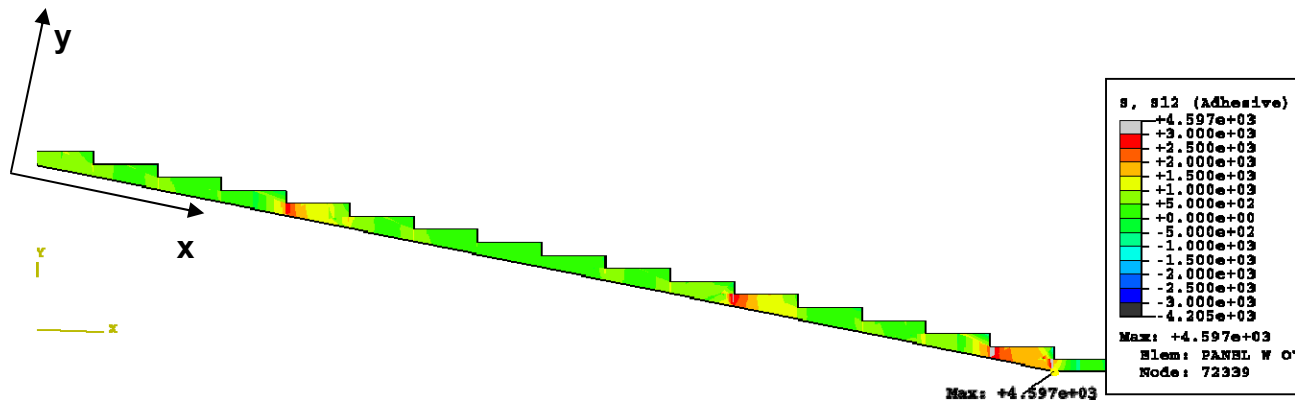


Figure 5.38. σ_{xy} : Stresses Transformed in-Plane with Scarf Edge

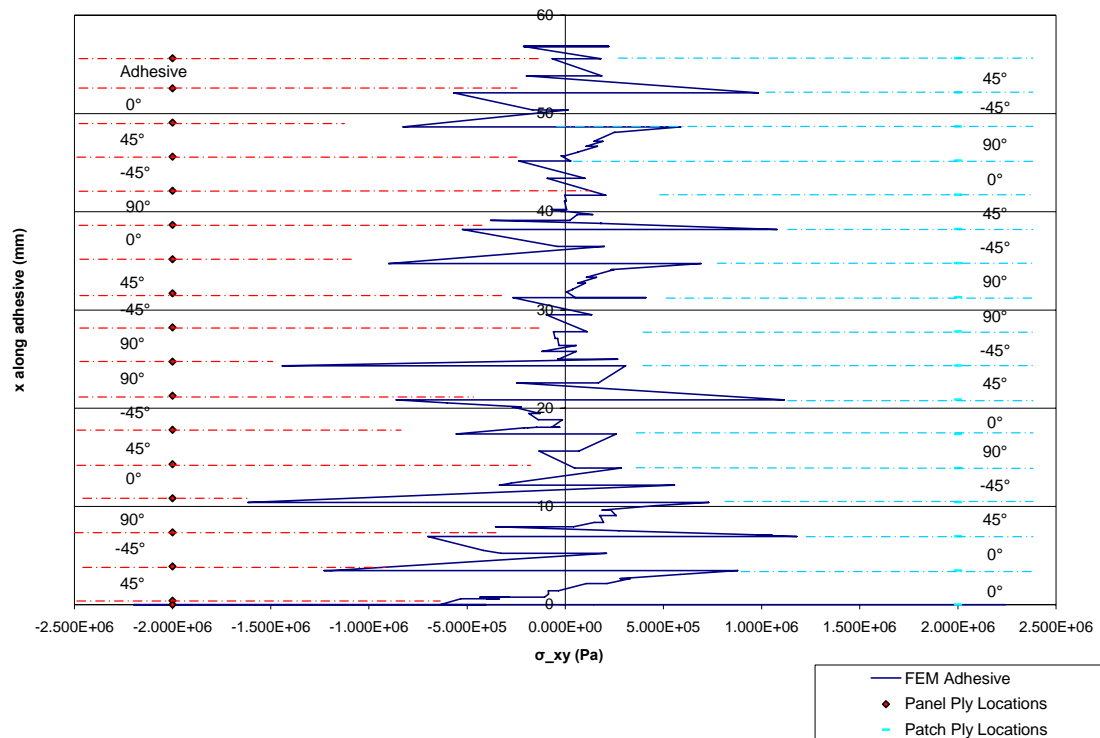


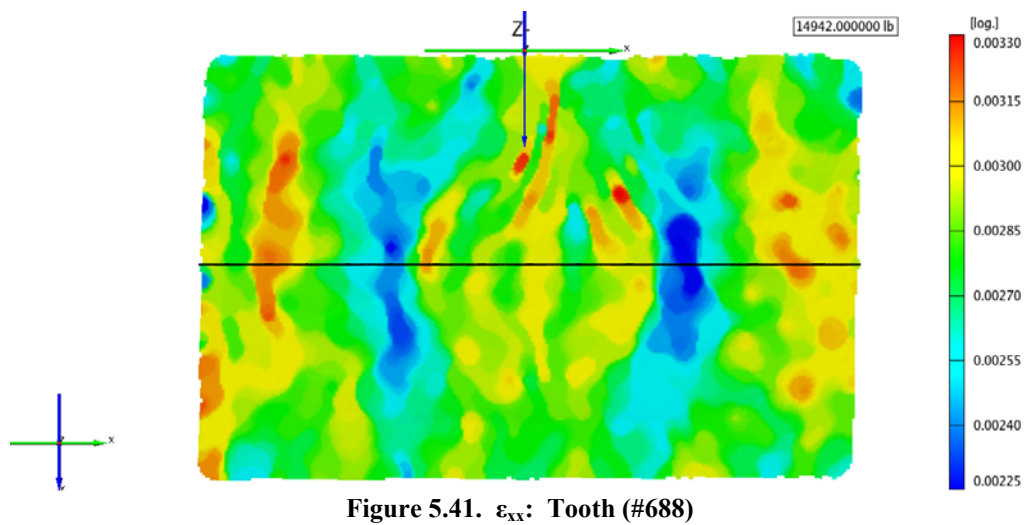
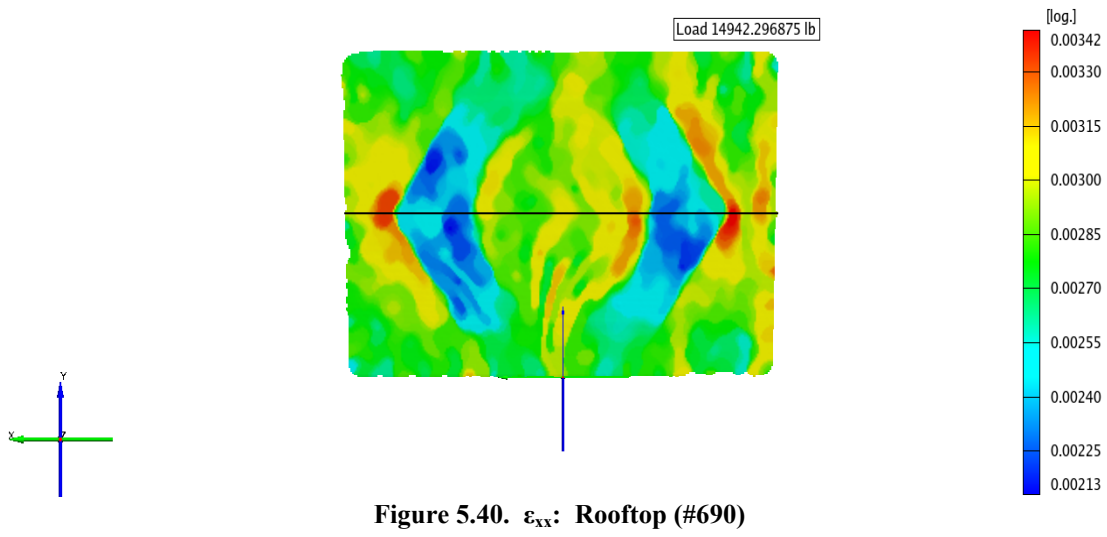
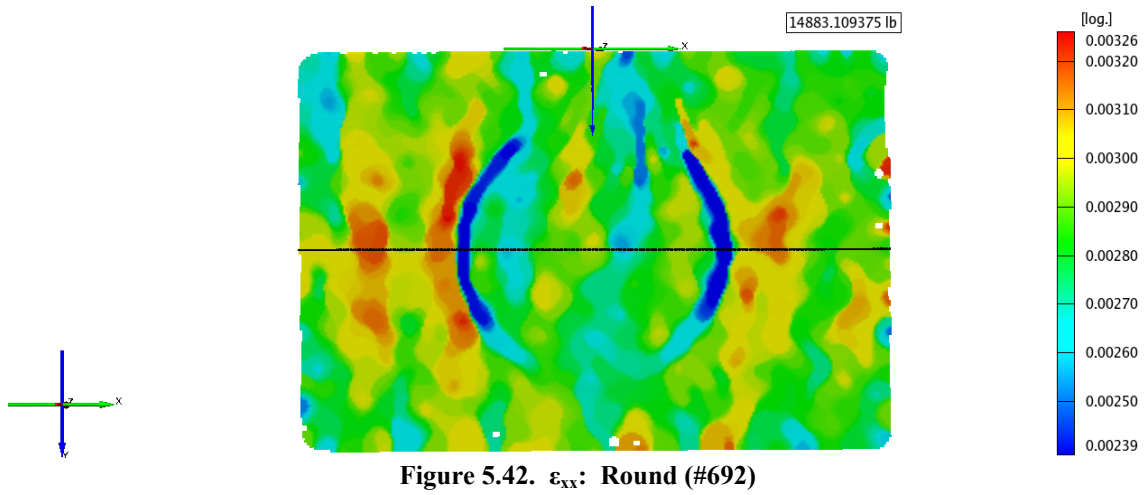
Figure 5.39. σ_{xy} : Line Plot, Stresses Transformed in-Plane with Scarf Edge

5.3. Comparison of Overply Geometries

For the most accurate comparison, each of the overply geometry groups are sorted according to their inner and outer hole diameter. Those panels with the closest diameters from each group are put into one group. The next set of panels with a slightly wider variation in hole diameters, are placed into a second set. For this discussion, the specific details of only the first set is examined. The second set serves only as a verification that what's seen in the first set is indeed a trend and not an anomaly. Panels in the first set include #692 (round), #690 (rooftop), and #688 (tooth). The second set of panels include #696 (round), #694 (rooftop), and #687 (tooth).

Figure 5.42 through Figure 5.43 show the contour and line plots for ϵ_{xx} . Several observations can be made looking at the strain along the centerline. First, the strains in the overlap zone are fairly uniform. The peak strains vary little between the different geometries. Compared to the round patch, the peak strains in panel #690 are only 4.1% higher. The tooth patch peak strain is just 0.28% higher than panel #692 with the round overply. Perhaps the most significant trend is the strain gradient as you move from the center of the patch out to the edge of the overply. Strain in both the round and rooftop overplies jumps nearly instantaneously as the outside edge of the patch is approached. For panel #690 (rooftop), on the positive side of the axis, there is a 38% increase in stress over a span of just 6 mm. In contrast, panel #688 has a 41% increase that's spread out over 51.3 mm. That's nearly ten times as long to build up the peak strain. The second set of panels exhibited similar trends.

The different overply geometries exhibit virtually no difference in the transverse strain (Figure 5.44 through Figure 5.46). At the center of the patch, the maximum strain is just 12.4% higher than the minimum strain. It should be noted that although panel #688 appears to show higher strain, this is inconsistent with the results of the second set of panels.



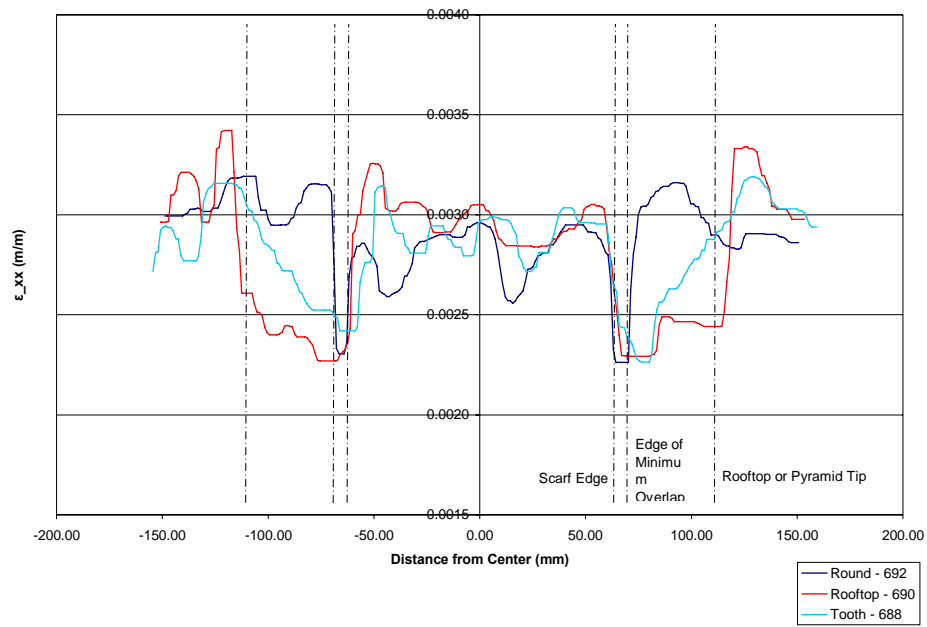


Figure 5.43. ϵ_{xx} : Geometry Comparison (y=4)

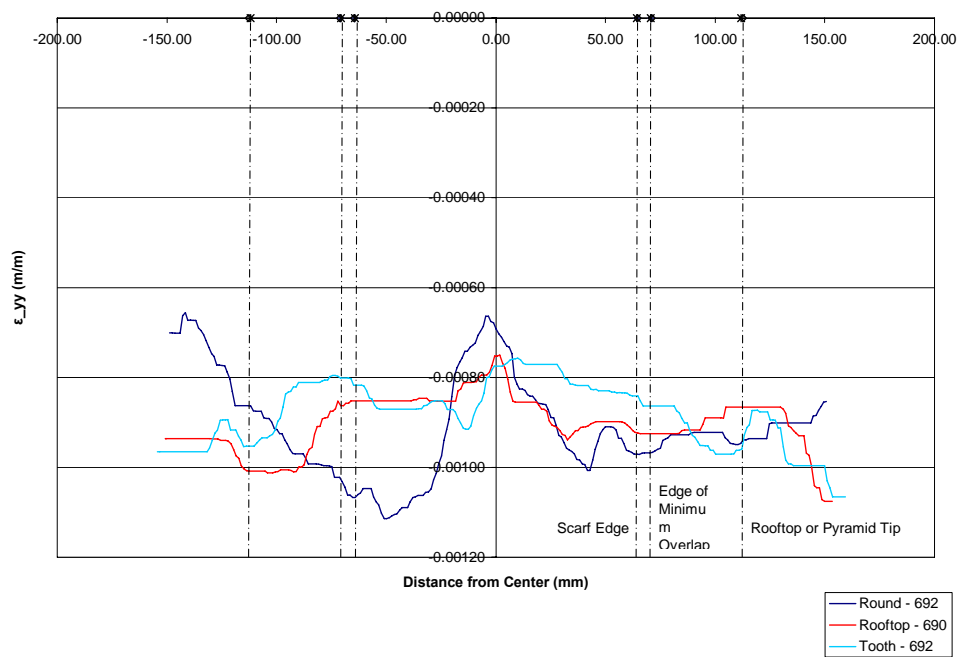


Figure 5.44. ϵ_{yy} : Overply Geometry Comparison (y=4)

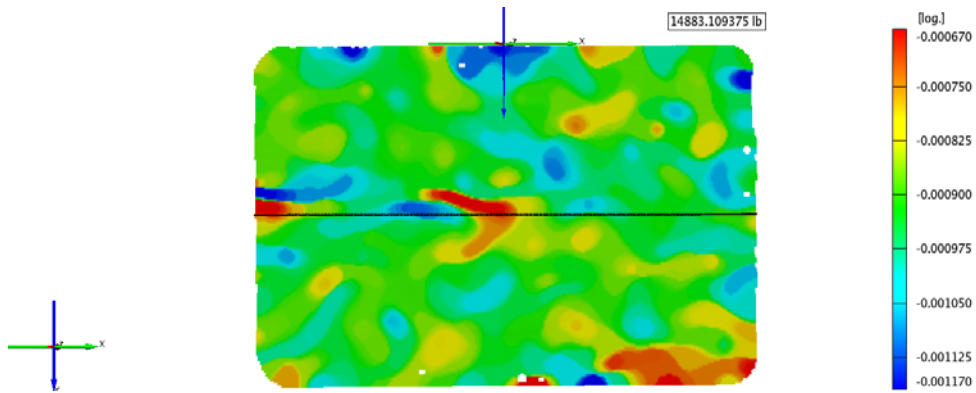


Figure 5.45. ϵ_{yy} : Round (#692)

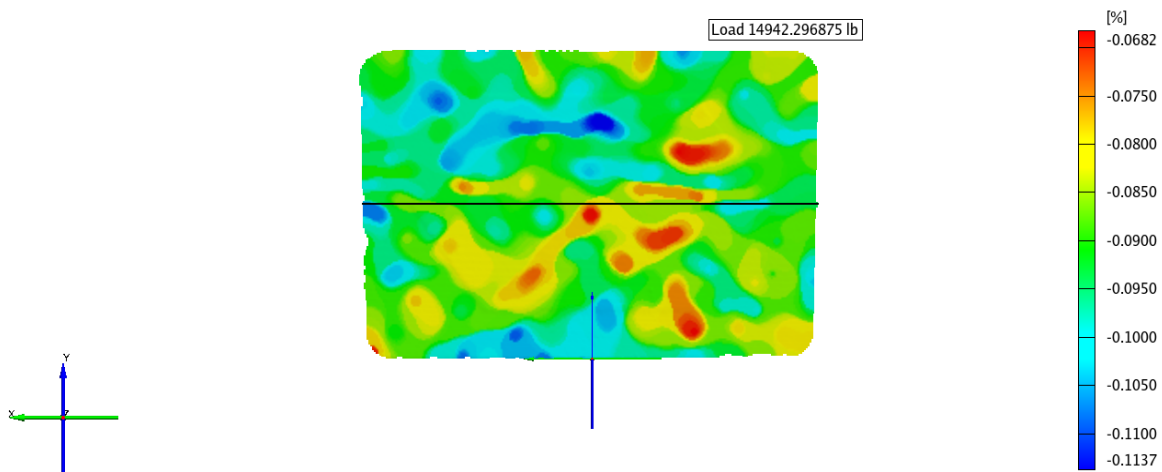


Figure 5.47. ϵ_{yy} : Rooftop (#690)

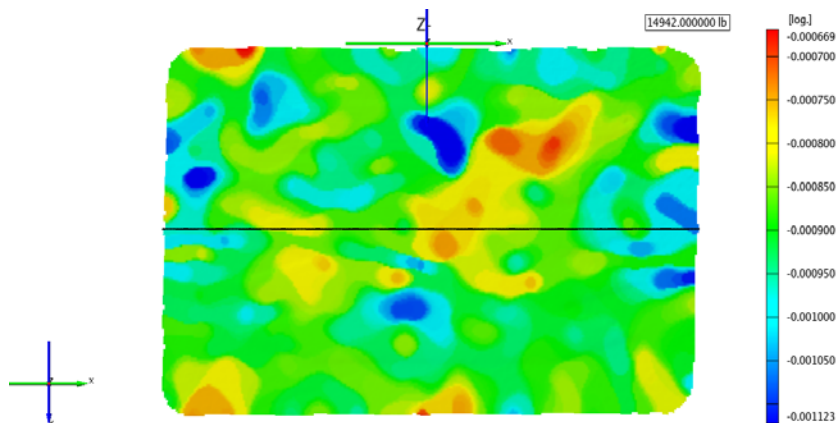


Figure 5.46. ϵ_{vv} : Tiger (#688)

VI. Conclusions and Recommendations

The combination of full field strain measurement using a digital image correlation photogrammetry system (ARAMIS) and finite element modeling enabled characterization of a three-dimensional scarf joint, and of the effects of variations in overply geometry. This was the primary objective of this research. This combination of experimental data and finite element analysis proved to be an effective means of modeling the joint's behavior and of validating that model. Additionally, based on experimental analysis of the overply geometries, the variation in strain behavior between the three profiles tested appears to be minimal. Conclusions are provided here in detail.

6.1. Repair Fabrication

To help achieve consistent, uniform taper ratios and diameters, a Scarf-o-Matic fixture was used. Experience reveals that this fixture requires a significant level of setup and adjustment to achieve acceptable results. Several factors, including fixture leveling and panel flatness, influence the ability of the fixture to cut a circular scarf. Even after these problems are overcome, it is difficult to achieve target diameters and cut it consistently in each panel. Although the scarf angle desired is 20:1, looseness inherent in the fixture's components results in an angle that varies slightly. This variation precludes achieving the target diameter by simple geometric calculations. Instead, a large amount of trial and error is required. Complicating this process is the thickness variation of each panel. The fixture has no means for fine adjustment; therefore, height adjustments to

accommodate the thickness of each panel will likely result in more variation. In this case, the height was held constant and the diameter variations resulting from different panel thicknesses were accepted.

6.2. Experimental Validation of a Finite Element Model

A full field strain measurement technique, such as the ARAMIS system used here, characterizes strain across an entire surface. It then displays the results as either a contour plot of the surface or a line plot created by a series of data points taken along a specified path. Commercially available finite element software, such as ABAQUS, uses similar methods of output display. The output similarity of the full field technique to that of commercial finite element software lends to its suitability for model validation.

Using both surface strain contour plots and plots of strains taken along the longitudinal centerline, the finite element model of the scarf joint with a circular overply is validated with the experimental data. Finite element strains on both the upper and lower surfaces of the panel show relatively good correlation with experimental measurements. In particular, the longitudinal strains exhibited similar trends, with maximum differences in magnitude around 14% on the top and between 11-29% on the bottom (compared to test data). In addition to validation of the model, the experimental data highlighted several areas that must be considered when using the digital image correlation photogrammetry method for strain measurement.

6.3. Digital Image Correlation Photogrammetry for Strain Measurement

As revealed by comparison of the experimental data with finite element data, the digital image correlation photogrammetry strain measurement method, like other strain

measurement techniques, is not a “one-size fit all” technique. It should be used when test applications are suited to its unique capabilities and when its limitations have been carefully considered.

Inherent limitations of the experimental method used are highlighted by magnitude disparities in regions of peak strain. Because of the averaging effect of the virtual strain gauge lengths exhibited in this measurement technique, the system isn't able to capture sharp strain singularities that may be evident in finite element model results. The gauge length here, 4.1 mm, is affected by a number of variables, including the field of view, the facet size, the step length, and the strain length.

Also, as evidenced by the poor correlation in the shear strain, expected strains should exceed the system sensitivity (inherent noise level), typically between 50-100 $\mu\epsilon$. In general, as the strains approach the sensitivity level, the signal to noise ratio decreases and the level of output filtering required increases.

6.4. Finite Element Model

With the finite element model showing fairly good correlation with experimental data, the model is used to characterize stresses within the repair joint and in the immediate vicinity. Many of the findings corroborate findings of previous studies using analytic methods and two-dimensional models. The primary focus here is on the out-of-plane strains that often contribute to delamination and joint failure. In the z direction, stresses are concentrated around the free edges of the 0° lamina. Stresses are most significant at the edge of the overply and at the tip of the scarf joint. Similar observations are made for stress in the xz direction. Stresses in the yz direction, however, show higher levels at the interfaces of the $\pm 45^\circ$ plies.

The in-plane stresses in the adhesive are also examined. The focus here is the shear and the peel stresses which drive the most common adhesive failure modes. Showing a similar trend to previous strain observations in the panel, adhesive peel stress is highest in areas adjacent to 0° plies. The shear showed highest concentrations at the $\pm 45^\circ$ ply interface.

Many of these stress observations are evident because the individual lamina are modeled individually in the finite element model. This approach is not without its shortcomings, however. To achieve reasonable accuracy, the maximum dimension of the element is dependant on the thickness of the ply (aspect ratio). The resulting model size, nearly 2.4 million nodes, limits its application. The standard desktop computer cannot handle such a model; its use is limited to only those with access to computers having the 37 giga-bytes of RAM required for the ABAQUS/Standard solution. The complexity of the model and the long processing time, nearly 8 hours using 12 CPUs, precludes any practical parametric study.

6.5. Overply Geometry Variation

Using full field strain measurement, three different profile geometries were examined, including a standard circular overply, a “rooftop” shape, and a “toothed” end. Results indicated that there was very little difference, if any, in the resulting strain magnitudes in either the longitudinal or transverse directions. These shapes were differentiated by the strain gradient in the areas adjacent to the peak strain exhibited at the boundary of the overplies. Both the round patch and the rooftop patch showed sharp steep strain gradients in these areas. The toothed patch, however, showed a much more gradual increase in strain.

6.6. Recommendations

This study characterized the scarf joint in the elastic range. While areas of higher stresses, etc. were identified, due to the elastic nature of this investigation, their effect on the ultimate strength of the joint is undetermined. A more thorough investigation of these areas identified, using higher loads and non-linear adhesive properties, needs to be accomplished before any conclusions about ultimate joint strength can be made.

If additional testing is undertaken, changes to either the specimen geometry (dog bone, etc.) or the load frame grip design must be made to ensure failure of the panel in the patch region. The panel geometry and grips used here resulted in consistent net section failure at the inside line of grip holes.

Further characterization of the ARAMIS system is also recommended. While the system excels in its flexibility and ease of use, like any test measurement system, there are limitations to its application. A parametric study that examines how strain sensitivity is affected by different factors, including displacement sensitivity (dependant on camera resolution and field of view), facet size, step size, and strain length. Additional characterization of the proper application of the filtering techniques is also recommended.

As discussed, the finite element model in its present form (size) limits its application. To increase its usefulness, several approaches may be taken to reduce its size. First, the mesh may be further refined so that the mesh is fine only in the areas of interest around the joint. Second, using the sub-modeling feature available in ABAQUS, the model may sub-divided to only the repair region, which would reduce the model volume by nearly 60%.

Additionally, the accuracy of the finite element model may be increased by modeling the patch to more closely resemble the physical patch configuration. In the current model, each layer is modeled as a planar layer. If the model were adjusted to reflect the test specimen's concave area in the center of the repair, eccentricity and therefore bending will be reduced.

Bibliography

ABAQUS Benchmarks Manual, rev. 6.6 (2006). Providence, RI: ABAQUS, Inc.

Adkins, D. W., & Pipes, R. B. (1978). Planar scarf Joints in Composite Repair. ICCM/2; Proceedings of the Second International Conference on Composite Materials, Toronto, Canada; United States; 16-20 Apr. 1978,

Ahn, S., & Springer, G. S. (1998). Repair of Composite Laminates-II: Models. *Journal of Composite Materials*, 32(11), 1076-1114.

Analysis/CAE Users Manual, rev. 6.6 (2006). Providence, RI: ABAQUS, Inc.

ARAMIS User Manual, v5.4.1 (2005). Mittelweg, Germany: GOM mbH.

Brannon, R. (2003). *Kinematics: The Mathematics of Deformation*. Unpublished manuscript.

Chu, T., Mahajan, A., & Liu, C. T. (2002). An Economical Vision-Based Method to Obtain Whole-Field Deformation Profiles. *Experimental Techniques*, 26(6), 25-28.

Chu, T. C., Ranson, W. F., Sutton, M. A., & Peters, W. H. (19850901). Applications of Digital-Image-Correlation Techniques to Experimental Mechanics. *Experimental Mechanics*, 25(3), 232-244.

Cloud, G. L. (1995). *Optical Methods of Engineering Analysis*. Cambridge ; New York: Cambridge University Press.

Cook, B. (2005). *Modeling and Experimental Measurement of Tensile Loaded Straight Scarf Joint*. (Masters, School of Engineering and Management, Air Force Institute of Technology (AU)). *AFIT/GA/ENY/05-M03*

Cytec Engineered Materials Inc. (2005). *Technical datasheet: FM 300 High-Shear Strength Modified Epoxy Film Adhesive*.

Dally, J. W., & Riley, W. F. (1991). *Experimental Stress Analysis (3rd edition)*. New York: McGraw-Hill, Inc.

Daniel, I. M., & Ishai, O. (1994). *Engineering Mechanics of Composite Materials*. New York: Oxford University Press.

Delara, R. J., Mitishita, E. A., & Habib, A. (2004). Bundle Adjustment of Images From Non-Metric CCD Camera Using LIDAR Data as Control Points. *XXth ISPRS Congress*, Istanbul, Turkey. , *TS WG III/1: Sensor Pose Estimation* pp.13.

Herakovich, C. T. (1998). *Mechanics of Fibrous Composites*. New York: Wiley.

Heslehurst, R. B., Dorworth, L. C., & Hoke, M. J. (2000). Comparison of Two Scarf Repair Configurations. *International SAMPE Symposium and Exhibition (Proceedings)*, 45 (1), 57-63.

Luhmann, T. (2006). *Close Range Photogrammetry : Principles, Techniques and Applications*. Dunbeath, Scotland: Whittles Pub.

Mallick, P. K. (1997). *Composites Engineering Handbook*. New York: M. Dekker.

Mikhail, E. M., Bethel, J. S., & McGlone, J. C. (2001). *Introduction to Modern Photogrammetry*. New York ; Chichester: Wiley.

Odi, R. A., & Friend, C. M. (2004). An Improved 2D Model for Bonded Composite Joints. *International Journal of Adhesion and Adhesives*, 24(5), 389-405.

Peters, W. H., & Ranson, W. F. (1982). Digital Imaging Techniques in Experimental Stress Analysis.

Pipes, R. B., & Adkins, D. W. (1982). *Strength and Mechanics of Bonded Scarf Joints for Repair of Composite Materials [Final Report, Jun. 1981 - May 1982]* (24 Composite Materials (AH) No. NASA-CR-169708; NAS 1.26:169708; CCM-82-14; Pagination 190P). Hampton, VA: NASA Langley Research Center.

Post, D., Han, B., & Ifju, P. (1994). *High Sensitivity Moiré : Experimental Analysis for Mechanics and Materials*. New York: Springer-Verlag.

Schmidt, T., Coe, D., & Tyson, J. (2004). *ARAMIS Training Part I*. Unpublished manuscript.

Schmidt, T., Tyson, J., & Galanulis, K. (2003). Full-Field Dynamic Displacement and Strain Measurement Using Advanced 3D Image Correlation Photogrammetry: Part I. *Experimental Techniques*, 27(3), 47-50.

Soutis, C., & Hu, F. Z. (1998). A 3-D failure Analysis of Scarf Patch Repaired CFRP Plates. *AIAA/ASME/ASCE/AHS/ASC Structures, Structural Dynamics, and Materials Conference and Exhibit, 39th, and AIAA/ASME/AHS Adaptive Structures Forum, Long Beach, CA; UNITED STATES; 20-23 Apr. 1998, , AIAA Paper 1998-1943*

Trillion Quality Systems, LLC. (2004). *3D aramis: Sensitivity, Accuracy and Data Validity Considerations*. Unpublished manuscript.

Vautrin, A., Lee, J. R., Molimard, J., & Surrel, Y. (2002). Full-Field Optical Techniques: Applications to Strain Measurement and Mechanical Identification. *Proc. of 10th European Conference on Composite Materials, Paper no. 338*, Brugge, Belgium.

What is the difference between CCD and CMOS image sensors in a digital camera? (April 01, 2000). Retrieved February 7, 2007, from <http://electronics.howstuffworks.com/question362.htm>

REPORT DOCUMENTATION PAGE				Form Approved OMB No. 074-0188	
<p>The public reporting burden for this collection of information is estimated to average 1 hour per response, including the time for reviewing instructions, searching existing data sources, gathering and maintaining the data needed, and completing and reviewing the collection of information. Send comments regarding this burden estimate or any other aspect of the collection of information, including suggestions for reducing this burden to Department of Defense, Washington Headquarters Services, Directorate for Information Operations and Reports (0704-0188), 1215 Jefferson Davis Highway, Suite 1204, Arlington, VA 22202-4302. Respondents should be aware that notwithstanding any other provision of law, no person shall be subject to a penalty for failing to comply with a collection of information if it does not display a currently valid OMB control number.</p> <p>PLEASE DO NOT RETURN YOUR FORM TO THE ABOVE ADDRESS.</p>					
1. REPORT DATE (DD-MM-YYYY) 22 Mar2007		2. REPORT TYPE Master's Thesis		3. DATES COVERED (From – To) Aug 2005 – Mar 2007	
4. TITLE AND SUBTITLE Three-Dimensional Analysis of a Composite Repair and the Effect of Overply Shape Variation on Structural Efficiency				5a. CONTRACT NUMBER	
				5b. GRANT NUMBER	
				5c. PROGRAM ELEMENT NUMBER	
6. AUTHOR(S) Sutter, David, A., Captain, USAF				5d. PROJECT NUMBER	
				5e. TASK NUMBER	
				5f. WORK UNIT NUMBER	
7. PERFORMING ORGANIZATION NAMES(S) AND ADDRESS(S) Air Force Institute of Technology Graduate School of Engineering and Management (AFIT/EN) 2950 Hobson Way WPAFB OH 45433-7765				8. PERFORMING ORGANIZATION REPORT NUMBER AFIT/GAE/ENY/07-M22	
9. SPONSORING/MONITORING AGENCY NAME(S) AND ADDRESS(ES) AFRL/MLBC Attn: Mr. Greg Schoeppner 2941 Hobson Way, Bldg 654, Rm 244 WPAFB OH 45433-7750 DSN: 785-9072				10. SPONSOR/MONITOR'S ACRONYM(S)	
				11. SPONSOR/MONITOR'S REPORT NUMBER(S)	
12. DISTRIBUTION/AVAILABILITY STATEMENT APPROVED FOR PUBLIC RELEASE; DISTRIBUTION UNLIMITED.					
13. SUPPLEMENTARY NOTES					
14. ABSTRACT <p>This research characterizes, in the elastic range, a scarf joint with overply using digital image correlation photogrammetry and finite element modeling. Additionally, the effect of varying the overply's geometric profile is examined. Specimens are constructed from AS4/3501-6 prepreg with a [0/±45/90]2S layup. A fixture is used to achieve a consistent scarfed hole in each panel. The patch and adhesive (FM 300) are co-cured to the panels using positive pressure, which minimizes repair porosity. Three variations in the overply geometry are used: circular, rooftop-end, and tooth-end.</p> <p>The full strain field in each uni-axially loaded specimen is captured using digital image correlation photogrammetry (ARAMIS). These results validate an ABAQUS 3-D finite element model of a scarf patch with circular overply. Good correlation is evident in the longitudinal strain; strain sensitivity limits correlation in the transverse and shear directions.</p> <p>The finite element model is used to identify peak out-of-plane stresses in the repair joint. Significant normal stresses occur at edge of the overply and at the inner scarf diameter.</p> <p>Finally, the experimentally-measured strains of the 3 overply variations are examined. Variation in strain magnitude is insignificant; the strain gradient at the overply edge, however, is significantly lower on the profile with the tooth-edge.</p>					
15. SUBJECT TERMS Fiber Reinforced Composites, Carbon Reinforced Composites, Repair, Bonded Joints, Photogrammetry, Stereo Photogrammetry, Finite Element Analysis, Scarf Joint					
16. SECURITY CLASSIFICATION OF:			17. LIMITATION OF ABSTRACT UU	18. NUMBER OF PAGES 138	19a. NAME OF RESPONSIBLE PERSON Anthony N. Palazotto
REPORT U	ABSTRACT U	c. THIS PAGE U			19b. TELEPHONE NUMBER (Include area code) (937) 255-3636, ext 4599; e-mail: Anthony.Palazotto@afit.edu